UNIVERSITA' DEGLI STUDI DI CATANIA

DIPARTIMENTO DI FISICA E ASTRONOMIA

XXX CICLO DI DOTTORATO

ABSOLUTE AND RELATIVE DOSIMETRY FOR THE ELIMED BEAM LINE

PhD THESIS

RENATA LEANZA

TUTOR:

Prof. S. Romano

SUPERVISORS:

Dott. F. Romano

Dott.ssa V. Scuderi

“Un raggio di sole è sufficiente per spazzare via molte ombre."
(San Francesco d’Assisi)

...A Voi che illuminate i miei giorni...

Abstract

Hadrontherapy is a type of external beam therapy which uses charged hadrons, mainly protons and carbon ions, to neutralize tumor growth with an improved precision and biological effect allowing to obtain a better dose deposition thanks to their characteristic Bragg peak, improving the ballistic precision and efficacy of the treatment, if compared to X-rays used in conventional radiotherapy.
One of the most challenging ideas, driving recent activities based on hadrontherapy applications, consists on using laser-target interaction as a source of high-energy ions for possible future medical applications, in order to reduce the costs of the infrastructure and increase the flexibility, if compared with conventional acceleration technics.
Several international collaborations and experiments have been launched in the last years aiming to explore the feasibility of using laser-driven sources for potential medical applications. In this framework, a collaboration between the INFN-LNS (National Institute for Nuclear Physics – Laboratori Nazionali del Sud, Catania, Italy) and the ASCR-FZU (Institute of Physics of the Czech Academy of Science), in charge for the ELI-Beamlines facility implementation, has been established with the main purpose to realize a transport and dosimetry beam line, named ELIMED (ELI- Beamlines MEDical and multidisciplinary applications), for laser accelerated ions.
In this thesis, dosimetry of laser-driven proton beams is discussed and results obtained with the dosimetric detectors developed for the ELIMED beam line are described. In particular, a description of the state-of-the-art of the different research centers available around the world and their activities, with the aim to

develop laser-driven ion sources for medical therapy and a brief description of the laser acceleration is presented. A detailed description of the ELIMED beam line is given with a focus on the details of the dosimetric systems of ELIMED beam line. The characterization of RCFs and FC with conventional beams, performed at the CATANA proton therapy facility at LNS is reported.

The characterization of dosimetric devices of ELIMED beam line, FC, SEM and multi-gap IC, in an experimental campaign carried out at Laboratoire d'Optique Appliquée (LOA, Paris, France), is discussed. Aim of the experiment has been the characterization of the detectors in terms of response, in order to reduce the EMP signal and to investigate the frequencies of the signal due to the oscillation modes of the EMP inside and outside the interaction chamber. The results obtained have confirmed that using a proper low-pass filters a signal generated from the fast ions component, accelerated in the laser matter interaction,can been discriminated, for each dosimetric detector.

The results discussed in this thesis demonstrate that the detectors designed and realized for the ELIMED beamline will allow to perform measurements for multidisciplinary applications with the level of accuracy required for these kind of irradiations.

Contents

Introduction

External beam Radiotherapy is a treatment modality which uses high energy ionizing radiation to destroy cancer cells in the area of interest.
Specifically, *Hadrontherapy* is a type of external beam therapy which uses charged hadrons, mainly protons and carbon ions, to neutralize tumor growth with an improved precision and biological effect. They allow to obtain a better dose deposition thanks to their characteristic Bragg peak, improving the ballistic precision and efficacy of the treatment, if compared to X-rays used in conventional radiotherapy.
The advantages of hadron radiation therapy, compared with the "conventional" one, were first outlined by Robert R. Wilson in 1946. He published his pioneering paper on the radiological use of fast protons to "*Acquaint medical and biological workers*" with some of the physical properties and potential of ion beams for medical use [1].
The number of hadrontherapy centers for proton and carbon ions treatment is constantly increasing.
In order to reduce the costs of the infrastructure and increase the flexibility, new compact accelerators for charged particles beam therapy have been proposed. One of the most challenging ideas driving recent activities consists on using laser-target interaction as a source of high-energy ions for possible future medical applications. Since the first experiments on laser-matter interaction, wide theoretical and experimental progresses have been carried out, confirming the possibility to accelerate multi-MeV ion beams from the interaction of high-intensity laser pulses (from 10^{18} to 10^{20} W/cm^2) on thin solid targets.

High fluxes per shot and broader energy spectra, if well controlled, could provide an alternative and powerful tool for dose delivery, representing a new opportunity for the therapeutic purposes of charged particles.
Different acceleration regimes [2],[3], such as the Target Normal Sheath Acceleration (TNSA) [4][5], the Radiation Pressure Acceleration (RPA) [6][7] and the Break-Out Afterburner (BOA) [8], have been studied and several experimental results, obtained mainly within the TNSA regime, have been reported in the literature[4][5].
Several international collaborations and experiments have been launched in the last years aiming to explore the feasibility of using laser-driven sources for potential medical applications and many research centers have been involved in the investigation of laser driven therapy and applications.
In this framework, a collaboration between the INFN-LNS (National Institute for Nuclear Physics – Laboratori Nazionali del Sud, Catania, Italy) and the ASCR-FZU (Institute of Physics of the Czech Academy of Science), in charge for the ELI-Beamlines (Extreme Light Infrastructure) facility implementation, has been established.
The main purpose of the collaboration is to realize a transport beam line, named ELIMED (ELI- Beamlines MEDical and multidisciplinary applications), for laser accelerated ions. The ELIMED beam line, designed and realized by LNS-INFN, represents the section of the ELIMAIA (Multidisciplinary Applications of laser-Ion Acceleration) user-oriented beam line addressed to the transport, handling and dosimetry of the laser-driven ion beams allowing the achievement of stable, controlled and reproducible beams which will be available for all the users interested in multidisciplinary and medical applications of such innovative technology with high energy laser-accelerated beams.
In this thesis, dosimetry of laser-driven proton beams is discussed and results obtained with the dosimetric detectors developed for the ELIMED beam line are described. In particular in chapter 1, an overview about physical and dosimetric quantities is reported.
In chapter 2, is presented a description of the state-of-the-art of the different re-

search centers available around the world and their activities, with the aim to develop laser-driven ion sources for medical therapy. Moreover, a brief description of the laser acceleration is reported.
A detailed description of the ELIMED beam line is given in chapter 3, with a focus on the details of the dosimetric systems of ELIMED beam line.
The characterization of these detectors with both conventional and laser-driven beams is presented, respectively in chapter 4 and chapter 5.

Chapter 1

Charged particle interactions with the matter: Physical and dosimetric quantities

1.1 Physical properties

1.1.1 Interaction of charged particles with the matter and range straggling

As it is well known, charged particles, due to their interaction mechanism with the traversed matter, provide a more advantagious dose delivery to the target volume with respect to photons.

When charged particles cross the material, can interact with the nuclei and the electrons close to their trajectory, in three distinct ways: they can *slow down* by myriad collisions with atomic electrons, setting electrons in motion by the collision; they can be *deflected* by myriad collisions with atomic nuclei orthey have head-on *collision with a nucleus*, setting secondary particles in motion. These processes are called, respectively, stopping, scattering, and nuclear interactions. Nuclear interactions are relatively rare and different interaction models are available to predict the reaction products.

Other types of interaction can take place, as Cherenkov radiation or bremsstrahlung, but due to their small probability at the energy of interest in hadrontherapy, they can be considered negligible for these purposes.
The range of a charged particle is defined as the traveled distance by incident particle in the material until it stops, before losing all its energy.
It is given by:

$$R = \int_0^T \left(\frac{dE}{dx}\right)^{-1} dE \tag{1.1}$$

where T is the incident particle kinetic energy.

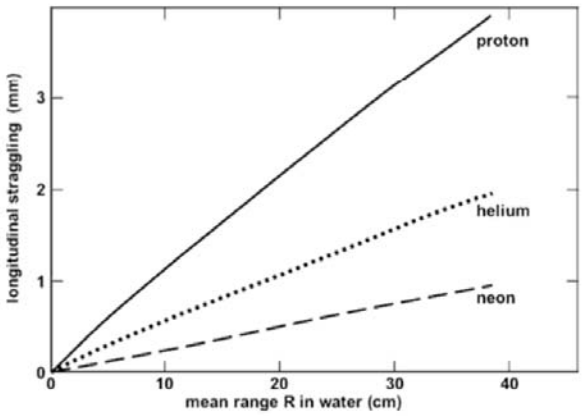

Figure 1.1: Range straggling of proton, helium and neon beam, as a function of mean range in water.

The particle range in hadron therapy is always specified in water because this is the reference material of interest in dosimetry considering the human body atomic composition. A maximum penetration depth of about 30 cm is tipically required and energies between 60 MeV and 250 MeV for protons and between 120 MeV/u and 400 MeV/u for carbon ions are necessary to reach tissues in depth.
Due to a finite number of individual interactions, energy deposit is a stochastic quantity.
Even if the initial beam energy is fixed, incident particles will not face the same

Table 1.1: Values of mean range and range straggling of protons and carbon ions for energies of interest in hadrontherapy.

Particles type	Energy [MeV/n]	Range [mm]	Straggling[mm]
Protons	66	36.1	1.5
	90	63	2.8
	125	112.9	4.7
	270	426.3	17.3
Carbon ions	66	12.5	0.5
	90	16.1	0.7
	125	38.5	1.5
	270	133.5	5

number of collisions and their range will be somewhat different. This phenomenon is called range straggling.

Range straggling corresponds to the standard deviation, σ, of the range distribution of a particle beam with mean range R.

In human tissues, the range straggling is of the order of 1% of the mean range of protons [9]. For heavier ions, range straggling varies approximately inversely of the square root of the particle mass. The integral range expression cannot be exactly calculated because of the straggling phenomenon, but like for energy loss, it is possible to define a mean range as the absorber thickness that reduces the particle beam of half of its initial value.

In figure1.1 is shown the range straggling of proton, helium and neon beam in water, as a function of the mean range [10].

In table1.1 are reported as an example some values of mean range and range straggling of protons and carbon ions for energies of interest in hadrontherapy.

Moreover it is possible to define also the extrapolated range, which is obtained by extrapolating the linear portion of the end of the transmission curve to zero.

1.1.2 The Bragg Peak

As mentioned before, most of particle energy is lost at the end of the path in crossed material, when the particles are stopping. This gives rise to the well known *Bragg peak*.

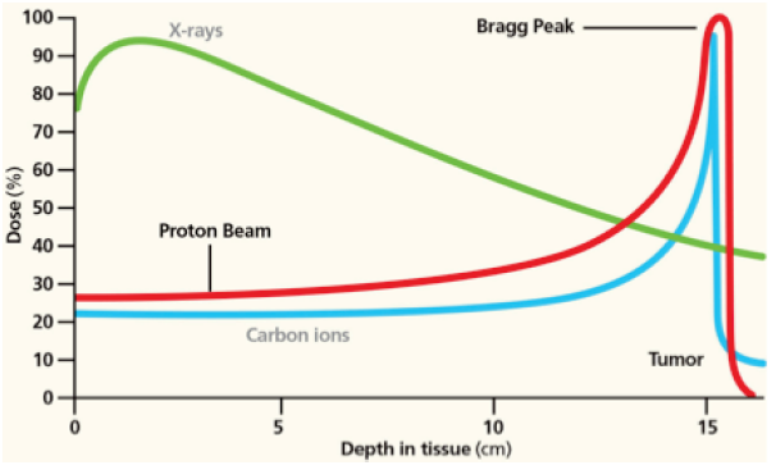

Figure 1.2: Dose released as function of depth for protons, carbon ions and X-rays.

The depth of the peak is determined by the incident beam energy. The width of the measured Bragg curve is typically determined by the energy spread. For higher incident energies the width of the Bragg peak becomes larger and the height smaller due to both electromagnetic and hadronic processes.
Figure 1.2 shows the dose released as function of depth for protons, carbon ions and X-rays.
Comparing the charged particle depth dose curves with that one of photons, used in conventional radiotherapy, it is evident the physical advantage of hadrontherapy.
Using charged particle beams, the superficial healthy tissues are slightly damaged, thanks to the good peak-plateau ratio[11]. On the other side, the intensity of photons, which are attenuated by crossed material through the three electromagnetic processes (photoelectric effect, Compton effect, pair production), follow the exponential absorption law $I(x) = I_0 e^{-\mu x}$ and depends on the linear attenuation

coefficient μ.
However, Bragg peaks are usually not wide enough to cover the target volume, so the Bragg peak must be spread out over the full depth of the tumor. By overlapping a set of mono-energetic beams with decreasing energies and weights, a Spread Out Bragg Peak (SOBP) is generated, (figure 1.3).
The SOBP and the lateral spread of the beam can be achieved by two different beam delivery techniques: the passive beam delivery makes use of energy degradation by absorbing materials of variable thicknesses in the beam path while in active beam scanning the energy and angle of the extracted pencil beam are varied to cover the tumor volume.

Passive Beam Delivery Passive scattering is a delivery technique in which scattering and range-shifting materials respectively spread the beam and degrade the energy. High density scattering foils are used for the first task, while wheels on increasing thickness are implemented to modulate the energy and to get homogeneous doses in the longitudinal direction.
Moreover, absorbing materials of variable thicknesses (range shifters) are typically used in the beam path in order to translate the SOBP to the desired depth.
Finally by using a collimator, the lateral extent of each treatment field is adapted to the beams eye view of the target volume.

Active Beam Scanning The active pencil beam scanning is more versatile compared to the passive technique.
This system takes advantage of the electric charge of the particles to produce a tightly focused pencil beam that is then deflected laterally by two magnetic dipoles to allow a scanning of the beam over the treatment field.
When the beam is produced with a synchrotron, the energy can be switched from pulse to pulse to adapt the range of the particles in tissue.
This way, a target volume can be scanned in three dimensions and the dose distribution can be tailored to any irregular shape without any passive absorbers or patient specific devices, like collimators.

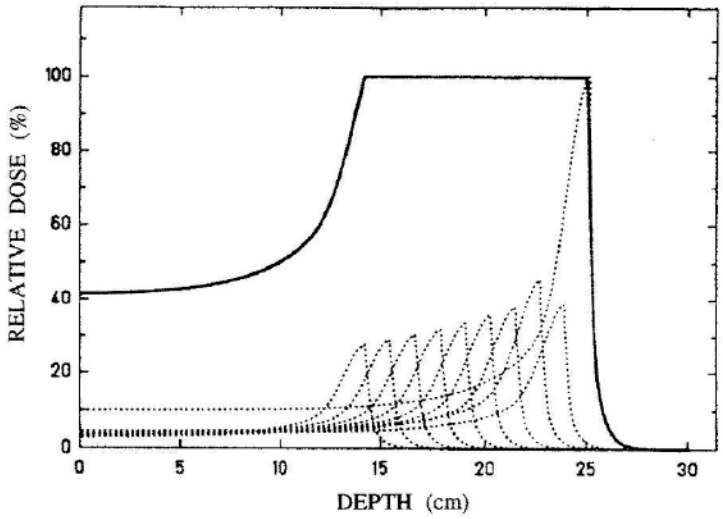

Figure 1.3: Overlapping of different Bragg peak curves in water and total effect in cumulative dose distribution (SOBP).

1.2 Dosimetry

The interaction of ionizing radiation with biological tissues produces biological effects to irradiated cells. To quantify these effects is first necessary to introduce some key physical quantities which describe the field of radiation as well as the interaction with the medium [12].

1.2.1 Physical quantities

A radiation field is created in a specific volume when it is irradiated by particles beams. The radiation field can be described by the following quantities:

Fluence: the particles number dN which go thought a sphere characterized of a maximum section of dA, centered on the interest point:

$$\Phi = \frac{dN}{dA}[m^{-2}] \tag{1.2}$$

Fluence Intensity: describes the particle fluence time evolution:

$$\phi = \frac{d\phi}{dt}[m^{-2}s^{-1}] \tag{1.3}$$

Energy Fluence: the product between the particle fluence and energy:

$$\Psi = \Phi E[Jm^{-2}] \tag{1.4}$$

1.2.2 Dosimetry quantities

In radiation therapy treatments, the dosimetric quantities have a fundamental role. A description of the main quantities used in radiation dosimetry has given in the following section [13].

Exposure

The exposure describes the ability to ionize air molecules by incident radiation. It refers to the produced charge, dQ, due to the air ionization while the radiation passing through an infinitesimal air volume with mass dm, considering that all secondary electrons are stopped in air. It can be defined as:

$$X = \frac{dQ}{dm} \tag{1.5}$$

The historical exposure unit of measure is the Roentgen (R) which in the International System (SI) corresponds to $1R = 2.58 \times 10^{-4} C/Kg$.

Kerma

Kerma is an acronym for kinetic energy released per unit mass [13]. It is a non-stochastic quantity applicable to indirectly ionizing radiations such as photons and neutrons.
It quantifies the average amount of energy transferred from indirectly ionizing radiation to directly ionizing radiation without concern as to what happens after this transfer.

In this section the discussion will be limited to photons.
The energy of photons is imparted to matter in a two stage process. In the first stage, the photon radiation transfers energy to the secondary charged particles (electrons) through various photon interactions (the photoelectric effect, the Compton effect, pair production, etc.). In the second stage, the charged particle transfers energy to the medium through atomic excitations and ionizations.
In this context, the kerma is defined as the mean energy transferred from the indirectly ionizing radiation to charged particles (electrons) in the medium $d\bar{E}_{tr}$ per unit mass dm:

$$K = \frac{d\bar{E}_{tr}}{dm} \qquad [Gy] \tag{1.6}$$

where $d\bar{E}_{tr}$ is the sum of the initial kinetic energies of all generated secondary charges (before they deliver energy by collision).
The unit of kerma is joule per kilogram (J/kg). The name for the unit of kerma is the gray (Gy), where 1 Gy = 1 J/kg.

Absorbed Dose

Absorbed dose is a quantity applicable to both indirectly and directly ionizing radiations.
For indirectly ionizing radiations, energy is imparted to matter in a two step process. In the first step (resulting in kerma), the indirectly ionizing radiation transfers energy as kinetic energy to secondary charged particles. In the second step, these charged particles transfer some of their kinetic energy to the medium (resulting in absorbed dose) and lose some of their energy in the form of radiative losses (bremsstrahlung, annihilation in flight).
The absorbed dose is defined as as the mean energy $\bar{E}$ imparted by ionizing radiation to matter of mass m in a finite volume V by:

$$D = \frac{d\bar{E}}{dm} \qquad [Gy = J/Kg] \tag{1.7}$$

The energy imparted $\bar{E}$ is the sum of all the energy entering the volume of interest minus all the energy leaving the volume, taking into account any mass-energy conversion within the volume. Pair production, for example, decreases the energy by 1.022 MeV, while electron-positron annihilation increases the energy by the same amount.
Note that because electrons travel in the medium and deposit energy along their tracks, this absorption of energy does not take place at the same location as the transfer of energy described by kerma. The unit of absorbed dose is joule per kilogram (J/kg). The name for the unit of absorbed dose is the gray (Gy).

Relationship between Kerma and Dose

Generally, the transfer of energy (kerma) from the photon beam to charged particles at a particular location does not lead to the absorption of energy by the medium (absorbed dose) at the same location. This is due to the non-zero (finite) range of the secondary electrons released through photon interactions [13].
Since radiative photons mostly escape from the volume of interest, one relates absorbed dose usually to collision kerma, K_{coll}.
In general, however, the ratio of dose and collision kerma is often denoted as:

$$\beta = \frac{D}{K_{coll}} \tag{1.8}$$

If radiative photons escape the volume of interest, an assumption is made that $\beta \approx 1$.
In figure 1.4 is shown the relation between collision kerma and absorbed dose under buildup conditions; under conditions of CPE in part (a) and under conditions of transient charged particle equilibrium (TCPE) in part (b).
As a high energy photon beam penetrates the medium, collision kerma is maximal at the surface of the irradiated material because photon fluence is greatest at the surface. Initially, the charged particle fluence, and hence the absorbed dose, increases as a function of depth until the depth of dose maximum z_{max} is attained.

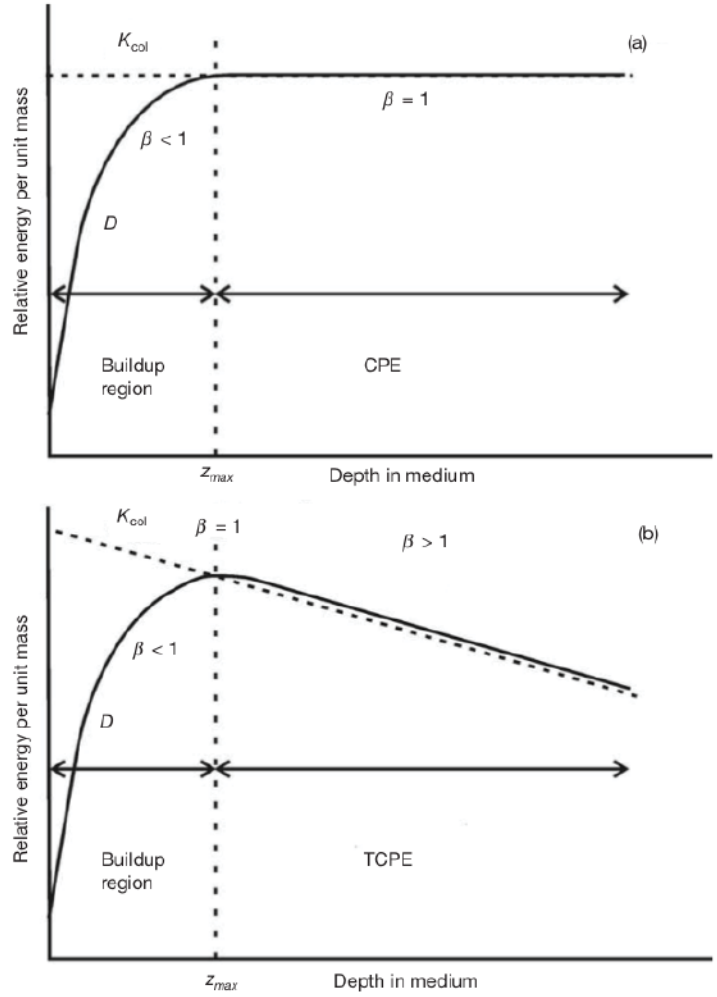

Figure 1.4: Collision kerma and absorbed dose as a function of depth in a medium irradiated by a high energy photon beam for (a) the hypothetical case of no photon attenuation or scattering and for (b) the realistic case.

If there were no photon attenuation or scattering in the medium, but yet production of electrons, a hypothetical situation, as illustrated in in figure 1.4 (a), would occur: the buildup region (with $\beta < 1$) is followed by a region of complete CPE where $D = K_{coll}$.
In the more realistic situation, however, due to photon attenuation and scattering in the medium, a region of TCPE occurs (figure 1.4 (b)) where there exists an essentially constant relation between collision kerma and absorbed dose. This relation is practically constant since, in high energy photon beams, the average energy of the generated electrons and hence their range does not change appreciably with depth in the medium.
The buildup of absorbed dose is responsible for the skin sparing effect in the case of high energy photon beams. However, in practice the surface dose is small but does not equal zero because of the electron contamination in the beam due to photon interactions in the media upstream from the phantom or due to charged particles generated in the accelerator head and beam modifying devices.

1.3 Biological effects in Hadrontherapy

In order to quantify the ionizing radiation effects in biological tissues and evaluate the efficiency in terms of tumor tissue damage, it is useful to consider several parameters connected to the biological effect.

L.E.T. The *Linear Energy Transfer* is defined as the energy dE lost by a charged particle due to soft and hard collisions in traversing a volume dl of crossed medium minus the total kinetic energy of the charged particles released with kinetic energies in excess of Δ:

$$L_\Delta = \left(\frac{dE}{dl}\right)_\Delta \tag{1.9}$$

It is expressed in $KeV/\mu m$.

It is closely related to the stopping power described by the equation:

$$-\frac{dE}{dx} = 2\pi N_a r_e^2 m_e c^2 \rho \frac{Z}{A}\frac{z^2}{\beta^2}\left[\ln\left(\frac{2m_e\gamma^2 v W_{max}}{l^2}\right) - 2\beta^2 - \delta - \frac{2c}{Z}\right] \tag{1.10}$$

where:

- N_a is the Avogadro number;
- m_e is the mass of the electron;
- Z and A are respectively the atomic and the mass number of the crossed material while $z$is the atomic number of the incident particle
- $\beta = vc$, expresses the incident particle velocity (v) relative to the speed of light (c);
- $\gamma = 1/\sqrt{(1-\beta^2)}$ is the Lorentz factor;
- ρ is the density of the target material;
- I is the mean excitation energy of the target material;
- W_{max} is the maximum energy transferred to a single collision;
- δ is density correction. It is significant only at high energy and takes into account that the electric field of the accidental incident particles tends to polarize the atoms along their path, so that distant electrons feel less electric field effect;
- C is the shell correction factor.

While stopping power can be seen as a material property (depending on electron density), which describes the energy absorbed by matter, LET describes the loss of energy by the particle.
If no limits are imposed on energy, L_Δ became L_∞, which represent the absolute value of stopping power.

Based on that, it is possible to distinguish high LET particles, as protons (for low energy ranges), alpha particles heavy ions and neutrons which densely ionize the crossed medium and low LET particles, as electrons and photons.
It has been extensively demonstrated that high LET particles produce less reparable damage at the cellular level, therefore are considered more efficient. The high level of dose conformation to the target together with an enhanced biological effect make hadrontherapy a powerful alternative cancer treatment radiation modalities, respect to radiotherapy with X-rays.

Relative biological effectiveness (RBE) In order to determine the final biological effect due to the interection of particles with the crossed matter in radiotherapy, it is necessary to define the RBE (Relative biological effectiveness) as the ratio of the sparsely ionizing radiation D_{ref} (mostly 220 keV X−rays) and the dose of particles radiation D_{ion} producing the same biological effect:

$$RBE = \frac{D_{ref}}{D_{ion}} \tag{1.11}$$

The RBE depends on different parameters both physical and biological ones: the delivered dose in the tissue, the type incident particles, LET, the cell or tissue type irradiated as well as on the selected biological endpoint.
All these physical quantities have to be experimentally measured in order to have a correct estimation of the radiation biological effectiveness.
Indeed, the RBE increase with the LET until a maximum value and after decrease, as shown in figure 1.5.
For proton beams the maximum of RBE corresponds to a lower value of LET then that one of other light ion beams.
The RBE decreasing after this value depends on the fact that for very high LET values the deposited energy is so large that the ionizing density inside the single cell is higher than that one necessary to achieve the cell inactivation. Hence the dose in excess is in some way dissipated inside the single cell and it does not contribute to cell death, implying an RBE decrease, called “overkill” effect.

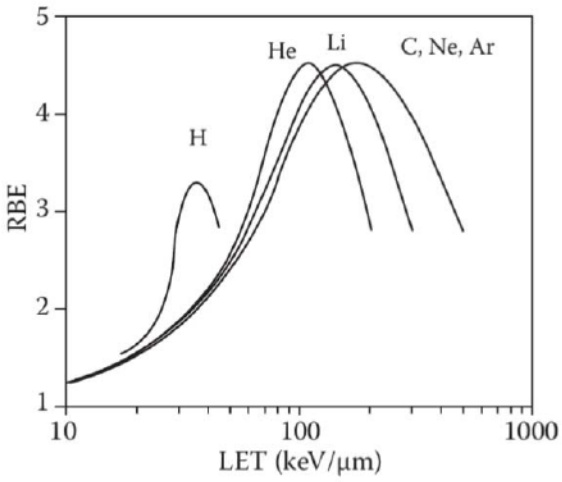

Figure 1.5: Schematic of the relationship between RBE and LET for cells exposed to different charged particles.

1.4 Measurement of the absorbed dose

Absorbed dose to water is the quantity of interest in radiation therapy, since this quantity relates closely to the biological effects of radiation. In order to determine this quantity, according to dosimetric protocols of IAEA-TRS 398 [14], a ionization chamber has to be used because of its high response sensitivity and, furthermore, because of the interaction processes involved are well known. In order to be used in the clinical facilities, the ionization chambers have to be first calibrated in a primary or secondary standard laboratory and, after that, they can be considered a reference for cross-calibrating any other dosimeter.

1.4.1 Bragg-Gray cavity theory

The determination of the absorbed dose in a point of an irradiated material could be obtained by measuring the ionization produced in a small cavity, filled of a material sensitive. The conversion of ionization, inside the cavity, in absorbed dose is possible thanks to the Bragg-Gray principle.
The Bragg-Gray cavity theory was the first cavity theory developed to provide a

relation between the absorbed dose in a dosimeter and the absorbed dose in the medium containing the dosimeter [13].
The conditions for application of the Bragg-Gray cavity theory are:

- The cavity must be small when compared with the range of charged particles incident on it, so that its presence does not perturb the fluence of charged particles in the medium;
- The absorbed dose in the cavity is deposited solely by charged particles crossing it (i.e. photon interactions in the cavity are assumed negligible and thus ignored).

Under these two conditions, according to the Bragg-Gray cavity theory, the dose to the medium D_{med} is related to the dose in the cavity D_{cav} as follows:

$$D_{med} = D_{cav}(\frac{\bar{S}}{\rho})_{med,cav} \tag{1.12}$$

where $(\frac{\bar{S}}{\rho})_{med,cav}$ is the ratio of the average unrestricted mass collision stopping powers of the medium and the cavity. The use of unrestricted stopping powers rules out the production of secondary charged particles (or delta electrons) in the cavity and the medium.
Although the cavity size is not explicitly taken into account in the Bragg-Gray cavity theory, the fulfilment of the two Bragg-Gray conditions will depend on the cavity size, which is based on the range of the electrons in the cavity medium, the cavity medium and the electron energy.
A cavity that qualifies as a Bragg-Gray cavity for high energy photon beams, for example, may not behave as a Bragg-Gray cavity in a medium energy or low energy X-ray beam.
The Bragg-Gray principle can be applied to X-rays, gamma, photons with energy higher the 3 MeV, electrons and heavy particles. In all cases, the measure of absorbed dose are normally made using ionization chambers filled of air and apply this theory.

1.4.2 Absolute dosimetry for proton beams

In order to determine the absorbed dose the IAEA-398 [14] dosimetric protocols is used.

Generically, the absorbed dose to water at the reference depth z_{ref} in water for a reference beam of quality Q' and in the absence of the chamber is given by:

$$D_{w,Q'(Gy)=M_{Q'}N_{D,w,Q'}}(1.13)$$

where $M_{Q'}$ is the reading of the dosimeter under the reference conditions used in the standards laboratory and $N_{D,w,Q'}$ is the calibration factor in terms of absorbed dose to water of the dosimeter obtained from a standards laboratory. In most clinical situations the measurement conditions do not match the reference conditions used in the standards laboratory. This may affect the response of the dosimeter and it is then necessary to differentiate between the reference conditions used in the standards laboratory and the clinical measurement conditions.

The reference conditions for calibrations in terms of absorbed dose to water are, for example, the geometrical arrangement (distance and depth), the field size, the material and dimensions of the irradiated phantom, and the ambient temperature, pressure and relative humidity.

Many influence quantities cannot be controlled, for example air pressure and humidity, but itis possible to correct for the effect applying appropriate factors in eq.1.13.

When a dosimeter is used in a beam of quality Q different from that used in its calibration, Q' , the absorbed dose to water is given by:

$$D_{w,Q}(Gy) = M_Q N_{D,w,Q'} k_{Q,Q'}(1.14)$$

where M_Q is the reading of the dosimeter with the reference point of the chamber positioned at z_{ref} in accordance with the reference conditions corrected for the influence quantities pressure and temperature, electrometer calibration, polarity effect and ion recombination.

$N_{D,w,Q'}$ is the calibration factor in terms of absorbed dose to water for the dosimeter at the reference quality Q' and $k_{Q,Q'}$ is a chamber-specific factor which corrects

for differences between the reference beam quality Q' and the actual quality being used Q.
The most common reference quality Q' used for the calibration of ionization chambers is ^{60}Co gamma radiation.
For a proton beam of quality Q and in the absence of the chamber, the absorbed dose to water at the reference depth z_{ref} is given by 1.14. The reference conditions could be found in Table 10.II of IAEA-398 [14].
The values for $k_{Q,Q'}$ should be obtained by direct measurement of the absorbed dose at the qualities Q and Q', each measured under reference conditions for the user's ionization chamber used for proton dosimetry (see Table 10.III of IAEA-398 [14]).
However, at present no primary standard of absorbed dose to water for proton beams is available. Thus all values for $k_{Q,Q'}$ are based on ^{60}Co gamma radiation as the reference beam quality Q'. The notation k_Q denotes this exclusive use of ^{60}Co as the reference quality.
The IAEA-398 protocols recommend the use of cylindrical and plane-parallel ionization chambers as reference instruments for the average absorbed dose, described in the following section.

1.5 Ionization Chambers

Ionization Chambers are devices used as a reference for measuring the average absorbed dose deposited in its (the dosimeters) sensitive volume by ionizing radiation.
A dosimeter can generally be considered as consisting of a sensitive volume filled with a given medium, surrounded by a wall of another medium.
In the context of cavity theories, the sensitive volume of the dosimeter can be identified as the 'cavity', which may contain a gaseous, liquid or solid medium. Gas is often used as the sensitive medium, since it is a relatively simple electrical medium for collection of charges released in the sensitive medium by radiation.
The cavity diameter of a plane-parallel ionization chamber or a cavity length of

the cylindrical ionization chamber, should not be larger than approximately half the reference field size.

The measurements could be absolute because allow the direct calculation of the absorbed dose or relative because they go back to dose measurement but after calibration with absolute dosimeters.

Among the different geometries, the parallel plate geometry is the most widely used and it consists of two parallel plates maintained at opposite electric potentials (Fig.1.6), with variable dimension depending on the application for which it must be used.

The residual range R_{res} at a measurement depth z is defined as:

$$R_{res} = R_p - z \tag{1.15}$$

where R_p is the practical range, defined as the depth at which the absorbed dose beyond the Bragg peak or SOBP falls to 10% of its maximum value, and z is the depth of measurement.

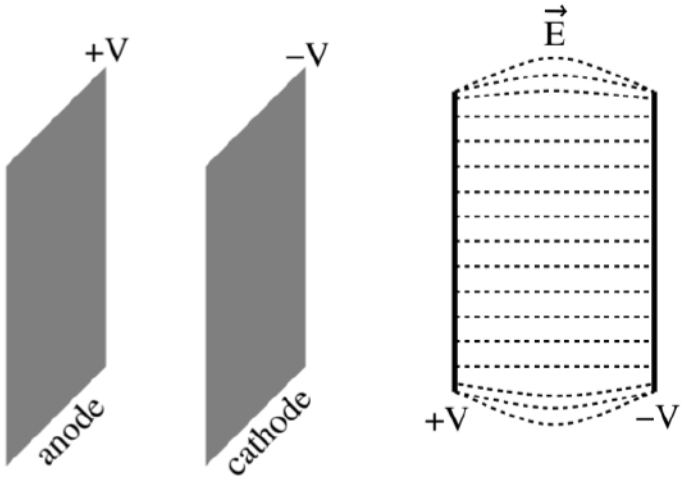

Figure 1.6: Parallel plate ionization chamber and a two dimensional view of electric field inside its active volume.

Plane-parallel chambers, figure 1.6, can be used for reference dosimetry in all

proton beams, but must be used for proton beams with qualities at the reference depth $R_{res} < 0.5$ g cm^{-2} while cylindrical ionization chamber should be used for proton beams with qualities at the reference depth $R_{res} > 0.5$ g cm^{-2}.
For these chambers, the reference point is taken to be on the inner surface of the entrance window, at the centre of the window.
The main characteristics required for a ionization chamber are:

1. leakage current not higher than a fraction of picoAmpere;
2. collection efficiency greater than 99%;
3. time stability and independence on energy of the beam.

The working principle of ionization chambers is based on the measure of the ionization produced by radiation in gas, usually air. The radiation passing through the gas ionizing molecules and the charge pairs produced will drift with constant velocity in opposite directions because of the uniform electric field applied to the electrodes. The drift of the positive and negative charges represented by the ions and the electrons constitutes an electric current, which can be measured.
As the voltage difference between the electrodes of an ionization chamber exposed to a constant radiation is increased from zero to a higher values, the resulting electric field begins to separate the ion pairs more rapidly, and ion recombination is diminished The positive and negative charges are also swept toward the respective electrodes. The ionization current increases, first linearly with voltage and later more slowly, reducing the amount of the original charge lost, until it finally approaches asymptotically the saturation current for the given radiation intensity. Therefore, the saturation current is the measured current under the condition that all the ions produced in the chamber by the radiation are collected by the electrodes. The curve which represents current as a function of the applied voltage is called the saturation curve, figure 1.7.
In some cases saturation current cannot be reached in the ion chamber, mainly due to recombination effects of some positive and negative ions within the gas.
The probability that an ion pair recombines in the chamber volume, depends on the concentration of positive and negative ions at a given location in the chamber

and on the ion interaction time.
The number of ions per unit volume dN/dV lost for recombination per unit time, dt, is called recombination rate and can be found from:

$$\frac{d}{dV}\left(\frac{dN}{dt}\right) = \alpha C^{+}C^{-} \tag{1.16}$$

where α is a constant of proportionality called recombination coefficient, and C^{+} and C^{-} are, respectively, the positive and negative ion concentrations. Equation 1.16 can be written in terms of the amount of charge lost for recombination $q = eN$ and as a function of the positive and negative charge densities $\rho^{+} = eC^{+}$ and $\rho^{-} = eC^{-}$, where e is the electron charge.

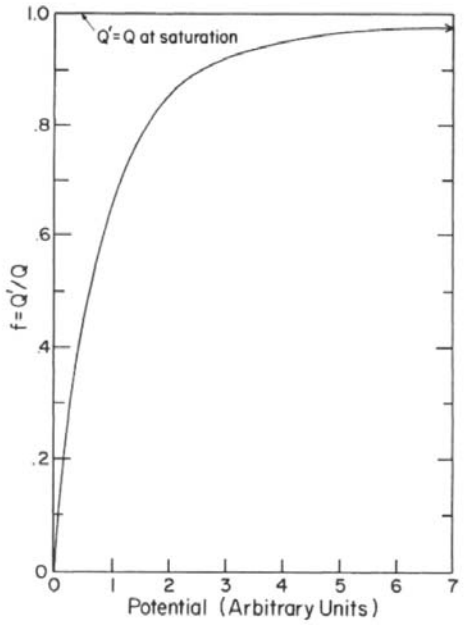

Figure 1.7: Typical saturation curves of an ionization chamber.

The rate at which charge is lost for recombination is:

$$\frac{d}{dV}\left(\frac{dq}{dt}\right) = \frac{d\rho}{dt} = \frac{\alpha}{e}\rho^{+}\rho^{-} \tag{1.17}$$

Both the exact ions concentration at a given point in the sensitive volume and

the interaction time are directly related to the applied voltage V, to the electrode separation d, and to the positive and negative ions mobility in the chamber gas. Due to the recombination effects, the current measured with the ionization chamber is less than the current produced at the saturation.

A possibility to reduce this effect is to further increase the applied potential to eliminate the recombination effect. This solution is not possible because of the electrical breakdown of insulators and for the gas multiplication in which the free electrons gain enough kinetic energy from the electrical field within their mean free path in the gas to ionize the next atom they encounter. A consequential effect could be an extra ionization.

The ratio between the charge measured Q' with the ionization chamber and the charge produced Q at the saturation, due to the recombination effects is given:

$$f = \frac{Q'}{Q} \tag{1.18}$$

f is named collection efficiency and depends on the distance between the electrodes, the collection potential, exposure time, and exposure conditions.

In the sensitive volume of a ionization chamber, positive ions drift toward the cathode while negative ions drift towards the anode with drift velocities proportional to the electric field E in the chamber, (for positive ions the velocity is $v^+ = k^+E$ while for negative ions $v^- = k^-E$).

In air and in other electronegative gases characterized by the tendency to form negative ions with high electron affinities, free electrons produced by ionizing radiation quickly attach to a gas molecule, resulting in a heavy negative ion. In inert gases, electrons do not combine with gas molecules, thus the negative charge carriers are free electrons with mobility k^- about three orders larger than k^+. The ion mobility greatly influences the recombination rate in the chamber, in fact, the ions with high mobility have less time to interact. The consequence is a reduction of the recombination effects.

The total effect of ion recombination is a combination of initial and general recombination and each contribution will be described in following section.

1.5.1 Initial recombination: Jaffè's theory

Initial recombination occurs when positive and negative ions formed along the same track recombine.

It is of major importance when the ion density in the tracks is large. This loss mechanism is dependent only on the local conditions along individual tracks and does not depend on the rate at which such tracks traverse the detector volume. Therefore, initial recombination is independent of dose rate but it depends on ion density within the tracks.

The measurable parameters associated with initial recombination give information about the local density of ions created in the tracks of the ionizing particles in small volumes of the traversed medium and can be correlated with the linear energy transfer (LET) or with other parameters describing radiation quality.

The model of the initial recombination which will be described in this section, has been developed by Jaffè. The experimental studies of proton ionization and α particle ionization in air conducted by Jaffè have been published by the same author in [15].

Jaffè's theory can be applied successfully to ionization caused by slow, heavy charged particles in gases.

The theory has also been widely applied to recombination in liquids, and good agreement with experiment has frequently been observed.

Jaffè's solution was based on a constant linear ion density, N_0 $[ionpairs/cm]$, along the track, a Gaussian radial distribution of ion density, starting from an initial mean-square radius, b, and widening by diffusion, and a fixed angle ϕ between the axis of the track and the uniform collecting field, E $[volts/cm]$, [16].

For the proportion of ions that scape from a column, Jaffè obtained the expression:

$$\epsilon = \frac{i}{I} = \frac{1}{1+gf(x)}x = \left(\frac{bk}{2D}Esin\phi\right)^2 g = \frac{\alpha N_0}{8\pi D}f(x) = e^x\frac{i\pi}{2}H_0(ix) \qquad (1.19)$$

where

- i is the measured ionization current;
- I the saturation current, α is the coefficient of recombination;

- D the diffusion coefficient of the ions;
- k is their average mobility;
- $H_0(ix)$ is the Hankel function

If, under given physical conditions, α, k, D and b are constants for a particular gas under given physical condition,as one can see from eq.1.19 the collection efficiency ϵ is a function of g and x.
Jaffè gave a series of experimental values of g appropriate to polonium α particles in various gases at pressures from 1 to 8 atm [16]. For other charged particles such as protons, the value of g, got by Jaffè for polonium α particles, can be multiplied by N_0'/N_0, where N_0' is the mean linear ion density of the particles in question and N_0 is the value for polonium α particles, (more datails are reported in [16]). The experimental results of Jaffè, have been confirmed by other experimental studies of proton ionization and α particle ionization in air, oxygen (in litterature see [17]).

1.5.2 General recombination: Boag-Wilson theory

General (or volume) recombination occurs when ions produced in different tracks recombine each other on their way to the collecting electrodes. The amount of this type of recombination depends on how many ions are created per unit volume and per unit time, consequently, general recombination is dose-rate dependent.
The investigation of volume recombination in parallel plate ionization chambers has a long history in physics. Rutherford and Thomson [18] reported the first measurements of the saturation curve, and Thomson [19] proposed a theory that may be used to study the details of the saturation curve in terms of the applied voltage, ionic mobilities, volume recombination, and self fields (space-charge effect) of single positive and negative charge carrier. Nevertheless, the Thomson differential equations are mathematically complex and analytical solutions, valid for the entire saturation curve, have been not been found.
Boag and Wilson [20] have developed simpler theories in order to describe the saturation curve near full collection efficiency for most practical applications.

The theory assume the positive ion density between the electrodes rises linearly from zero at the positive plate to a maximum at the negative plate, while the negative ion density varies linearly in the opposite direction. The model should be valid in the region near to the saturation.
Following this theory, the collection efficiency for an ionization chamber filled with electronegative gas and radiated from a pulsed beam with pulses of short duration (microseconds or less) compared with the transit time of ions across the chamber and slow enough repetition rate with respect to time of charge collection, is given by:

$$f = \frac{1}{u}\ln(1+u) \tag{1.20}$$

$$u = \frac{\alpha/e}{k_1 + k_2}\rho\frac{d^2}{V} \tag{1.21}$$

where ρ is the initial charge density of positive or negative ions created by a pulse of radiation (C/cm^3), d is the electrode spacing, α a recombination coefficient, k_1 and k_2 positive and negative ions mobility and V the voltage.

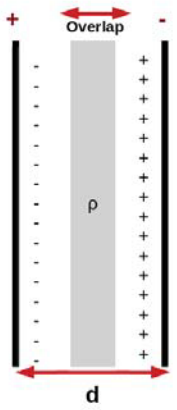

Figure 1.8: Overlap of positive and negative charge when the ionization chamber is exposed to a pulsed radiation of short duration.

Boag-Wilsson theory could be applyed when ionization chambers are exposed to

a pulsed radiation of short duration.
A pulse is short when the pulsed duration is at least of microseconds (or less), compared with the transit time of the slowest ions across the whole gap between the electrodes.
In this case, the total ionization per pulse, being produced in a negligible time interval, begins to drift after the end of the pulse. The recombination (in a plane parallel chamber) occurs when positive and negative charge distributions is overlapped during the collection of an instantaneous pulse of ionization, (figure1.8).
Furthermore, since general recombination increases with dose rate, when ionization chambers are exposed to laser driven ion beams, characterized by high dose rates, the recombination effect due to general recombination is predominant, respect the initial recombination.

Chapter 2

Laser-Acceleration and the ELIMED project

More than half a century ago, Veksler (1957) introduced the concept of *coherent acceleration* of particles as a mechanism where the accelerating field on each particle is proportional to the number of particles being accelerated[21], contrary to traditional techniques. Additional elements in Veksler's vision of future accelerators included the automatic synchrony between the particles and the accelerating field, the localization of the latter inside the region where the particles are and the production of quasineutral groups with large numbers of energetic particles.
These features, today, are obtained in the acceleration of ions from plasma produced by the interaction of ultra-intense (higher than $10^{18}\ W/cm^2$) and short pulse (tens to hundreds of fs) lasers on thin solid targets[22].
In the last decades, a growing interest of the scientific community has led to the development of several projects aiming to demonstrate the possible use of laser-driven beams for multidisciplinary applications.
So far a number of different acceleration regimes, for instance Target Normal Sheath Acceleration (TNSA)[23][24], Radiation Pressure Acceleration (RPA)[6], Break-Out Afterburner Acceleration have been investigated. Several international collaborations and experimental campaigns have been launched aiming to explore the feasibility of using laser-driven sources for potential medical applications and

many research centers have been involved in the investigation of laser driven ion therapy and applications, as for instance the Queens University Belfast Consortium, the OncoRay National Center for Radiation Research in Oncology, Dresden, The Munich Centre for Advanced Photonics (MAP), the ion Acceleration Program at BNL ATF and UCLA.
A large number of experimental results have been reported in literature[25],[26],[27], [28],[29].
Some of the peculiarities of these new particle beams are very promising for fundamental research as well as for multidisciplinary applications, including the medical field. Nevertheless, the non conventional characteristics of laser-accelerated ion beams such as the very high peak current and dose rate, the broad energy and angular distribution, and the low shot-to-shot reproducibility require development of innovative devices in order to make these beams suitable for different applications. In this framework, a collaboration between the INFN-LNS (National Institute for Nuclear Physics - Laboratori Nazionali del Sud, Catania, Italy) and the ASCR-FZU (Institute of Physics of the Czech Academy of Science) has been established in the last years. The main purpose of the collaboration is to realize a transport beam line, named ELIMED, for laser accelerated ions. The ELIMED beam line represents the section of the ELIMAIA (Multidisciplinary Applications of laser-Ion Acceleration) user-oriented beam line addressed to the transport, handling and dosimetry of the laser-driven ion beams allowing the achievement of stable, controlled and reproducible beams which will be available for all the users interested in multidisciplinary and medical applications of such innovative technology with high energy laser-accelerated beams.
In this chapter a description of the new acceleration techniques, together with an overview of the state-of-the-art of the different research centers where studies of laser- driven ion sources for medical therapy are carried out, and a description of the ELIMED beam line, will be presented.

2.1 Laser-Acceleration for Potential Medical Applications

Laser technology and laser-plasma physics as beam accelerators are advancing rapidly. Outstanding progress has been made in high-power laser technology in the last decade with laser powers reaching Petawatt (PW) level.
Currently, there are several PW lasers built or being built around the world.
In this section an overview of the state-of-the-art of the different research centers available around the world and their activities related to the development of laser-driven ion sources for medical therapy will be given.
A more complete and extensive review of the different research centers and of research projects along with the specifications of the laser systems and technical approaches involved can be found in [30],[31],[32].

Queens University Belfast Consortium

Researchers activities from Queens University Belfast (QUB), University of Strathclyde, Imperial College and Rutherford Appleton Laboratory, are currently carried out with the aim to develop laser-driven ion sources for medical applications.
The project aims to obtain controlled, all-optical acceleration of dense bunches of protons and other low-Z ion species, in the 60 - 300 MeV/nucleon range of interest for therapy of deep-seated cancer. A number of different laser acceleration protocols will be studied to increase the energy of the ion beam, as for instance, the Radiation Pressure Acceleration (see section 2.4.2).
A unique property of laser-driven ion beams is the ultrashort pulse. Ions are emitted in bursts of ps or fs duration at the source and their clinical use may result in dose rates up to 9 orders of magnitude higher than the one normally used in conventional therapy.
Dose rate can be a critical parameter affecting radiation biological responses.
The biological effects of ions at such extreme doses are still unknown, and need to be carefully assessed. In parallel to the source development, the collaboration is pursuing a program of investigations of the dynamics of cellular response to

ion irradiation and damage at these unprecedented dose rates. Pioneering experiments exploring the biological effects on cells at dose rates $>10^9$ Gy/s have been carried out at QUB's TARANIS laser, and recently using the PW laser system at RAL(Rutherford Appleton Laboratory) [33][34].

Laboratoire d'Optique Appliquée-LOA, Palaiseau, France

Laboratoire d'Optique Appliquée (LOA) hosts the multi-TW fs pulse SAPHIR laser system. The corresponding project, called SAPHIR, involves academic (groups from CNRS and CEA), medical groups (from Institut Gustave Roussy and Institut Curie) and industrial partners (Amplitude Laser Technologie, Imagine Optics and Dosisoft). Proton beams with energies in the few tens of MeV are produced by a a 200 TW laser and controlled to allow radiobiological studies.
Biological studies have been performed in order to get a stronger confirmation on the dosimetry protocol. Radiobiological effects of laser-accelerated pulsed protons have been assessed on human colorectal cancer and a preliminary study of the DNA damage foci from SAPHIR accelerated protons have been carried out [35][36].
The studies performed by the researchers involved in this project, have shown that the range of energy, the charge per bunch, and the repetition rate of the laser, satisfy many of the medical requirements for medical application [37][38].
Furthermore, Monte Carlo calculations have been found to be in very good agreement with dose measurements.
Treatment planning for laser accelerated high energy electrons has already been carried out for prostate irradiation and further studies are scheduled for other type of cells.

Ion Acceleration Program at BNL ATF

Only two facilities worldwide operate picosecond carbon dioxide (CO_2) lasers for advanced accelerator research, ones is the ATF (Accelerator Test Facility) at BNL (BROOKHAVEN Nation Laboratory) the other is at UCLA's (University of California, Los Angeles) Neptune laboratory to develop a next-generation plasma beat-wave accelerator.

The BNLs ATF is a user facility open for international collaborations. The CO_2 laser offers new opportunities to explore ion acceleration using the Shock Wave Acceleration (SWA) regime from gas jets.
The SWA experiment at ATF has been carried out in close partnership with Imperial College (London) and Stony Brook State University (New York).
The project has the aim to upgrade to $50-100$ TW peak power range of current CO_2 laser in order to obtain ion beams with kinetic energies suitable for medical applications.
The upgrade underway at ATF is a three-year plan and includes dedicated experimental space for applying laser-driven ion beams to user experiments with biological samples and living tissue[39][40].

OncoRay-National Center for Radiation Research in Oncology, Dresden

The Dresden OncoRay center has recently achieved an important step towards compact radiation facilities for cancer treatment.
The center operates in collaboration with three other research center: Forschungszentrum Dresden Rossendorf (FZD), University Hospital Dresden and TU Dresden.
The high-power laser DRACO (Dresden laser acceleration source) at the FZD generates protons, accelerating them on a very short scale of less than ten micrometers.
The Dresden group has irradiated cancer cells with protons of 20MeV, produced by the ultra-short pulse 150 TW laser system at FZD . They have investigated the impact of radiation on cells under controlled conditions. Furthermore, they have developed dosimetry devices enabling to measure online, the dose of the irradiated cells[41]. The dose of the irradiations at the FZD ranged between 1.5 and 4Gy.

Laser-Acceleration Studies at JAEA in Japan

Electron and proton acceleration with lasers has been an active area of investigation at the Kansai Photon Science Institute (KPSI) of JAEA for several years.
Researchers at KPSI have shown a strong interest in the development of integrated laser-driven ion accelerator systems (ILDIAS) that can be used for laser-driven ion beam radiotherapy (L-IBRT). Researchers of KPSI, in collaboration with the

University of Bologna, the University of Milano and INFN, have been performed simulations of a hybrid ILDIAS (i.e., HILDIAS). ILDIAS will be the basic laser-driven ion beam (Laser systems produce peak powers up to PW) "machine" (i.e., distinct from applications) which is analogous to a synchrotron.
The energies accessible nowadays, up to tens of MeV/u, offer the possibility to engage in a wide range of the ILDIAS applications, which aims to exploit the therapeutic advantages of ion-tissue interaction in matter with more compact footprints for production and steering of energetic ion beams inside the patient in comparison to the current commercially available solutions.
First radiobiological investigations with in vitro cell cultures recently demonstrated the feasibility of meeting all prerequisites for biomedical sample irradiation at accessible low proton energies of few MeV/u, including rigorous absolute dosimetry for controlled delivery of clinically relevant fraction-like doses of few Gy in multiple or single laser-shot [42].
Furthermore, new milestones on the near horizon include small-animal in vivo studies and biological experiments addressing the implications of the unique features of laser-driven ion beams, in terms of very elevated local dose rates (towards Gy/ps or more) and, more importantly, the intriguing possibility to produce multiple ion species (e.g.,protons and carbon ions) of different biological effectiveness in the same laser-target interaction.

The Munich Centre for Advanced Photonics (MAP)

The Munich Centre for Advanced Photonics (MAP) is a research cluster funded by the German government since 2000. MAP draws on recent developments in high-power laser technology and emerging secondary sources of laser-driven X-rays and laser-driven particle beams.
Researchers at MAP are currently investigating the required physical, technological and biological basis for laser-based radiation therapy with proton or carbon ion beams. They focus on these issues both from a fundamental physics point of view as well as with respect to applied medical physics and radiobiology with the long term goal of developing a laser-based particle therapy unit[43][44].

When higher proton energies (250 MeV) will be available, radiobiological investigations will shift to pre-clinical studies in mice and finally towards clinically relevant setups.
Appropriate methods for beam delivery including lateral and axial beam shaping for highly pulsed beams and the corresponding treatment planning strategies are being developed in order to design clinical treatment units for laser-driven particle beams. The mission of MAP is to create an unparalleled infrastructure in photonics, on the long run sustained by the Centre for Advanced Laser Applications (CALA), and a lasting bridge between physical and biomedical sciences.
The Centre for Advanced Laser Applications(CALA) accommodates two high tech laser sources ATLAS-3000 (Advanced Ti:Sapphire Laser 3000 Terawatt) and PFS-pro (Petawatt Field Synthesizer), as well as the Compact Light Source (MuCLS). A combination of a compact electron accelerator and lasers for the generation of X-rays, are domiciled in CALA[45].
The notified experiments at CALA are supposed to explore the physical basics for a later use in medicine.
Relativistic electrons are used for the generation of brilliant X-rays for imaging ions for research towards therapy (LION).
Furthermore, thanks to the BIRD experiment, an experimental station for trace analysis of tumor-relevant metabolites in blood and breathing air with the help of laser light will be also available.

2.2 The ELIMED project

The interest of scientific community in a new particle acceleration technique has led to establish a collaboration between INFN-LNS in Catania and the ASCR-FZU (Institute of Physics of the Czech Academy of Science), within the ELI-Beamlines (Extreme Light Infrastructure-Beam lines) project.
The main aim of the collaboration is to provide a user-oriented facility where accurate dosimetric measurements and radiobiology experiments can be performed with high energy laser-accelerated ion beams.

The realization of a high-power laser facility, ELI-Beamlines, started in 2012[46] and it is dedicated to generation and application of the laser produced photon and particle beams.
ELIMAIA (ELI-Multidisciplinary Applications of laser-Ion Acceleration) is the user-oriented beam line of the ELI-Beamlines facility, dedicate to the multidisciplinary experiments with laser-accelerated protons and ions.
ELIMED beam line represents the section of the ELIMAIA beam line addressed to transport, handling and dosimetry of the laser-driven ion beams allowing to deliver reproducible beams that, starting from 2018, will be available for the users interested in multidisciplinary and medical applications of such innovative technology.
In the next section, 2.2.1, the ELIMAIA beam line will be described.

2.2.1 ELIMAIA: a user beam line

ELIMAIA is the target area, at the ELI-Beamlines facility, dedicated to the multidisciplinary applications of the secondary sources produced by the interaction of a PW-class laser with solid target.
The proposed technological and scientific solutions for the implementation of the ELIMAIA beam line is the result of a complex investigation carried out in the last years with the main goal to provide, stable, characterized and tunable ion beams, to a broad international community of users for multidisciplinary applications, as well as for fundamental science.
The ELIMAIA beam line consists of two main subsystems: the Ion accelerator section and the ELIMED section. The first subsystem consists of a plasma mirror chamber, laser diagnostics and a main interaction chamber. In the plasma mirror chamber the laser beam is cleaned from sub-nanosecond pre-pulses. The beam then continues its propagation towards the laser diagnostics section where the laser parameters, such as laser energy, pulse duration, contrast ratio, and wave-front, are measured. After the diagnostics section, the laser beam is sent into the interaction chamber and focused onto the target by an off-axis parabolic mirror.
The ion beam accelerated in the laser- target interaction will be transported thanks

to the ELIMED subsystem down to the irradiation point.
A 3D drawing of the ELIMAIA beam line inside the experimental hall E4 at ELI-Beamlines is shown in figure 2.1.

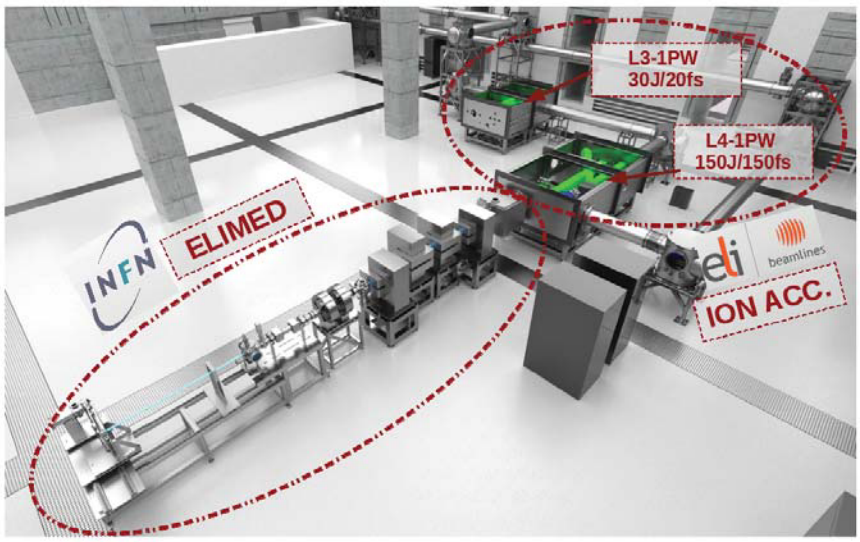

Figure 2.1: 3D drawing of the ELIMAIA beam line showing the ELIMAIA ion acceleration section and the ELIMED section.

2.2.2 Overview of the ELIMED beam line

Laser-driven ion beams, available so far are characterized by high intensities, several species with multiple charge states, broad energy spectra and energy-dependent angular distributions.
Thus, in order to make these beams suitable for multidisciplinary and medical purposes, it is necessary to control ion energy, angular aperture, fluence, spot size, dose distribution and reproducibility of the beam delivered [47][48].
The ELIMED beam line consists of two main sections[49]: the first one, in vacuum, is dedicated to transport, collection, selection and diagnostics of the optically accelerated beam; the second one, in air, is addressed to relative and absolute dose measurements, figure 2.2. The transport beam line consists of three main elements: a collection system, composed by a set of permanent magnet quadrupoles (PMQs)

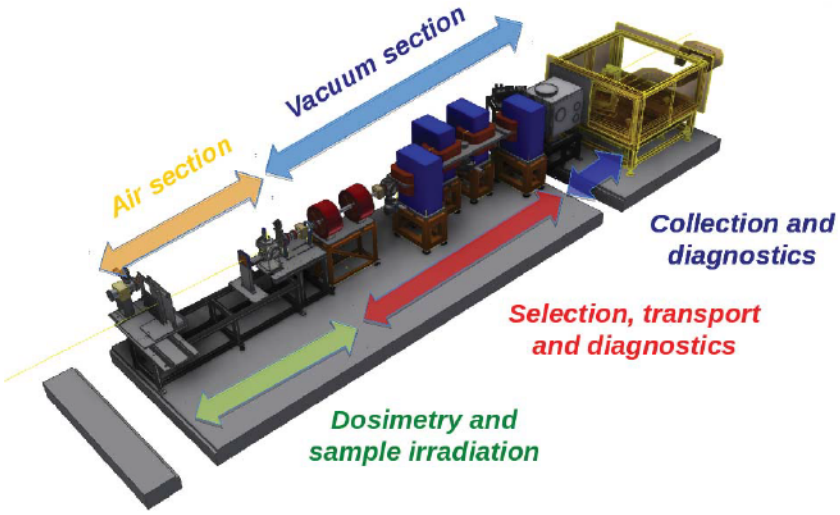

Figure 2.2: Scheme of the ELIMED section of ELIMAIA.

that will be placed close to the laser-interaction point, an energy selection system (ESS) based on four resistive dipoles, and a set of conventional electromagnetic transport elements.

The beam line has been designed to transport and select laser-driven ions up to 60 MeV/u, delivering a stable beam in terms of energy spread, angular divergence and variable beam spot size, [50],[51],[52].

Beam size, shape and any possible misalignment will be controlled using a doublet of resistive quadrupoles, two steerers and collimators.

The aim of the focusing system is to collect the accelerated particles within a certain energy range, reduce the angular divergence of the beam and inject the beam in the selection system which will stop the particles outside the energy range of interest.

The beam coming out from this part of the beam line (PMQs+ESS) will have characteristics closer to conventional beams and, hence, easier to be transported and shaped with conventional magnetic lenses, such as resistive quadrupoles and steerers. They will be placed in the last part of the in-vacuum beam line.

Ion collection system: Permanent Magnet Quadrupoles The collection system consists of five quadrupoles, whose characteristics are reported in table 2.1, [51],[53] .

The system collects a wide range of ion energies,from 3 MeV/u up to 60 MeV/u, and inject a given beam component in the ESS.

Therefore, in order to optimize the beam injection in the energy selector system, optics simulations of the ion collection system have been performed. The simulations have allowed defining geometrical configurations in terms of number of quadruple and distances between each one quadrupol, to ensure an acceptable transmission efficiency for any specific requirements (in particular the PMQ bore is 36 mm, with a strong field gradient and high uniformity).

Considering these requirements, the quadrupoles have been designed on a standard trapezoidal Halbach array [54][55] surrounded by two external hybrid arrays made of rectangular magnetic blocks and iron.

The inner array is mainly responsible for the field quality of the quadrupole whereas the external array is necessary to increase the volume of the permanent magnet material and to reach the required field gradient.

A scheme of the PMQs layout is shown in figure 2.3.

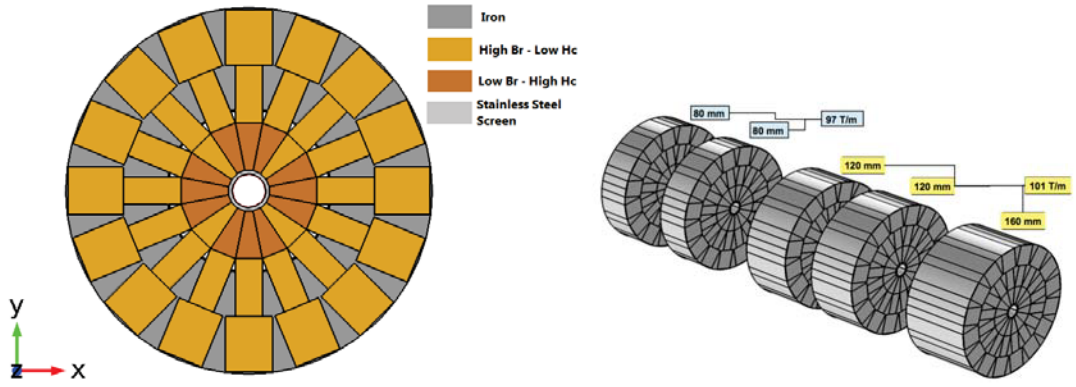

Figure 2.3: PMQ layout. The different colours represent the different materials used.

This layout results to be robust with a good field quality.

The field analysis, described in [56], shows a gradient uniformity better than 2% and integrated field uniformity better than <0:3% within a radius of 12 mm [51]

[53].

Table 2.1: PMQs main features.

No. of PMQs	Geometric length(mm)	Field gradient(T/m)	Bore diameter (mm)
1	160	101	30
2	120	99	30
2	80	94	30

Energy selector system The ESS is based on four resistive dipoles with alternating magnetic field and it is realized in order to use a single reference trajectory. The theoretical reference trajectory of the ESS and its main trajectory parameters are shown in figure 2.4, [52], described in [57].

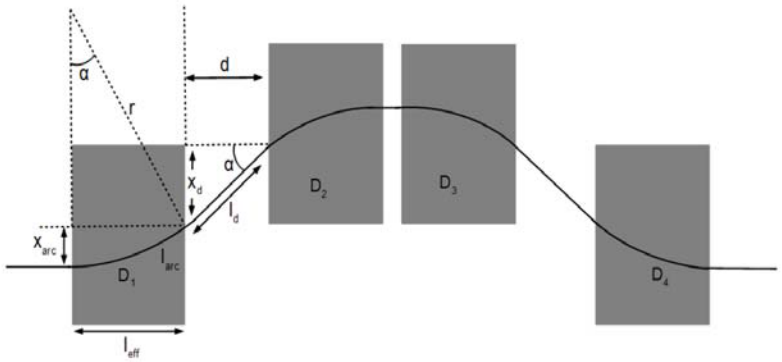

Figure 2.4: Scheme of the ELIMED ESS.

Analytically, using the main trajectory parameters shown in figure 2.4, it is possible to define the characteristics of the ESS, in terms of radial and longitudinal dimensions of each dipole, field strength and selection slit size, necessary to have the required energy resolution. In fact, the bending radius r and the bending angle α of a dipole are both function of the particle momentum. Hence, the energy can

be written using the following relativistic equation:

$$\sqrt{\left[\frac{qc(\Delta x - d\tan\alpha)}{2(\frac{1-\cos\alpha}{B})}\right]^2 + M_0^2c^4 - E_0} \tag{2.1}$$

which represents the calibration equation of the ESS, being δx the radial displacement of the beam at the centre of the device and q, M_0 and E_0 the characteristics of the ion to be selected. The derivative of the previous equation times the slit aperture size s gives the energy resolution of the device.
In figure 2.5 are shown the trajectory within the four dipoles (coloured lines).

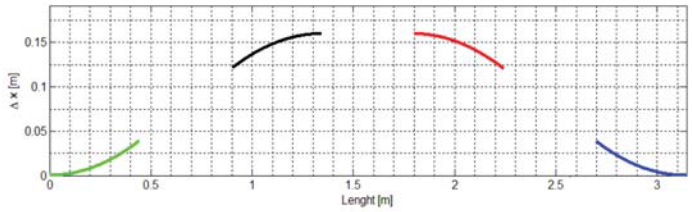

Figure 2.5: Trajectory within the four dipoles.

The main features are listed in table 2.2. The total geometrical length of the system is about 3 m m and the reference particle path length is 3.168 m with a maximum radial deflection of 160 mm at the center. The selection path guarantees a fixed energy resolution of about 5% if a 4 mm aperture slit is used.
The resolving power does not depend on the particle energy or ion species. In order to deflect particles with a specific energy along the reference trajectory the magnetic field has to be changed. It will be varied between 0.085 and 1.2 T, which corresponds respectively to an energy ranging between 3 and 350 MeV for protons and between 3 MeV/u and 100 MeV/u for carbon ions (C^{+6}). The proposed layout allows to vary the energy resolution by changing the slit aperture size, which is an advantage particularly when selecting higher energies: in this case, indeed, laser-driven particles are less abundant, and they can be selected with a broader spectrum (corresponding to a bigger slit aperture) to keep the transmission efficiency acceptable.

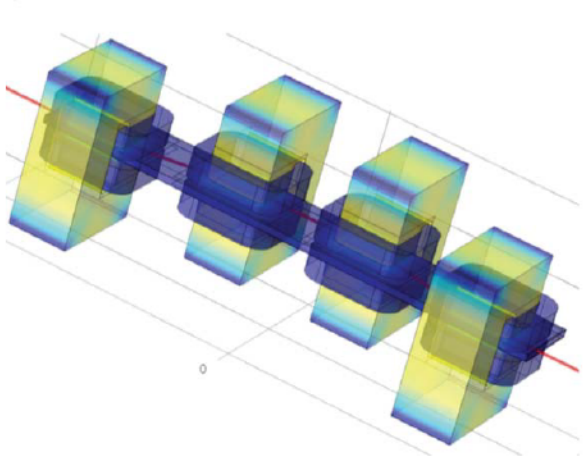

Figure 2.6: Energy selector layout. In red the reference particle trajectory.

The pole shape has been designed in order to fulfill the requirements of table 2.2. It ensures the required field uniformity and effective length for the whole range of magnetic fields [58]. The whole system is shown in figure 2.6 where it is also shown the reference particle trajectory.
The system is provided with two collimators upstream and downstream the selection, necessary to avoid spatial mixing of particles with large divergence and to define the energy selection at the exit of the system. They have 30 mm diameter aperture and they will be placed 200 mm upstream and downstream, respectively, the ESS[59].

Table 2.2: ESS dipole features.

Dipoles	B field	Length	Effective length	Gap
4	0.085–1.2 T	400 mm	450 mm	59 mm
GFR	B uniformity	Curvature radius	Drift length	Max J
100 mm	$< 0.5\%$	2.593 m	500 mm	2.53 A/mm^2

Diagnostics detectors

In order to obtain on line information on proton and ion beam parameters, different diagnostics detectors will be placed in the ELIMED beam-line. The first diagnostics section will be placed downstream the collection system at about $2m$ from the source. It will consists of two different detectors:

- A detector, based on the well-known pepper pot method, specifically designed and optimized for single shot emittance measurement of the laser-driven proton beam, placed just right after the PMQs system.
- A diamond detector, used in Time Of Flight (TOF) configuration, providing particle energy spectrum and fluence measurements.

The second diagnostics section will be placed downstream the in-vacuum beam line after the energy selection and the conventional transport elements, i.e. at about 9m from the source. It consists of a detector performing TOF measurements for the on-line characterization of the beam coming out of the energy selector system. A schematic view of the ELIMED beam line together with the diagnostics positions along the beam-line are shown in figure 2.7.

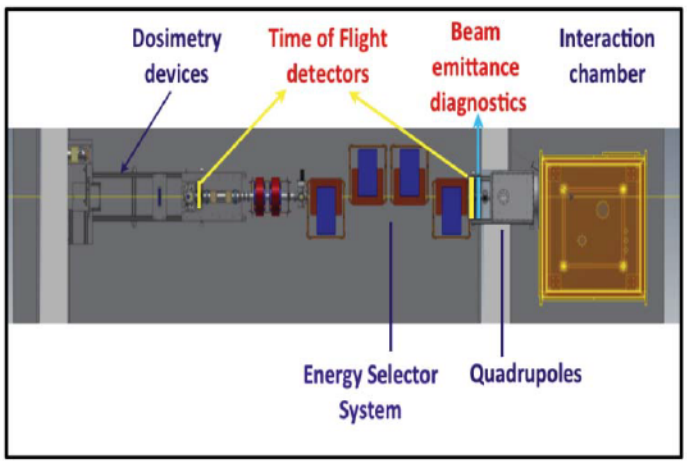

Figure 2.7: Schematic view of the ELIMED beam line where is shown the position of the diagnostics elements along the beam line.

TOF detectors

In order to perform TOF measurements along the ELIMED beam line, two Chemical Vapour Deposition (CVD) diamond detectors have been chosen: a polycrystalline (pCVD) and a single crystalline (sCVD) diamond, [60], [61], [62].
The pCVD has been designed for high intensity loss measurements well above 10^5 particles per bunch and has a linear response for very high intensity up to 10^9 particles per pulse. The sCVD beam loss detector has also been optimized for high intensities and high irradiations. It has also a good time resolution in the sub-nanoseconds range and an excellent signal-to-noise ratio making this detector particularly suitable for beam loss measurements with good energy resolution.
The pCVD will be used to perform the TOF measurements at about 2 m from the source, i.e after the PMQ system, and the sCVD will be used to measure the TOF of the proton distribution selected by the ESS downstream the in-vacuum beam line at about 9 m from the source.

Beam emittance system

In order to reconstruct the beam flux density as respect the spatial position, giving information for the emittance estimation, a beam-emittance system will be used.

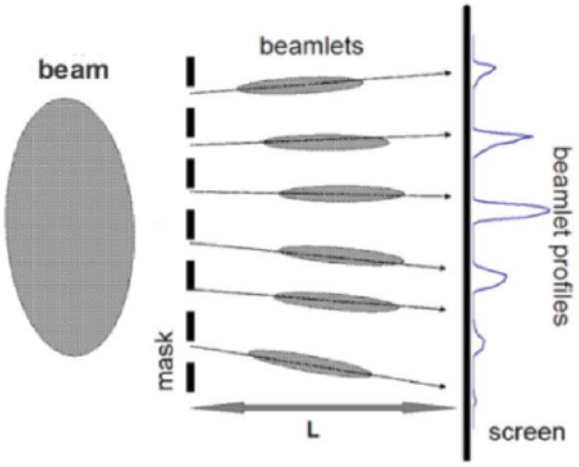

Figure 2.8: Emittance diagnostics set-up based on Pepper-Pot method.

The working principle is based on the pepper-pot method and can provide simultaneous information about beam profile and angular divergence in a single measurement allowing the emittance measurement. A typical setup of a Pepper-Pot device is shown in figure 2.8. The emittance provides a quantitative basis for describing the quality of a particle beam in two-dimensional phase-space i.e. the collection of the space and momentum coordinates of the particle distribution and it is defined as the ellipse area A enclosing the beam particles in a determined direction (figure 2.9).
All particles within the ellipse in the phase space always remain inside of it while moving. During the particle motion, only the ellipse shape can changes, this indicates the convergence or divergence condition of the beam, while the area A remains constant.
A metallic mask, provided with a set of holes is used to sample the initial transverse phase space distribution. The mask must be thick enough to stop the beam but, at the same time, it must be as thin as possible to avoid cutting off diverging beamlets (with the consequent loss of information on divergency). The total intensity of each beamlet as a function of the position of the hole axis permits to extract the spatial profile of the beam. Moreover, the profiles of each individual beamlet can be used to extract information on the angular distribution of the beam at the position of the hole. With the pepper-pot device it is possible to determine the emittance, measuring the beamlets position on the screen and divergence that is the slope of the velocity component as respect to the propagation direction and it is obtained from the width of the correspondent current density curve measured on the screen.
The system will be composed by the following components:

- a pierced mask;
- a micro-channel plate coupled a phosphor screen;
- a CCD camera

The beamlets images, that will be projected on the scintillator screen, will be reflected by the 45^0 mirror and observed by a CCD camera placed outside the

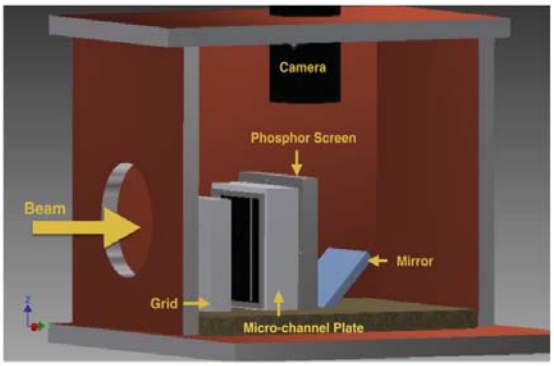

Figure 2.9: Pepper-pot detector scheme.

chamber. The system, composed by a grid, a MCP and a phosphor screen, will be mounted in a box with a linear motion feed-through. The pepper-pot device,therefore, will be moved on or out of the beam using a control remote system.

Absolute and relative dosimetry

Although the transport elements will allow obtaining beams selected in energy and with small divergence, the beam properties are still far from the typical features characterizing the conventional accelerated beams, from the point of view of the temporal structure.

Indeed, the transported laser-accelerated ion beams will be characterized by very high intensities per pulse, i.e. up to 10^7-10^{10} particles per bunch, and very short temporal profile (ns), compared to 10^8-10^9 particles/s accelerated by conventional clinical machines. This results in an extremely high dose rates, i.e. 10^6-10^9 Gy/min (vs 1-50 Gy/min in conventional proton therapy).

The high laser pulse peak intensity leads to a high dose delivered per pulse. In order to use laser-driven ion beams in hadrontherapy, it is fundamental to control the dose deposition. The high dose released per pulse makes necessary the development of dose-independent system for absolute and relative dose measurement, [49], with a level of accuracy required by absolute dosimetry [14].

In order to perform such kind of experiments, the dosimetric system has to allow

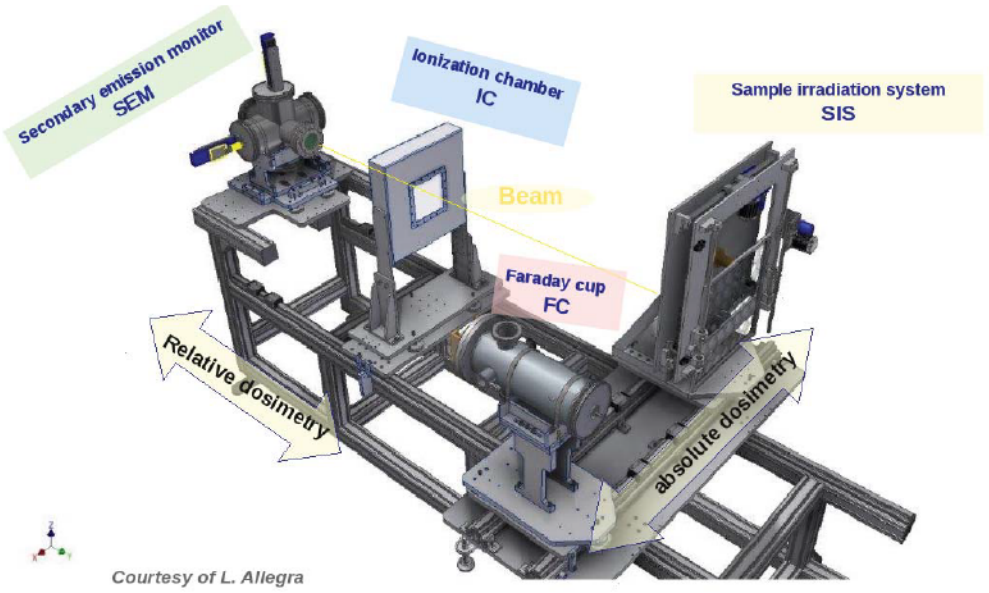

Figure 2.10: A technical drawing of the dosimetric system and the sample irradiation system.

on-line dosimetry measurements with a level of accuracy within 5%.

The dosimetric system, together with the sample irradiation system, represents the key-element of the in-air section of the ELIMED beam line.

It is composed by dose-rate independent detectors which have been specifically designed and realized to work in a typical laser-driven environment, characterized also by a strong electromagnetic pulse [48].

In particular, for absolute dosimetry, a Faraday cup (FC) specifically designed to decrease uncertainties in the collected charge has been realized [63] while for relative dosimetry an electron monitor (SEM) and a multi-gap ionization chamber (IC) will be used.

The FC is an absolute dosimeter with the aim to count and measure the collected charge entering the detector. The FC, together with radiochromic films (RCF), allows extracting the absolute dose in water. RCF are, indeed, used in order to measure the effective beam area and the energy spectrum. Typically, in order to measure the proton spectra, RCFs are used in stack.

The SEM is a thin metallic foil detector, whose working principle is based on

the secondary electron emission (SEE). It will be mounted in a vacuum chamber, placed at the end of the in-vacuum beam line section.
The multi-gap IC is an innovative detector, designed to measure real-time the dose delivered per pulse.
It is an in-transmission double-gap chamber, filled with air, which will be cross-calibrated with the FC absolute dosimeter. The presence of a second gap close to the first one allows correcting for ion recombination effects caused by the very high dose-rate per pulse.
Moreover, a sample irradiation system (SIS) will be installed at the end of the in-air section, allowing the positioning of the cell samples with a sub-millimetric precision, figure 2.10. Each element will be installed on special supports, placed on a removable support and moved along rails from the kapton window down to the irradiation point.
The details of relative and absolute dosimetry will be described in chapter 3.

2.3 Laser interaction with matter

As discussed in section 2.1, many studies and experiments have been performed in the last decades to use the laser-matter interaction as possible alternative to the conventional acceleration methods, for multidisciplinary and medical applications.
High power laser-matter interaction denotes the phenomenon when a laser radiation with intensities ranging from 10^{10} W/cm^2 to approximately 10^{23} W/cm^2 delivers an energy to a target over times from nanoseconds down to few femtoseconds [64].
Electric field of a laser wave with such power is much stronger than a Coulomb field which is responsible for binding electrons and atomic nuclei.
Therefore, a rapid ionization occurs near the target surface and matter is transformed into dense plasma. The collective motion of free electrons and ions determines the properties of the plasma.
The motion of charged particles in electromagnetic field is governed by the Lorentz force [65], [67].

For electron with relativistic momentum $\vec{p_e} = \gamma m_e \vec{v_e}$ the equation is:

$$\frac{d\gamma m_e \vec{v}_e}{dt} = q[\vec{E} + \vec{\nu}_e \times \vec{B}] \tag{2.2}$$

where

$$\gamma = \frac{1}{\sqrt{1 - \vec{v}_e^2/c^2}} \tag{2.3}$$

The direction of the electron motion is given by the ratio between the longitudinal component and the perpendicular component momentum:

$$p_{\parallel} = m_e c(\gamma - 1) \tag{2.4}$$

$$\vec{p}_{\perp} = \sqrt{p_{\parallel}(2m_e c\gamma)} \tag{2.5}$$

In the non-relativistic case ($\gamma \sim 1$), the longitudinal component $p_{\parallel}$ is very small and the electron oscillates in the electric field of the laser wave perpendicularly to its wave vector $\vec{k}$. As $\vec{v}_e$ increases the second term of eq.2.2, $\vec{\nu}_e \times \vec{B}$, becomes more important and the electron starts moving in the direction of $\vec{k}$, [66].

The electron trajectory in the electromagnetic field of a laser pulse depends strongly on the pulse parameters, such as the pulse polarization and its duration.

Another parameter which determines the electron motion in a laser field, is the parameter a_0, [66]:

$$a_0 = \frac{eE}{m_e c\omega_L} = \sqrt{\frac{e}{2\pi^2 m_e^2 c^5 \epsilon_0}}\sqrt{I\lambda_L^2} \tag{2.6}$$

where E is the strength of the laser electric field, ω_L is the angular frequency of the laser wave, λ_L is its wavelength, I is its intensity and ϵ_0 is the vacuum permittivity. The parameter a_0 corresponds to the normalized (with respect to the speed of light c) average oscillation velocity of an electron in the electric field of the laser wave [67].

If $a_0 \geq 1$ the magnetic field component of the laser wave becomes as significant as the electric term and the electron oscillates with a relativistic velocity.

When ultra-short laser pulse begins to propagate in underdense plasma, the Lorenz force, in this case named ponderomotive force, occupy a central role.

This nonlinear force, tends to push electrons against the gradient of the laser

electric field and it is expressed by [66]:

$$\vec{F_p} = \frac{e^2}{4 < \gamma > m_e \omega_L^2} \vec{\nabla}(E_s^2) \tag{2.7}$$

where $< \gamma >$ is the relativistic factor which is averaged over the fast oscillations of the laser fielled and $\vec{(E_s^2)}$ stands for the spatial dependence of the electric field. The plasma oscillates with a typical frequency ω_p, given by [67]:

$$\omega_p = \frac{\sqrt{4\pi n_e e^2}}{m_e} \tag{2.8}$$

where n_e is the electron density, e is the elementary charge and m_e is the mass of the electron.
Plasma frequency describes the speed with plasma electrons can travel through the plasma.
From the macroscopic point of view plasma may be described as a dielectric medium with high polarizability due to coupling between charged particles and an electric and a magnetic fields.
The dielectric function, considering a very short time scale and electron-ion collisions neglible, could be written as:

$$\epsilon(\omega) = 1 - \frac{\omega_p^2}{\omega^2} \tag{2.9}$$

where ω is the driving frequency of an external electric field.
If $k^2 = \epsilon(\omega)\ (\omega^2/c^2)$, it is possible define the dispersion relation of an electromagnetic wave in plasma as:

$$\omega^2 = \omega_p^2 + k^2 c^2 \tag{2.10}$$

where:

- $\omega > \omega_p$ plasma acts as dielectric, k is real and the wave propagates through plasma.

- $\omega < \omega_p$ region where both the wave number k and the index of refraction have imaginary values, thus the wave is exponentially dumped and it vanishes on a distance of the order of skin depth.

- $\omega = \omega_p$ it can be derived the so-called critical density of electrons when the wave is reflected from plasma:

$$n_0 = \frac{\omega^2 \epsilon_0 m_e}{e^2} \tag{2.11}$$

All the laser plasma interactions occur either in the underdense($\omega > \omega_p$) plasma or near the critical density.

2.4 Ion acceleration mechanisms

When a laser pulse irradiates a solid target an overdense plasma slab is formed and several absorption mechanisms can be involved[23].
The absorbed laser energy accelerates and heats electrons in plasma. Moreover, if normal incidence is considered, the ponderomotive force pushes inward the electrons from the rear surface of the target creating a charge separation, which produces an electrostatic field experienced by the ions.
The ions dynamics has been neglected, as they are much heavier than the electrons and therefore not able to contribute within short time scales.
Ions indeed respond to slowly varying electric fields.
Ion acceleration mechanisms can be divided into two groups, according to the target side from which ions are accelerated: *Rear surface acceleration* and *Front surface acceleration*. In figure 2.11 are rapresented the front and rear side of the target [23].

Rear surface acceleration: a very intense current of high energy hot electrons may be generated at the front side of the target and eventually reach the rear side. There, as the hot electrons cross the rear side boundary and attempt to escape in vacuum, a charge unbalance is generated and consequently also a sheath field E_s,

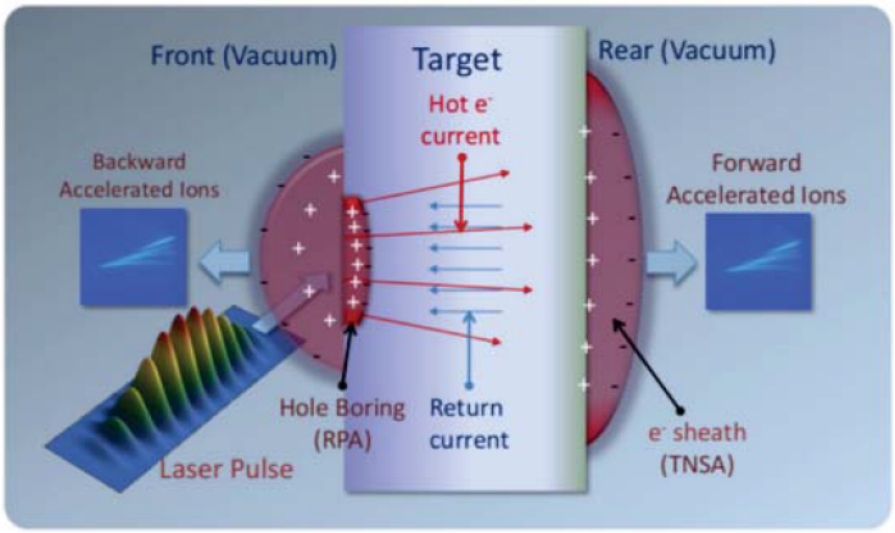

Figure 2.11: Possible acceleration mechanisms in the interaction with a thick solid target: including TNSA at the rear side, hole boring RPA at the front side, and backward acceleration in the plasma blowoff [70]. Also the hot electron flow is shown leading to sheath formation and expansion at the rear side and the associated return current.

normal to the rear surface. Since E_s back-holds electrons with typical temperature T_h , the typical spatial extension, L_s, of the sheath from the target will be related to E_s by [67] :

$$eE_s \sim \frac{T_h}{L_s} \tag{2.12}$$

where e is elementary charge and L_s can be approximated with the Debye length of the hotelectrons λ_{Dh}. This approximation comes directly from the definition of Debye length that is the distance within which a significant charge separation can occur. Considering n_h the density of hot electron [67]:

$$L_s \sim \lambda_{Dh} \sim \left(\frac{T_h}{4\pi e^2 n_h}\right) \tag{2.13}$$

For typical experimental data, electric field values of about $10^{10-11}\ V/cm$ can be calculated. This huge field will backhold most of the escaping electrons, ionize

atoms at the rear surface and start to accelerate ions.
Since the target can contain hydrogen impurities on its surface, protons can be easily accelerated from target rear side. In fact they are faster than other ions thanks to their higher charge-to-mass ratio. This mechanism is commonly known as Target Normal Sheath Acceleration (TNSA)[68] in which the accelerated protons come from the rear surface of the target and the accelerating field is due to the expansion of heated electrons around the target[69]. TNSA has become the reference framework to interpret observations of multi-MeV protons from the target rear side.

Front surface acceleration: starting from the first measurements of proton acceleration in the forward direction, the possibility of a contribution originating at the front surface of the target was also observed and therefore investigated [70][71]. The main idea is that the intense radiation pressure of the laser pulse pushes an overdense target inwards, which causes a sharp growth in density profile and changes the shape of its surface. This process is known as hole boring mechanism, which is a part of the Radiation Pressure Acceleration (RPA) scheme.
In this acceleration mechanism, the approximate relation for the plasma surface velocity v_{hb} is obtained from balancing electromagnetic and mass momentum flows:

$$I_L/c \sim n_i(m_i v_{hb})v_{hb} \tag{2.14}$$

with n_i the ion density. This corresponds to energy per nucleon of

$$E_i = \frac{1}{2}m_p v_{hp}^2 \sim I_L/(An_i c) \tag{2.15}$$

As one can see, the scaling law of the ions energy with respect to the laser intensity is now I_L, more favorable than the $I_L^{1/2}$, typical of the TNSA regime. This aspect suggests RPA effects will become more important for higher laser intensities.

2.4.1 Target Normal Sheath Acceleration - TNSA

Nowadays, the dominant mechanism for ion acceleration intensity up to 10^{20} W/cm^2 from thin foils, is represented by the TNSA.
The regime was firstly described in [68] in 2001 and it has been widely accepted as a possible mechanism for acceleration of ions to multi-MeV energies. The TNSA process is a consequence of the large charge separation generated by hot electrons reaching the rear side of the target.
In figure 2.12 is shown a scheme of the TNSA where ions from the rear side of the target are accelerated by the quasi-static electric field generated due to the charge separation.
A cloud of relativistic electrons is formed, extending out of the target for several Debye lengths, and giving rise to an extremely intense electric field,mostly directed along the normal to the surface.
A consequent distinctive feature is that ions are accelerated perpendicularly to the surface, with high beam collimation. The electric field generated at the rear surface depends on parameters of the electron distribution (temperature, number, divergence) as well as of the surface (mostly its density profile).
The acceleration is most effective on protons, which can be present either in the form of surface contaminants or among the constituents of the solid target as in plastic targets.

The heaviest ion populations provide a positive charge with much more inertia, thus creating the charge separation which generates the accelerating field.
Part of the heavy population can be also effectively accelerated, on a longer time scale, if the proton number is not high enough to balance the charge of the escaping hot electrons, and especially if impurity protons are removed before the interaction, for example by pre-heating the target [72].
The energy spectrum of the protons is typically broadband, up to cut-off energy. A broad angular distribution is also observed, being dependent on particle energy.
Several theoretical models have been proposed in order to describe the TNSA regime, but the most efficient in predicting the energy cut-off and that gives also a good interpretation of the acceleration mechanism is the one proposed by Passoni

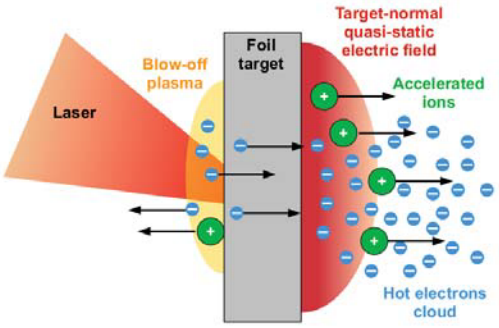

Figure 2.12: Schematic illustration of the TNSA where ions from the rear side of the target are accelerated by the quasi-static electric field generated due to the charge separation.

in [73].

Despite of the strong assumption, this model successfully describes the scaling law of the proton acceleration in TNSA regime, compatible with the experimental results that show a linear dependence of $E_{cut-off}$ with $I^{1/2}$.

Simultaneously to the theoretical studies, several experiments have been performed in order to investigate the properties of the TNSA ion beams.

Many experiments have reported spectral observations for a wide range of laser and target parameters. A number of experimental studies have been also devoted to the investigation of the angular characteristics of the accelerated beams, closely dependent on the electron sheath spatial distribution, and consequently on the target properties (resistivity, surface roughness, etc) affecting the electron propagation[74][75][76].

Together with the energy spectrum behavior, the maximum ion energy, E_{max}, has been, probably, the most characterizing parameter of such experiments.

Due to the importance of the laser irradiance, in literature has became common to report the maximum proton energy E_{max} as a function of the main laser and target parameters. In figure 2.13 is shown a collection of experimental data for E_{max} with respect to the laser intensity together with the two trend lines corresponding to a $I^{1/2}$ and I dependences.

It is also interesting to study the proton-beam maximum energy and the energy-

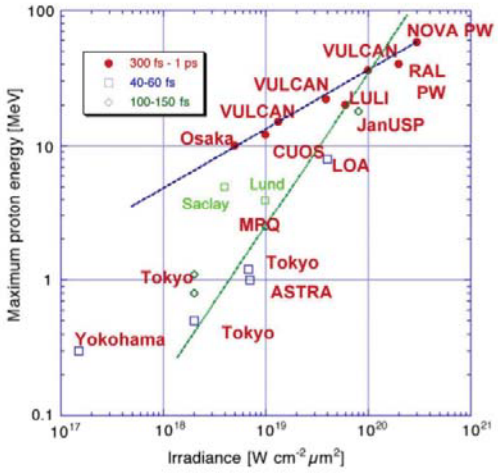

Figure 2.13: Maximum proton energy from laser irradiated solid targets as a function of the laser irradiance and for three ranges of pulse durations, and with additional data (labels Lund and Saclay) reporting later experiments up to 2008. Two trend lines are overlaid, the shallower one corresponding to a $I^{1/2}$ dependence, and the steeper one to a scaling proportional to I.

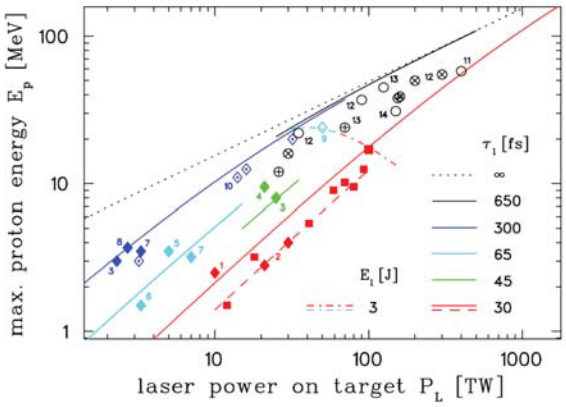

Figure 2.14: Data of experimental scaling of proton energy cut-off with laser power and pulse duration. Squares represent experimental results obtained with 150 TW Draco laser at FZD (Dresden). Other points are data from other laboratories, for references and details see [76].

conversion efficiency varying one parameter at a time, either laser intensity (I), laser en- ergy (E), laser pulse duration (τ_{laser}) or target thickness (d), in order to obtain useful scaling laws [75],[76],[77].
In figure 2.14 are shown the data results of some experiments of E_{max} considering different pulse duration.
In the research program of ELI-beam line commissioning[78], the laser-driven ion beams will be produced through the laser-matter interaction, in the TNSA regime. Indeed, it is expected that the laser-driven ion beams, which will be produced by the interaction of a PW-class laser with solid target, will have similar characteristics of the ion beams accelerated in several experiments investigating the TNSA properties,[74],[75],[76]. In table 2.3 are listed, some estimated parameters of the laser-driven ion beams which will be produced at ELIMAIA beam line.

Table 2.3: Estimated parameters of the laser-driven ion beams expected at ELIMAIA beam line for enabling experiments.

Energy range	3−60 MeV/u
Ion No./laser shot	$< 10^9$(@ 60 MeV/u)
Bunch duration	1−10 ns
Energy spread	± 5%
Source Size	0.1−10 mm
Repetition rate	0.01−1 Hz

2.4.2 Radiation Pressure Acceleration

Electromagnetic (EM) waves carry momentum, which may be delivered to a non-transparent (either absorbing or reflecting) medium. This is the origin of radiation pressure regim whose expression for a plane, monochromatic EM wave of intensity I and frequency ω normally incident on the plane surface of a medium at rest,is given by:

$$P_{rad} = (1 + R - T)\frac{I}{c} = (2R + A)\frac{I}{c} \tag{2.16}$$

where R, T and A are respectively the reflection, transmission and absorption coefficients [79]. Indeed, the EM can release momentum to the target through three different mechanisms: reflection, transmission and absorption.
Clearly the radiation pressure is connected to the ponderomotive force which, as described in section 2.4, provokes hot electrons emission at the surface of the overdense plasma, producing the back-holding electrostatic field that allows the ion acceleration. The effect of radiation pressure on particle acceleration depends on the target thickness.
It is possible to distinguish two different regimes: *Hole Boring regime* and *Light Sale regime*, [68].

Hole Boring regime The*Hole Boring* (HB), occurs when the intense radiation pressure of the laser pulse, pushes the surface of an overdense plasma inward, steepening the density profile. For a realistic laser beam of finite width, the radiation pressure action drives a parabolic deformation of the plasma surface allowing the laser pulse to penetrate deeply into the target, [80].
It is associated with ion acceleration at the front side of the target.
It has been observed that in the instantaneous frame, when the surface is at rest, incoming ions are bouncing back at the surface.
The fastest ions bounced back from the surface in the moving frame, result in a maximum energy per nucleon of:

$$E_{max} = 2m_p c^2 \frac{\Pi^2}{1 + 2\Pi^{1/2}} \tag{2.17}$$

where Π is

$$\Pi = \frac{Z n_c m_e a_0^2}{A n_e m_p} \tag{2.18}$$

Equation 2.17 indicates that with the actual laser intensities high energies may be obtained via HB acceleration if the density can be reduced to be slightly above n_c, which is possible if a gas jet target and a long wavelength laser,i.e., CO_2, is used. Experimental evidence of HB acceleration have been reported in literature [81],[82], [83].

Light Sale regime When a target is thin enough that all the ions are accelerated before the end of the laser pulse, a complete hole boring process occurs. In such a case, the laser pulse is able to further accelerate ions to higher energies since the ions are not screened by a background plasma anymore [84].
This regime of RPA has been named *Light Sale* and it refers to a thin object of finite inertia, having large surface and low mass, so that it can receive a significant boost from radiation pressure. Analytical dissertation of the regime is reported in [85].

Chapter 3

Detector for relative and absolute dosimetry in the ELIMED beam line

The ELIMED beam line, as said in chapter 2, is the beam transport and dosimetric section of the ELIMAIA beam line of ELI-Beamlines facility (in Prague). It has been designed with the aim of providing a user facility where accurate dosimetric measurements and radiobiology experiments can be performed, in order to demonstrate the possibility to use laser-driven ion beams for therapeutic purposes.
Provided that the transport elements, designed and realized at INFN-LNS, will allow to obtain beams selected in energy and with low angular divergence, the beam temporal structure is still very different from the one characterizing conventionally accelerated beams.
Indeed, high intensity pulsed beams will reach the irradiation point, traversing all the dosimetric devices with dose rates per pulse several order of magnitudes higher (i.e. up 10^8-10^{10} Gy/s) as respect the case of conventionally accelerated particles.
In order to perform accurate dosimetry of laser-driven ion beams in this extreme environment in the perspective of multidisciplinary applications at ELIMAIA, alternative approaches have been adopted and new detectors have been developed.
The dosimetric system is composed by detectors for relative and the absolute dose measurements.
The key elements of this section, as described in chapter 2, are a Faraday Cup used

to the absolute dose measurements, a multi-gap transmission ionization chamber (IC), used for relative dosimetry and a secondary emission monitor (SEM). A sample irradiation system (SIS) will be installed at the end of the in-air section and it will be used to place the samples to irradiate.
In the following sections, a detailed description of each detector composing the dosimetric system will be presented.

3.1 Absolute dosimetry

3.1.1 Faraday Cup

In order to overcome ion recombination effects that may occur using ionization chambers at high dose-rate per pulse, a Faraday Cup (FC) for absolute dosimetry has been designed and realized for the ELIMED beam line, (figure 3.1).
It is an absolute dosimeter with the aim to count and measure the collected charge due to beam impinging the detector and, according to its working principle, it is independent on the dose rate. It is currently the best solution to measure the dose delivered by laser-driven proton beams. The realized FC has a peculiar geometry and it has been inspired to similar detectors already developed for ion beam dosimetry, but aiming to optimize the charge collection efficiency, [86], [87].
It is 400 mm long, with an internal radius of 20 mm and it is made of aluminum. The main components are:

- The entrance Window: a 50 μm kapton window. An entrance window is necessary in order to maintain the vacuum inside it has to be thinner enough to avoid beam perturbation;
- The guard ring or suppressor: a 180 mm steel suppressor. An electric field can be applied to collect the secondary electrons generated in the cup itself and repel the ones produced in the entrance window;
- Cup: a 50 mm thick aluminum cup. The thickness has been designed in

Figure 3.1: The Faraday cup with its line support opened.

order to stop both the primary particles and the secondary ones eventually produced in the interaction with the cup itself.
Since the ionization of the residual air could affect the FC measurements, a vacuum of about 10^{-5} mbar is required as working condition.

The primary beam, passing through the thin vacuum window, is collected in the FC cup. The total collected charge is acquired by an electrometer. In the absolute dose measurement using a FC, a precise measurements of the total charge carried by the beam, of the proton beam energy spectrum and of the effective beam area are needed to extract the absorbed dose to water (Dw) for a proton beam, according to the expression:

$$D_w = \frac{1}{A_{eff}} \frac{\int_{E_min}^{E_max} S(E)N(E)dE}{\int_{E_min}^{E_max} N(E)dE} \frac{Q}{e} 1.6020 \times 10^{-10} \quad [Gy] \tag{3.1}$$

where A $[cm^2]$ is the *beam effective area*, $S_W(E)$ the *mass stopping power* in water $[MeVcm^2g^{-1}]$ at a given energy E, Q is the *measured charge* and e is the *elementary charge*.
The beam effective area depends on the dose distribution over the beam profile

and can be expressed as:

$$A_{eff} = \int_0^{2\pi} \int_0^R D(r) r dr d\theta \tag{3.2}$$

where $D(r)$ is the *normalized dose* at the point of the radius r, and that can be approximated as:

$$A_{eff} = 2\pi \sum_0^R r_i P(r_i) dr_i \tag{3.3}$$

where r_i is the scan step, $P(r_i)$ is the *normalized dose* or *fluence distribution* associated to the beam profile and R is the radius for $P(R) = 0$, [88].

An issue related to the total charge measurements is represented by the emission of secondary electrons produced by the interaction of the protons with both the entrance foil and the cup itself. The emitted secondary electrons may be either collected or leave the cup, affecting the collected charge measurements.

The secondary electrons produced in the entrance window former may lead to a total charge underestimation while those produced within the cup material, if produced with sufficient energy, may leave the collecting cup and cause a charge overestimation.

Typical FC detectors have cylindrically symmetric components and employ coaxial electrostatic fields to recapture the ejected electrons.

In order to improve the measurement of the total charge, it is possible to shape the internal electrode in a similar way as presented by Thomas et al. in [89] with a peculiar *beveled cylinder* design, fig. 3.2. The implementation of this additional element breaks the electrostatic coaxial symmetry of the field, provided solely by the external electrode, introducing a relevant transverse electric field component, which can further increase the recapturing efficiency for secondary electrons.

A feasibility study has been carried out, aiming to establish the best electric field configuration for secondary electron suppression. It has been performed using the COMSOL [90] FEM (Finite Element Method) software, SIMION FEA (Finite Element Analyze) software and the Monte Carlo toolkit Geant4 [91].

A Monte Carlo simulation has been performed to obtain the energy spectrum of

Figure 3.2: Beveled cylinder electrode.

the secondary electrons produced in the interaction of the beam with the kapton window and the cup in order to be used as input for the SIMION simulations.
The results obtained considering as input a 62 MeV proton beam with Monte Carlo simulations are shown in figure 3.3. The secondary electron are produced by the

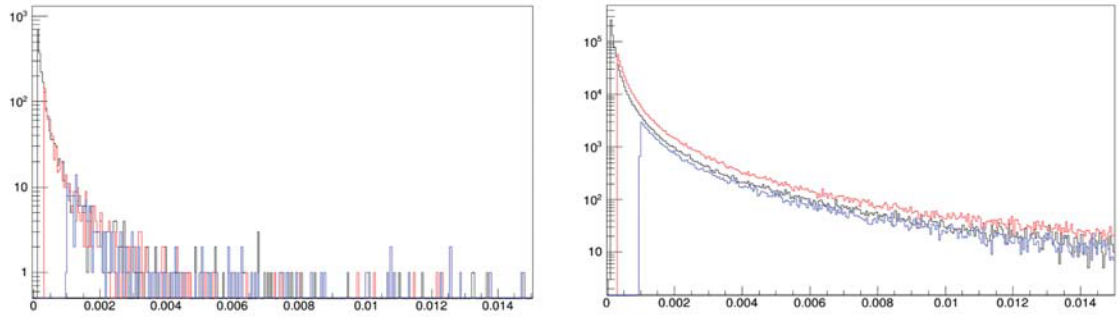

Figure 3.3: On the left simulation of the energy spectrum (MeV) of the secondary electrons produced in the beam-kapton and on the right the beam-cup interaction obtained varying energy threshold for secondary electron production: 990 eV (blue) , 300 eV (red) and 100 eV (black).

interaction of the primary beam, respectively with the entrance window and with the cup. The simulations with SIMION software have been performed, in order to study how the applied field determines the secondary electron deflection, improving the collection efficiency for the electrons produced in the cup and rejecting the ones produced in the entrance window .
In particulary, SIMION simulations have been performed to study the electric field when the additional internal electrode is used to deflect the secondary electrons,

figure 3.4, [92].

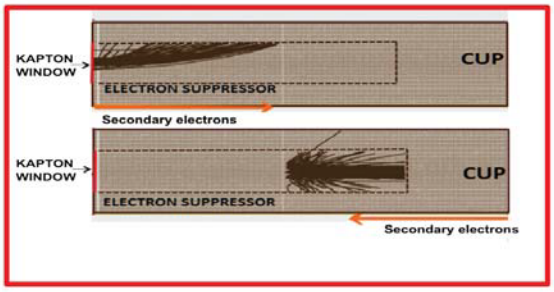

Figure 3.4: An example of secondary electrons generated by the beam-kapton and the back-scattered interaction repulsed by the asymmetric electric field, simulated with SIMION.

The cylindrical symmetry of the electric field provided by the external electrode is broken due to the presence of the internal one. The resulting effect is a strongly asymmetric electric field, characterized by a significant transversal component able to maximize the deflection of the secondary electrons. In figure 3.5 are represented the X-Y component of electric field along the beam axis.

In order to define the final shape and the materials of the collection cup, a study

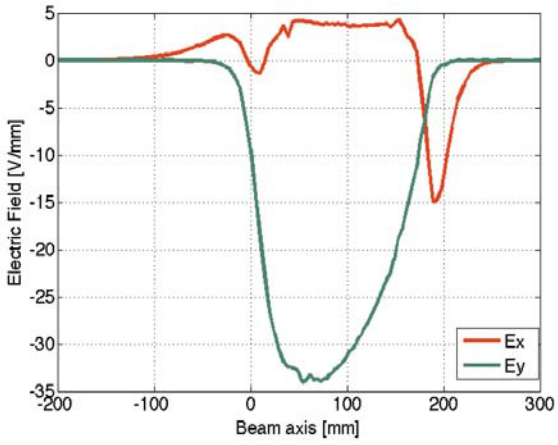

Figure 3.5: Electric field components Ex (red), Ey (green). The electric field is expressed in V/m and the X axis in mm.

has been carried out with Geant4 Monte Carlo simulations.
Three different materials have been considered: aluminum, graphite and copper. The results have shown that a good compromise between secondary electron production (to minimize in order to have lower uncertainties in charge collection) and the material handling from the mechanical point of view is represented by the aluminum. Hence, this material has been choosen for the realization of the cup.
Similar investigations have been done for the designing the shape and size of the cup, chosing a final thickness of 3 cm.
According to the results obtained with the feasibility study performed with the mentioned analytical and Monte Carlo codes, the final configuration of the FC has been obtained and it has been designed as shown in figure 3.6. In this thesis, the

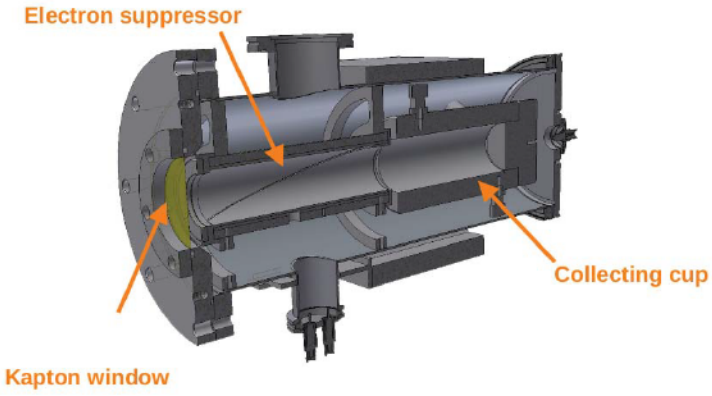

Figure 3.6: Layout of the FC developed at LNS.

results related to the characterization of the FC using the conventional cylindrical electrode will be shown and discussed in the next chapter.

3.2 Relative dosimetry

3.2.1 Radiochromic films

Radiochromic films (RCFs) are dose-rate independent relative dosimeters that allow to measure the delivered dose, giving 2D dose distributions, once calibrated

against an absolute dosimeter. They are easy to handle and the physical information contained in the films is not lost during the reading process, allowing post-processing for additional data analysis.
RCFs consist of a single or double layer of radiation-sensitive organic microcrystal monomers, on a thin polyester base with a transparent coating. Due to polymerization of monomers by ionizing radiation, the active layer color becomes darker and, quantitatively, it is measured through the optical density of the film (OD).
The OD is defined as the luminous intensity reduction that a beam of light, preferably monochromatic, undergoes when it passes through the film and it is given by:

$$OD = log\left(\frac{I_0}{I}\right) \tag{3.4}$$

where I_0 i is the light intensity before passing through the film and I is the light intensity after the film.
RCFs are not perfectly transparent due to an intrinsic background, therefore it is tipically defined the netOD as:

$$netOD = OD_{RFC_{irradiated}} - OD_{background} \tag{3.5}$$

Different models of RCFs are on the market, and they have to be chosen according to the sensitivity, dose and energy range.

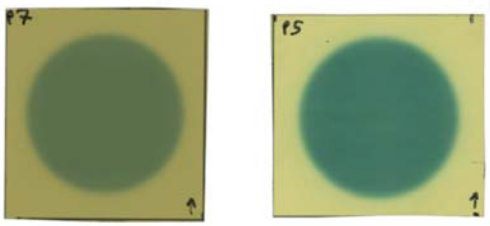

Figure 3.7: Examples of EBT3 and HD-V2 films irradiated, respectively, with 3 Gy and 400 Gy of proton beam at $60MeV$.

EBT3 and HD-V2 models can cover all the possible requirements related to laser-driven beams measurements (Figure 3.7).
HD-V2 films are made of three different layers both for thickness and for atomic percentage composition (figure 3.8). The basis is a layer of polyester of 97 μm of thickness on which is deposited an active layer of 6.5 μm and a protective gelatin surface layer of 0.75 μm. Thus, they basically are characterized (at least from one side) by a negligible dead layer (that may be useful for low energy measurements) but they have a lower sensitivity ($10 - 1000\ Gy$).
EBT3 are symmetric and consist of three layers: the central active layer of 28 μm covered by two identical polyester layers of 125 μm of thickness 3.7. They are more sensitive respect to HD-V2 (0.1 - 10 Gy), so that they have a good response also for low dose irradiations (figure 3.9).

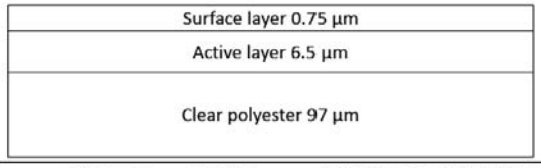

Layer	Thickness [µm]	Density [g/cm³]	Atomic composition percentage			
			C	H	O	N
Clear polyester	97	1.35	45.45	36.36	18.19	
Active layer	6.5	1.08	29.14	56.80	7.12	6.94
Surface layer	0.75	1.2	24.36	55.22	12.82	7.6

Figure 3.8: Structure, relative dimensions of layers and nominal atomic abundances of GafChromic films HD-V2.

A particular type of RCFs is the "unlaminated" version of the EBT3, which could represent a good compromise between the two different products, because characterized by the same sensitivity, as for EBT3, and a negligible dead layer, as HD-V2.
Due to the mentioned specifications and to their high spatial resolution (typically dependent on the scanner resolution, which is of the order of hundreds of μm) the RFCs have been used to perform transversal/longitudinal depth dose distributions (figure 3.10) and fluence measurements.

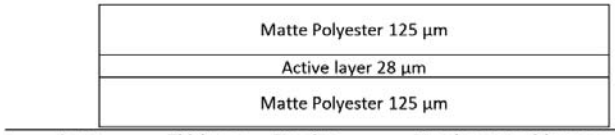

Layer	Thickness [µm]	Density [g/cm³]	Atomic composition percentage				
			C	H	O	Li	Al
Matte polyester	125	1.35	45.30	36.40	18.10	0.10	0.10
Active layer	28	1.2	26.60	55.80	10.70	5.30	1.60

Figure 3.9: Structure, relative dimensions of layers and nominal atomic abundances of GafChromic films EBT3.

RCFs can be also used in stack configuration, providing a measurement of the energy spectrum of an incident radiation, which is one of the information needed for obtaining the absolute dose with the FC, according to the equation 5.6.
In stack configuration, ions with lower energy stop in the first layers while the ones with higher energy penetrate the deeper layers. Knowing the thickness, composition and density of each RCF, it is possible to retrieve the energy spectra through an iterative procedure based on deconvolution methods.

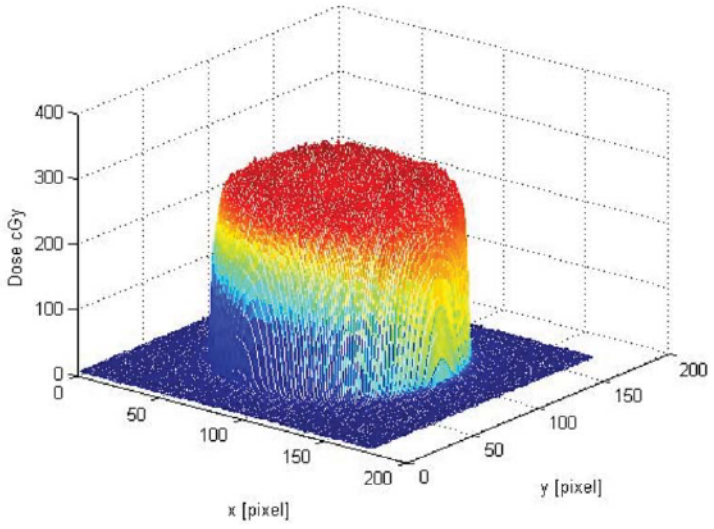

Figure 3.10: 2D image of a profile obtained with a RFC irradiated with 62 MeV proton beams.

An example of how to use this method to extract the energy spectrum of proton beams is described as follows: using a modulator wheels to obtain polychromatic beams, it is possible to spread the beam and achieve several single peaks at different energies, whose convolution gives rise to the depth dose distribution of figure 3.11 well know as SOBP.

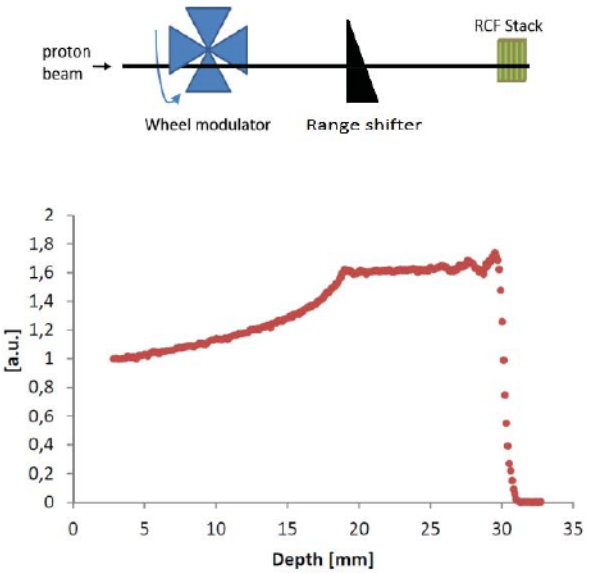

Figure 3.11: On the top: typical configuration composed by a wheel modulator and to obtain SOBPs. On bottom: depth dose distribution obtained with a modulator wheel.

In Figure 3.12, a stack of HD-V2 films irradiated with modulated proton beams is shown. Starting from the delivered dose D in the n-*th* RCF and using the equation valid for monochromatic beams relating the dose to the fluence f:

$$D = (f \cdot de/dx)/\rho \tag{3.6}$$

where dE/dx is the stopping power and ρ the density of active layer, it is possible to extract the absolute number of protons at that energy and, at the end of the iterative procedure, obtain the energy spectrum.
For the ELIMED beam line a removable support for the RCFs has been designed, in order to perform gaf irradiations in stack configuration with high level of accuracy

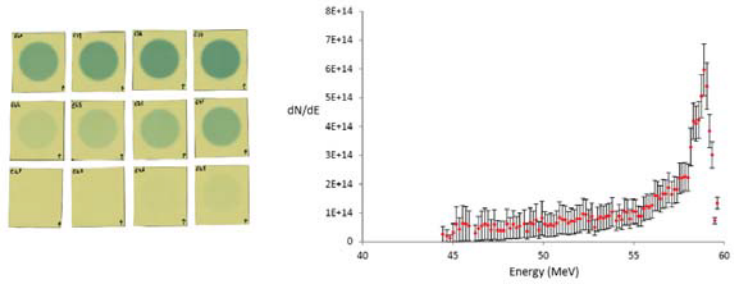

Figure 3.12: RCFs in stack configuration acquired with a flatbed scanner (on the left); example of energy spectrum retrieved with the iterative procedure (on the right).

and reproducibility. It is a PMMA support,fig3.13, screwed to the flange of the FC by two bolts 3.12. Two front screws hold up the single RCF or the stack, depending on the kind of measurement to be carried out.

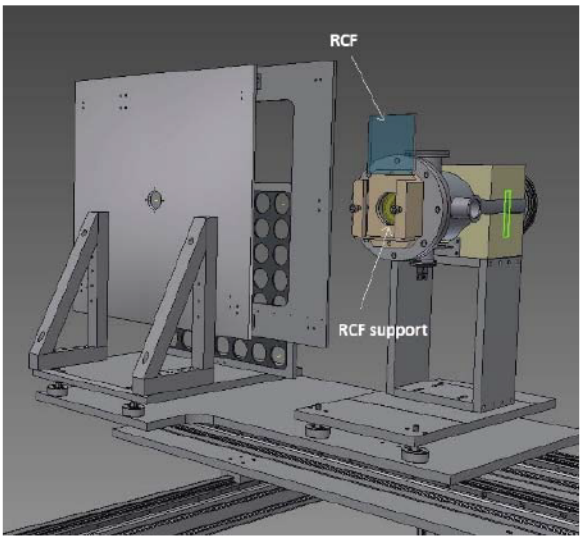

Figure 3.13: RCF PMMA support.

3.2.2 Ionization Chamber

A multi-gap Ionization Chamber (IC), for relative dosimetry, has been realized for the ELIMED beam line. It is a novel in-transmission ionization chamber de-

signed to on-line measure the dose delivered per pulse, without perturbing the beam transport downstream at the irradiation point, figure 3.14. It is an in-transmission double-gap chamber, filled of air, which will be cross-calibrated with the FC absolute dosimeter.

The presence of a second gap close to the first one allows to correct for the ion recombination effects caused by the very high dose rate per pulse characterizing laser-driven ion beams.

In the sensitive volume of an ionization chamber, positive and negative ions are created when ionizing radiation passing through the gas and the charge at the electrodes can be measured, as it has been described in chapter 1.

Figure 3.14: Picture of multi-gap ionization chamber.

In principle, the charge generated in the gap of the chamber, Q', should be the same that is collected at the electrodes, if ones ideally consider 100% of collection efficiency. In real conditions, however, the collected charge, Q, results to be lower than the produced charge: this occurs because of recombination effects inside the

gap, as discussed in chapeter 1. In order to estimate the magnitude of the charge efficiency between Q' and Q, it is necessary know the collection efficiency.
By increasing the voltage applied to the electrodes, it is possible to observe an increase of the collected charge: initially almost linearly with the applied voltage, up to asymptotically approaching to the saturation charge as shown in figure 3.15.
As explained in chapter 1, general recombination occurs when ions produced in

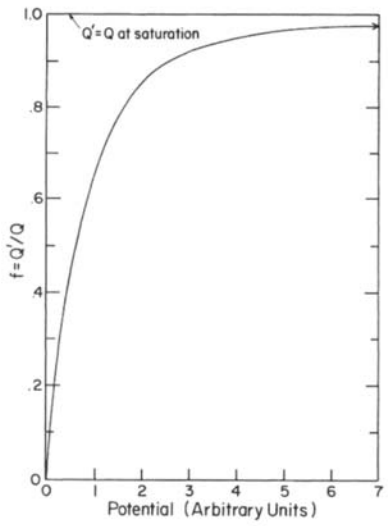

Figure 3.15: The saturation curve for a multi-gap IC.

different tracks recombine each other on their way to the collecting electrodes. The amount of this type of recombination depends on how many ions are created per unit volume and per unit time, consequently, general recombination is dose-rate dependent and, for laser-driven beams, it is expected to be relevant.
For high flux beams the recombination phenomenon become very significant and therefore the total charge collection is inefficient unless a very high voltage between the electrodes is applied.
Due to physical limits, mainly due to a breakdown threshold for the applied voltage, it is not possible to arbitrarily increase the electric field in the ionization chamber.
A solution is provided by a detector with at least two gaps, operated as two inde-

pendent ionization chambers, where the recombination effects, and consequently the efficiency, are different.

The device is a planar structure, basically composed of two adjacent ionization chambers, with a gap (space between the electrodes) respectly of $5mm$ and 10 mm and independently supplied (different voltage values according to the specific gap). The anode is constituted by a thin layer of $5\mu m$ of copper and 2 μm of

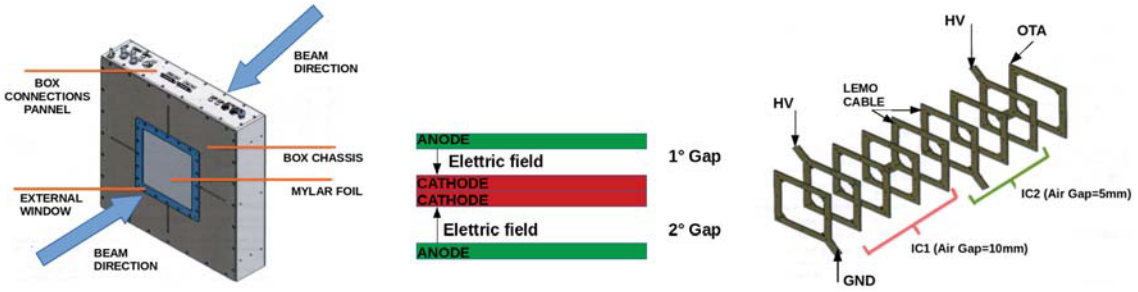

Figure 3.16: An overview of multi-gap IC, the scheme of electrode and the sensors package composed of frames used in stack, in order to separate the cathodes and the anodes and to support the multi-gap IC at the center of the box. In the sensors package (on the right) IC_1 is indicated by the red bracket and IC_2 by the green bracket.

Nichel deposited on a 25 μm layer of kapton, while the cathode is constituted by a 12 μm layer of aluminized mylar. Both of them are fixed by a frame of epoxy glass, (figure3.16).

The two chambers have been designed with a different gap, which is typically filled by air and arranged with a precise order to allow a different electric field between chambers.

The two chambers are placed in the center of an aluminum box of 420x420x100 mm^3 of size (figure3.16), and an external window of aluminized mylar is present in front. The modularity of the device will give the possibility to eventually add, in future, additional gaps for redundancy.

The working principle of this detector is based on the idea that the recombination effects can be corrected once the collection efficiency f in specific conditions is known.

For specific experimental conditions, ionization chamber response can be related

not only to absorbed dose, but also to the beam flux crossing the chamber. When the change in incident particle energy can be neglected, the average charge produced per particle for a beam energy E_p traversing the gas Q=$N_p(E_p)$, is given by:

$$\frac{Q}{N_p(E_p)} = \frac{(S(E_p)/\rho)_g \rho x}{W(E_p)/e} \tag{3.7}$$

Considering the equation 3.7 it is possible to obtain equations 3.8, i which show that the current measured by the ionization chamber is proportional to the beam current:

$$Q = \frac{e(N_p)S\rho_g d}{W} \tag{3.8}$$

$$I_{IC} = \frac{Q}{\Delta t} = \frac{eS\rho_g dN_p}{W\Delta t} \tag{3.9}$$

$$I_{beam} = \frac{eN_p}{\Delta t} \tag{3.10}$$

$$I_{IC} = I_{beam}\frac{S\rho_p d}{W} \tag{3.11}$$

where

e is the electron charge,

$N_p/\Delta t$ is the flux beam (part/s),

S is the stopping power (MeVcm^2 /g),

ρ_g is the density of the gas (g/cm^3),

d is the distance between the electrodes (cm),

W is the average energy required to create an ion pair for the gas (MeV/ion pair),

I_{IC} is the current measured by the ionization chamber (A),

$I_{beam}$is the beam current (A). The linear proportionality between the two different currents (I_{IC} and I_{beam}) current only occurs if the effect of charge recombination is negligible. In fact, it is known from the recombination models that the collection efficiency decreases with the increase of the ionization density in the gas.

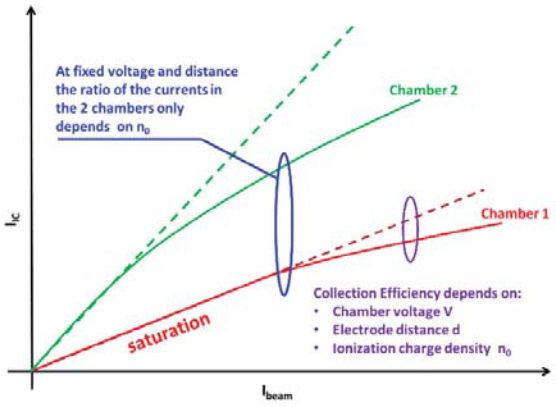

Figure 3.17: Relation between the beam current I_{beam} and the current measured by the ionization chamber I_{IC} for two chambers with different gas gaps.

At high beam currents the relationship between I_{IC} and I_{beam} is not more linear, as shown in figure 3.17 for two chambers, where chamber 2 has a larger gap than chamber 1.

This effect is explained by the theory of Boag-Wilson used to determine the collection efficiency for an ionization chamber filled with electronegative gas,radiated from a pulsed beam with pulses of short duration and slow enough repetition rate with respect to time of charge collection (chapter 1), [93].

This model,predicts the charge recombination and explain as collection efficiency can be determined knowing the chamber voltage V,the electrode distance d and the ionization charge density n_0: at a fixed voltage and distance between the electrodes, the ratio of the currents in the different gaps only depend on the ionization charge density n_0, which is the parameter of interest to determine. Applying the Boag-Wilson theory, since the two ionization chambers have independent electrodes with different thicknesses, d_1, d_2, separated by gas and operated at different voltages, if crossed by the same beam they will be characterized by two two different collection efficiencies.

The ratio of the efficiencies, f_2, f_1, of two IC is directly related to the ratio of the

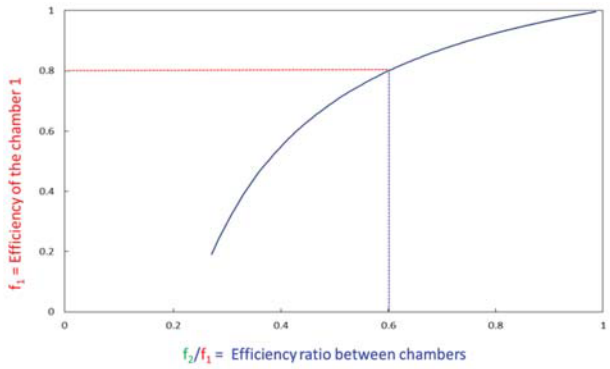

Figure 3.18: Calibration curve which relates the efficiency of the chamber 1 to the ratio of efficiency of the two chambers.

currents measured(I_{IC_2}, I_{IC_1}) in the two chambers by:

$$\frac{f_2}{f_1} = \frac{I_{IC_2}}{I_{IC_1}} \frac{d_1}{d_2} \tag{3.12}$$

This quantity can be easily determined and will be unique for a given common ionization density, figure 3.17.
If the chamber 1 is chosen as the reference chamber, a curve relating the efficiency f_1 to the measured ratio f_2/f_1, would allow to determine f_1 and correct for it. This curve is called *Calibration curve* and it is represented in figure 3.18.
Once the calibration curve is included in a data acquisition software, an on-line correction for the chamber response can be provided shot-by-shot, tacking into account the intensity variations per bunch.

3.2.3 Secondary Electron Monitor

The SEM (Secondary Electron Monitor) detector [94],[95] is made of a 130 mm diameter Tantalum foil, 12.5 μm thick, provided with an electrically insulated circular frame of PMMA. It is represented in figure3.19. Its working principle is based on the secondary electron emission (SEE): when a charged particle passes through an interface of a solid material, very low energy electrons can be emitted from

the surface. The main parameter describing the SEE is the Secondary Emission Yield (SEY), which is the average number of electrons emitted when an incident projectile passes through a surface and it is proportional to the energy loss of the particle in the surface layer.
The secondary emission yield theory is based on three steps: creation, diffusion and emission. The creation is the production of the electron-ion pairs by a fast projectile in the bulk of the material and the dominant process is the ionization. A least energy to excite the electrons from the conduction band is required.
If the projectile is an ion containing electrons in its shells, these ones can be stripped off and possibly induce ionizations.
When the low energy electrons produced by ionizations propagate through the solid, they strongly interact with other electrons and rapidly lose their energy.
In the metals, the excited electrons with higher velocities have to propagate by diffusion and by cascade multiplication create many low energy secondary electrons. The low energy secondary electrons are described by an exponential decay law.
At very low primary energies, the secondary electrons escape efficiently, and due to the small primary energy only a few secondary electrons are created. Since the number of secondary electrons generated increases with primary energy, the observed yield also rises with primary energy. At very high primary energies the exponential nature of the escape process causes the decrease in the number of secondary electrons that escape to be more rapid than the increase in generation of low energy secondary electrons. Consequently, the observed yield decreases with primary energy.
Before a secondary electron is emitted from a metallic surface, it is necessary overcome the surface barrier potential. The emission process can be regarded as a refraction phenomenon, as only the momentum vector normal to the surface is lowered due to the barrier crossing and transverse momentum is conserved.
The SEM is basically a beam current monitor, but it can be used as a device to measure the dose, once cross-calibrated against a reference dosimeter; indeed, a relationship between SEM current and the absorbed dose rate at a specified point in the radiation field can be found.

The SEM detector will be mounted in a vacuum chamber, placed at the end of the in vacuum beam line section and it will be mainly used to monitor the beam flux. It will be provided with an actuator that will allow to remove the detector from the beam axis when it is necessary. In figure3.19 a section of the SEM placed in the vacuum chamber of the beam line is shown.

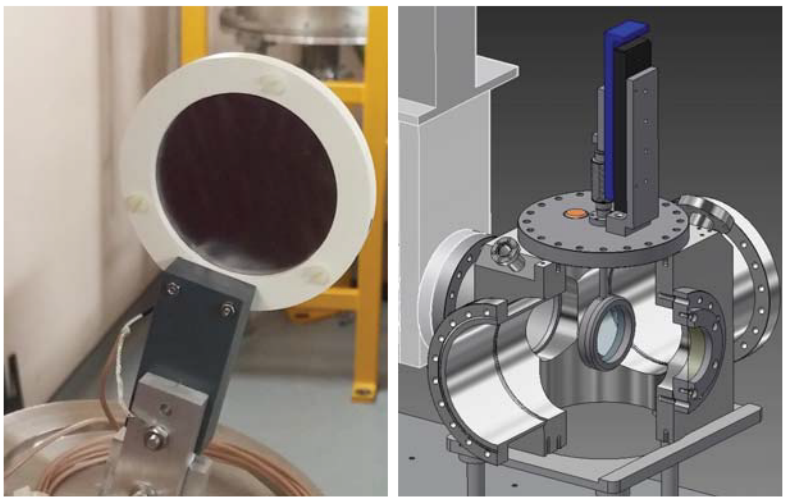

Figure 3.19: A picture of the SEM (left) and a drawing section of SEM in the vacuum chamber of the beam line (right).

Chapter 4

Characterization of the ELIMED dosimeters with conventionally accelerated protons at 62 MeV

The radiochromic films (RCFs) and the Faraday cup (FC) described in the previous chapters have been characterized with proton beams provided in conventional accelerator facilities. The absolute and relative dose have been measured at the irradiation point at the CATANA proton therapy facility at LNS-INFN in Catania with clinical proton beams of 62 MeV accelerated by a Superconducting Cyclotron. In this chapter the treatment beam line and all the passive elements used to deliver clinical beams will be described, as well as the procedures to calibrate the relative dosimeter according to IAEA TRS 398 protocol [14]. The results related to the measurement carried out with FC and the RCFs will be discussed at the end.

4.1 Description of the CATANA passive proton beam line

The CATANA (Centro di AdroTerapia ed Applicazioni Nucleari Avanzate) proton beam line is the first Italian hadron-therapy facility, entirely built and installed at INFN-LNS at the end of '90s. It is based on the use of a 62 MeV proton beam

delivered by a superconducting cyclotron. It is used for the therapeutic treatment of some kinds of ocular tumours. Figure 4.1 shows a global view of the CATANA facility. The energy of 62 MeV confines maximal range of proton beam to about

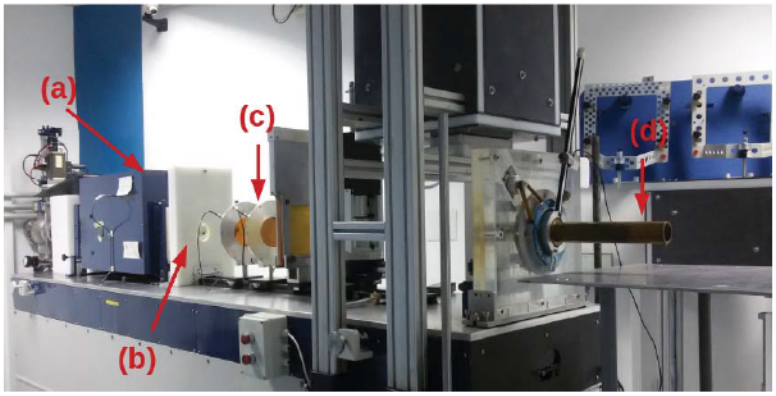

Figure 4.1: View of the CATANA beam line: (a)Box for the location of modulator wheel and range shifter; (b) Intermediate collimator; (c) Monitor chambers; (d) Final collimator

30 mm of eye-tissue, sufficient for the irradiation of intraocular tumours, as uveal melanoma.

The proton beam exits in air through a 50 μm Kapton window placed upstream the in-air final section of beamline at about 3 m from isocenter. Just before the exit window, it is placed the first scattering foil made of 15μm of tantalum. It is used to control the beam current and to provide a first diffusion of the beam. The first element of the beam in air is a second tantalum foil, 25 μm thick, provided with a central brass stopper of 4 mm in diameter.

The double scattering foil system is optimized to obtain a good homogeneity in terms of lateral off-axis dose distribution, minimizing the energy loss.

The stopper has the function of deleting the more pronounced central component of the Gaussian distribution of the protons spread by first scattering foil.

In order to passively degrade the energy of protons and to obtain uniform longitudinal dose distributions, respectively range shifters and range modulators are used. They are placed inside a box, downstream of the scattering system, (figure 4.1), [96], [97]. The modulator is a PMMA wheel with some steps of different thicknesses, figure 4.2, equipped of a motorized system to rotate. It allows

the modulation of the beam energy by giving rise to the spread out Bragg peak (SOBP). A key element of the treatment line is represented by two in-transmission

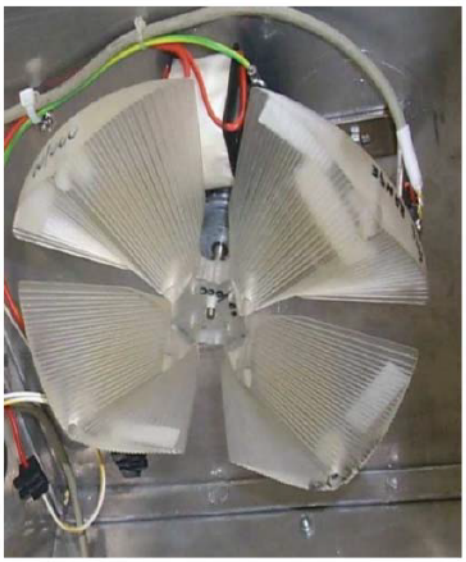

Figure 4.2: An example of modulator

monitor ionization chambers. The aim of the chambers is, once cross-calibrated with a reference detector, to provide the on-line control of the dose delivered to the patient.
They are made up of two Kapton foil thick 25 μm separated by 9 mm of air and internally covered by a layer of 224 copper which makes the conductive walls.
The last element is a collimator located 8.3 cm before the isocenter.
A positioning system consisting of a light field and a laser, is used both for positioning the patient or the dosimeters used during the measurements.

4.2 Preliminary dosimetric characterization of proton beams

The proton beam transported from the cyclotron up to the Catana beam line is quite far to be considered a clinical beam, since it has a Gaussian distribution

approximately 2 mm wide along the plane perpendicular to the direction of the beam. The passive elements described in the previous paragraph are used to change the beam parameters in order to achieve a proper longitudinal and transversal dose distribution, suitable for clinical treatments. To check if the obtained beam is characterized by the required parameters, it is necessary to acquire the spatial dose distributions along the horizontal (X) and vertical (Y) directions. These curves are called transverse beam profiles and are obtained with a detector located in the input channel in the case of a non-modulated beam, or at the center of the spread-out Bragg peak (SOBP) in the case of a modulated beam. Moreover, also longitudinal dose distributions have to be measured to measure the beam range and characterize the energy modulation (for SOBPs).

Beam diagnostics with Gafchromic and semiconductor diode

As said before, a check of the X-Y profiles along the orthogonal direction of the beam is necessary to verify the homogeneity.
In order to determine the X and Y profile at isocenter a Hi-pSi diode detector is used(0.6mm detector diameter).
The diode is equipped with a remotely controlled handling system. It scans the beam in both directions. The data analysis is performed with a LABVIEW software, developed at LNS.
Transversal dose profiles is characterized by the following parameters :

- The radiation field ($W_{50\%}$) is defined as the Full Width at Half Maximum of the dose profile and allows to evaluate the size of the beam.

- The lateral penumbra (PSX - PDX) is defined as the distance between the points corresponding to 80% and 20% of the central value and allows to evaluate the trend of dose drop to the edges. This parameter must be smaller than 1 mm for non-modulated beams and less than 1.5 mm in the case of modulated beams.

- The beam symmetry (symmetry of ionization profiles on a transverse plane

to the beam axis) can be defined as:

$$S_r = \frac{(\mid a - b \mid) \times 200\%}{a + b} \tag{4.1}$$

where a is the area to the left of the central axis and b is the area to the right of the central axis; the areas are bounded by the central axis and the point where one have 50% of the field.

- the trasversal homogeneity is defined as:

$$S_T = (\frac{D(x)}{D(-x)})_{max} \times 100\% \tag{4.2}$$

where D (x) is the dose at point x; x and -x are symmetric points to the beam axis. This symmetry is defined as the maximum ratio, within the largest of the regions between T_{R1} and T_{R2}, multiplied by 100. The parameters T_{R1} and T_{R2} are thus determined:

  - T_{R1} is the central region of width equal to 80% of the field size ($W_50\%$)
  - T_{R2} is inner region twice width from the point of 50%

  Where S_r can be less than or equal to 3% and S_T must be less than or equal to 103%.

- The homogeneity of the beam ($R\%$) is a percentage value that indicates how much the beam is homogeneous in the central region and is calculated using the following formula:

$$R_{\%} = \frac{P_{max} - P_{min}}{P_{max} + P_{min}} \times 100 \tag{4.3}$$

where P_{max} and P_{min} are the maximum and minimum values measured in the region between 95 and 100. This parameter must be less than 2.5%.

In figure 4.3 is shown an example of the experimental lateral dose distribution for the 62-MeV proton beam measured with a final 25-mm diameter circular brass collimator (reference collimator).

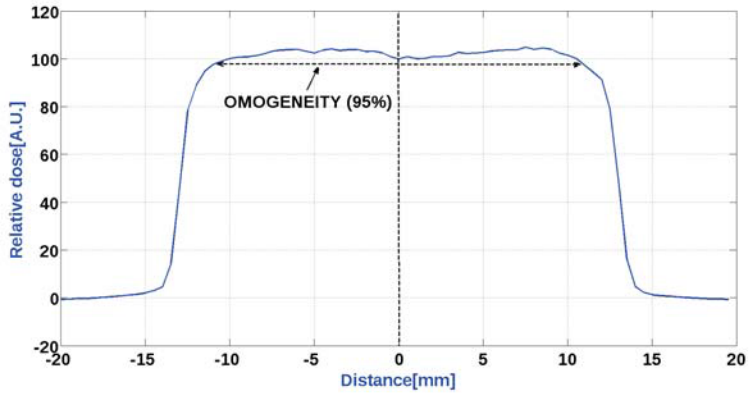

Figure 4.3: Experimental lateral dose distribution for the 62-MeV proton beam measured with a final 25-mm diameter circular brass collimator (reference collimator).

Unmodulated Bragg Peak acquisition

As already mentioned, in order to calibrate the proton beam and deliver the required absolute dose in water at the irradiation point, an Advanced Markus plane-parallel PTW Ion Chamber is used as reference dosimeter, following the IAEA TRS-398 code of practice for absolute dosimetry, [14].

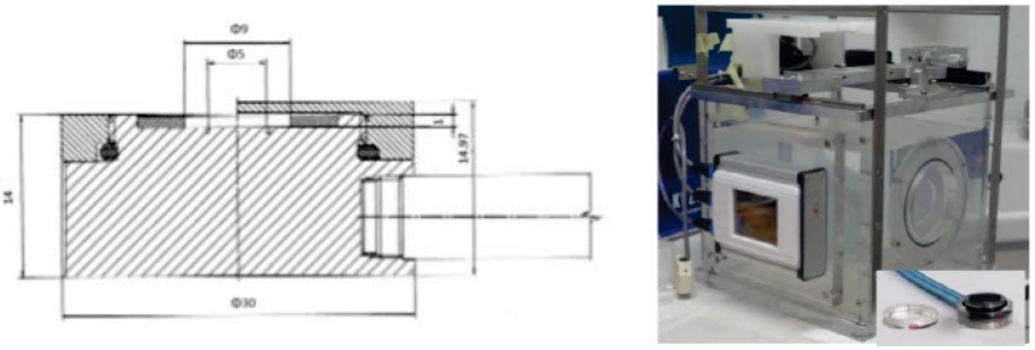

Figure 4.4: Left: a scheme of an Advanced Markus plane-parallel PTW Ion Chamber. Right: a water phantom for the absolute dose measurement in the clinical practice with the Markus chamber and for the depth dose distributions

It is characterized by an electrode spacing of 1 mm and a collection volume of 0.02 cm^3, (figure4.4).

The same chamber is used in the clinical practice, [14], to acquire the depth dose curves in a water phantom, using the reference 25 mm diameter circular collimator. The following parameters are considered for longitudinal dose distributions:

- FWHM:Full Width at Half Maximum of unmodulated Bragg peak.
- Penumbra (80% -20%): this term specifies the distance between points, present in the distal part of the peak, which correspond to 80% and 20% of the maximum dose peak and must be less than 1 mm.
- Penumbra (90% -10%): this term specifies the distance between points, present in the distal part of the peak, which correspond to 90% and 10% of the maximum dose peak and must be less than 1 mm.
- Practical Range: It is defined as the depth at which the absorbed dose becomes the 10% of the maximum and it is measured in the distal part of the Bragg or SOBP.
- Peak/Plateau ratio: it is the ratio between the maximum value recorded at the peak and measured at the entrance.
- Residual Range: usually expressed in g/cm^2 is defined as:

$$R_{res} = R_p - Z \tag{4.4}$$

  where Z is the measurement depth and R_p is the proton practical range.

The acquisition of the depth dose curves (or Bragg peak) give informations about the practical range used to calculate the ratios between the stopping powers, which will be used to determine the dose in water and therefore to perform absolute dosimetry following the IAEA TRS-398 code of practice. Figure 4.5 shows the depth dose distribution obtained with the Markus chamber for unmodulated peak. The Full Width at Half Maximum of the Bragg Peak is 2.8 mm. The 90%-10% and 80%-20% distal fall-offs are 0.8 and 0.6 mm, respectively, and the peak to entrance ratio is 4.7.

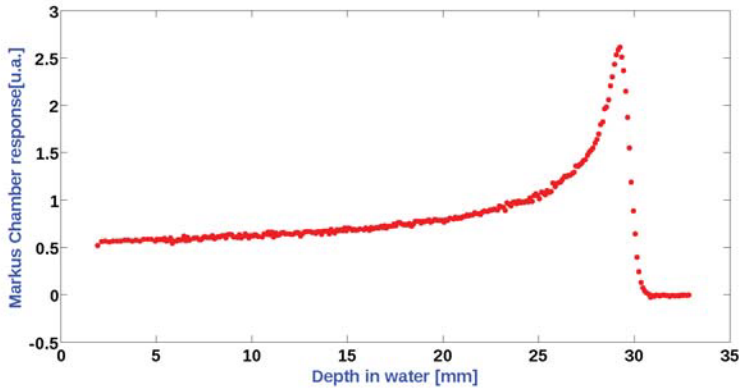

Figure 4.5: An example of Bragg peak for proton beams at 62 MeV acquired with the Advanced Markus chamber in a water phantom

Modulated Bragg peak acquisition

The acquisition of the a modulated Bragg peak is performed by placing a PMMA modulator wheel(see Figure 4.2)previously described, in order to obtained the SOBP, using the reference 25 mm diameter circular collimator. Also in the case

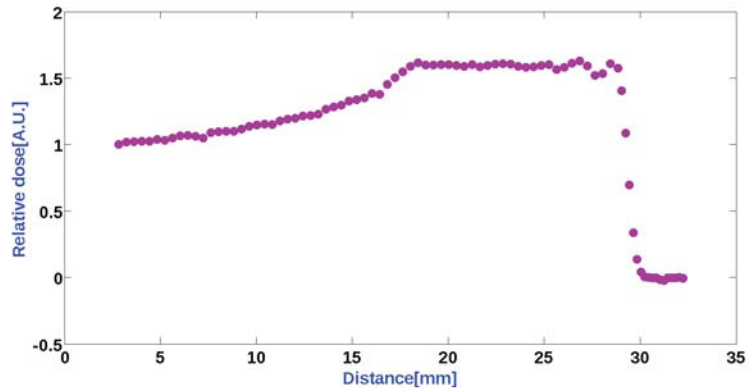

Figure 4.6: Example of Modulated Bragg peak acquired with an Advanced Markus chamber

of the modulated peak, similar parameters, as described above, are calculated. Moreover, for SOBPs, the modulation width is a key parameter. Figure 4.6 shows an example of SOBP obtained with a modulator wheel.

Absolute dosimetry

The dose measurements are performed in a water phantom, according to IAEA TRS 398 Code of practice and determined according to the formula 1.14 reported in chapter 1 .
Once the absolute dose at the irradiation point is measured, a set of in-transmission ionization chambers are cross-calibrated against the reference dosimeter. Therefore, the absorbed dose to water per monitor unit (cGy/M.U.) is on-line monitored and measured in order to perform irradiations at fixed amount of dose at the isocenter. The measurement is carried out at the entrance in the case of unmodulated Bragg peak and in the middle of SOBP, for the Bragg modulated peak, using the reference 25 mm diameter circular collimator.

4.3 Relative dose measurements with RCFs

Relative dosimetry measurements and fluence determination have been carried out at CATANA facility with conventionally accelerated protons using RCFs.
In order to deliver the desired amount of dose at the irradiation point, where RCFs have been placed, the procedure described in previous paragraph has been applied. RCFs have been used to estimate the fluence, the X and Y dose profiles and the depth dose distribution.
As said in chapter 3, RCFs are dose-rate independent relative dosimeters that allow the measurement of the delivered dose, providing 2D dose distributions, once calibrated against an absolute dosimeter. Due to polymerization of monomers by ionizing radiation, the active layer colour becomes darker and, quantitatively, it is measured through the optical density of the film (OD), as described in chapter 3. In particular EBT3 Radio Chromic films [98], have been used for the measurements.
RCFs have been cropped to have a 5x5 cm^2 area, an identification number and a reference were included to fix the film orientation.
The batch used for the measurements has been previously calibrated in terms of dose to water against the reference dosimeter.

For fluence and X/Y transversal dose profiles, a dose of 2.5 Gy has been delivered for three different collimators (20 mm, 25 mm and 20 mm antiscattering, figure 4.7, the last one specifically designed to decrease the lateral scattering and, therefore, to further improve the lateral dose fall-off), using a dedicated PMMA phantom placed at the irradiation point, 9 cm far from the collimator (Figure 4.8). To mea-

Figure 4.7: The three brass collimators used for the measurements, from left 20 and 25 mm of diameter and, the longer one, the 20 mm diameter antiscattering collimator.

sure the OD, the RCFs were scanned with an in transmission "Epson Expression 10000XL" scanner and digital images acquired in ".tiff" digital format.
The data analysis has been carried out through dedicated MATLAB scripts.
The 2D dose distributions have been obtained and, afterwards, fluence and X/Y profiles have been determined and compared with reference measurements.
In particular, the fluence (defined as protons per cm^2 in the region of interest) has been retrieved, for both the RCFs and for the reference detector, measuring the delivered dose and considering the mass stopping power for proton in water from ICRU49 tables at 59 MeV, taking into account the energy losses in the passive elements of the beamline (determined by Monte Carlo simulations).
The determined values are summarized in table 4.1. For the reference dose measurements a relative uncertainty of 2.5% has been estimated, according to the dosimetry protocol (IAEA TRS-398) and to the calibration procedures uncertainties.
For the dose measurements with RCFs, a relative uncertainty of 4% has been estimated, according to the scanning procedure and the intrinsic film uniformity.
In both cases, the correspondent fluence relative uncertainties are directly propa-

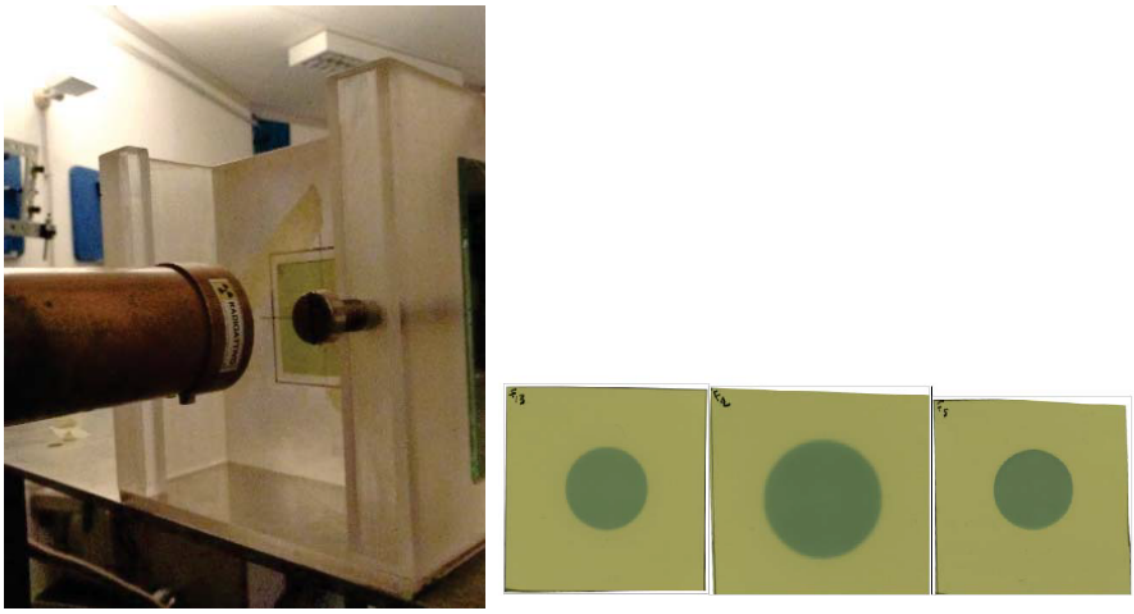

Figure 4.8: Left: PMMA phantom for the 2D transversal dose distributions measured with the RCFs. Right: RCFs irradiated respectively with (from left) the 20 mm, 25 mm and 20 mm antiscattering collimators.

Table 4.1: Comparison between the reference dose and the one measured with RFCs, with the correspondent fluence values. In the last line, the discrepancies are also shown for each collimator.

Collimator diameter [mm]	20	25	20 (antiscattering)
D_W with ref. det. [Gy]	2.50 $\pm$0.06	2.49 $\pm$0.06	2.49 $\pm$0.06
D_W with RCF [Gy]	2.44 $\pm$0.08	2.51 $\pm$0.09	2.43 $\pm$0.08
Flu with ref. det.$[p/cm^2]$	$(1.44\pm0.04)10^9$	$(1.43\pm0.04)10^9$	$(1.43\pm0.04)10^9$
Flu with RFC$[p/cm^2]$	$(1.41\pm0.06)10^9$	$(1.45\pm0.06)10^9$	$(1.41\pm0.06)10^9$
Flu Discrepancy	2.1 %	1.4 %	1.4 %

gated in the calculation because only constants are included in the formula.
In table 4.1, the discrepancy between the measured reference fluence value and the one obtained with RFC are also shown.
For the spatial dose distributions, both transversal and longitudinal profiles have been measured and compared with reference detectors.
The X/Y profiles measured with RCFs have been compared with a Hi-pSi diode (spatial resolution of 0.6 mm), typically used to check the transversal beam uniformity prior clinical treatment sessions.
RCFs can perform very high resolution 2D dose distribution measurements because, in principle, their intrinsic spatial resolution is dependent on the micrometric spatial distribution of polymers, responsible for the detector response. However, considering that the whole chain of measurement includes scanning the RCFs, the overall spatial resolution is mainly dominated by the resolution used in the scanner.
In order to obtain a good compromise between pixel fluctuations and reasonable resolution, a scanning resolution of 150 dpi has been used, correspondent to 0.17 mm, which can be finally considered as the overall RCFs spatial resolution for both the transversal and longitudinal dose distributions.
Comparisons between RCFs and X/Y relative dose profiles obtained with the diode for all the three different collimators show a very good agreement (Figure 4.9), with a maximum discrepancy between the field sizes (50% lateral dose distribution) measured with the two different detectors of 0.4 mm, as summarized in table 4.2.

Table 4.2: Comparisons between RCFs and X/Y relative dose profiles obtained with the diode for all the three different collimators

Collimator diameter [mm]	20	25	20 (antiscattering)
Discrepancy for the X profiles	0.4	0.4	0.1
Discrepancy for the Y profiles	10.3	0.3	0.1

To measure the longitudinal relative dose distribution, the experimental setup

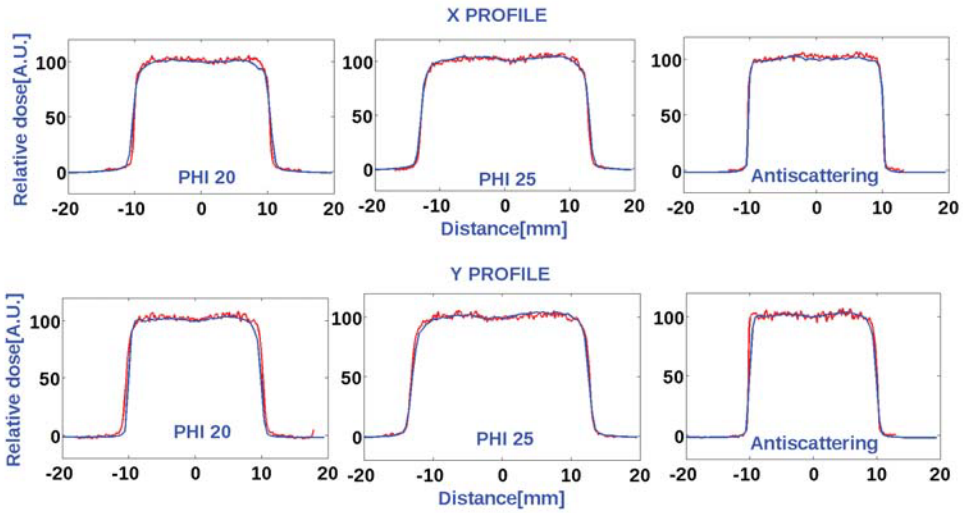

Figure 4.9: X and Y transversal dose profiles, respectively on the top and on bottom, for both diode and RCFs respectively obtained using, from left, a 20 mm, 25 mm and 20 mm antiscattering collimator

shown in Figure 4.11 has been used. Basically, a single RCF has been placed in a dedicated PMMA phantom, designed on purpose. In particular, the phantom is shaped in a way that the RFC is fixed between two half trapezoidal prisms, with the aim of determining a small tilt angle between the beam direction and the RCF plane (of about 5 deg). Irradiations were performed with this peculiar

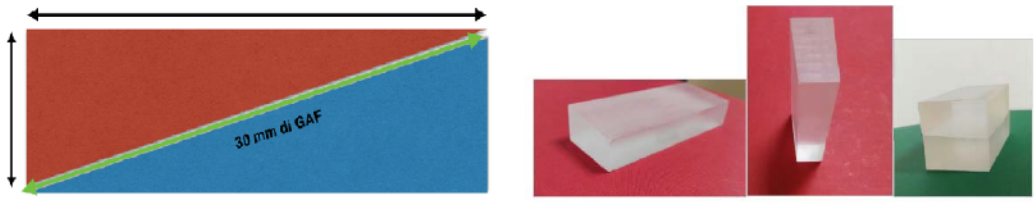

Figure 4.10: Left: Schematic drawing of the PMMA phantom used to irradiate the RCF in the longitudinal direction, with a specific tilt angle. Right: pictures of the PMMA phantom used in the measurement, composed by two trapezoidal prisms.

configuration to avoid the presence of a secondary peaks caused by partial or total

slowing down of protons in the substrate layers covering the active layer and also to decreases the uncertainty in the material conversion. The film has been placed between the two prisms composing the phantom, as shown in Figure 4.11. Three

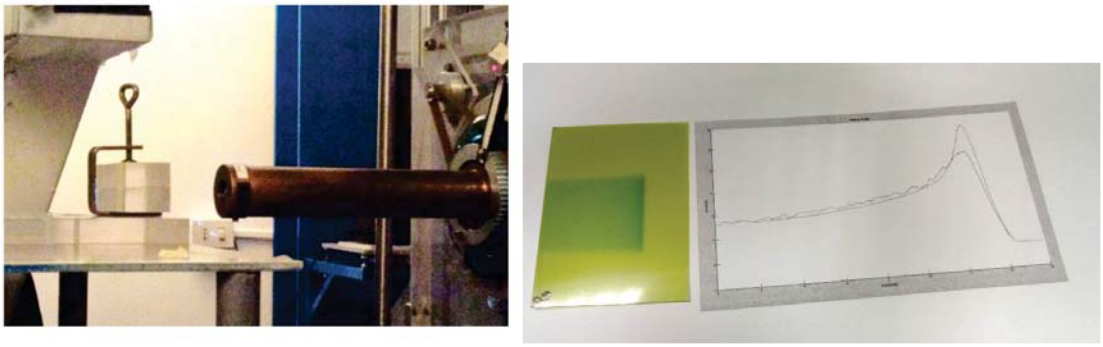

Figure 4.11: Picture of the experimental setup used for acquiring longitudinal depth dose distributions with one single RCF, where the final brass collimator is visible and the RCF pressed between the two prisms.

different configurations have been considered, in order to have respectively three different ranges in water:

- pristine peak, correspondent to about 29 mm range in water;
- range shifter "$A7$", correspondent to about 22 mm of range in water
- range shifter "$A15$", correspondent to about 13 mm of range in water

As for the X/Y transversal profiles,the longitudinal dose distributions obtained, have been compared with the RCF using the described setup with the ones obtained with a reference dosimeter (Markus chamber in a water phantom with a spatial resolution of 0.1 mm).
As shown in Figure 4.12, once performed the proper material conversions (to obtain depth in water also for the RFC case), a good agreement has been found in terms of measured range in water, demonstrating the reliability of the described experimental procedure. Anyway, as expected, saturation effects of the RCF response are clearly visible, when comparing with a reference dosimeter. These are due to a

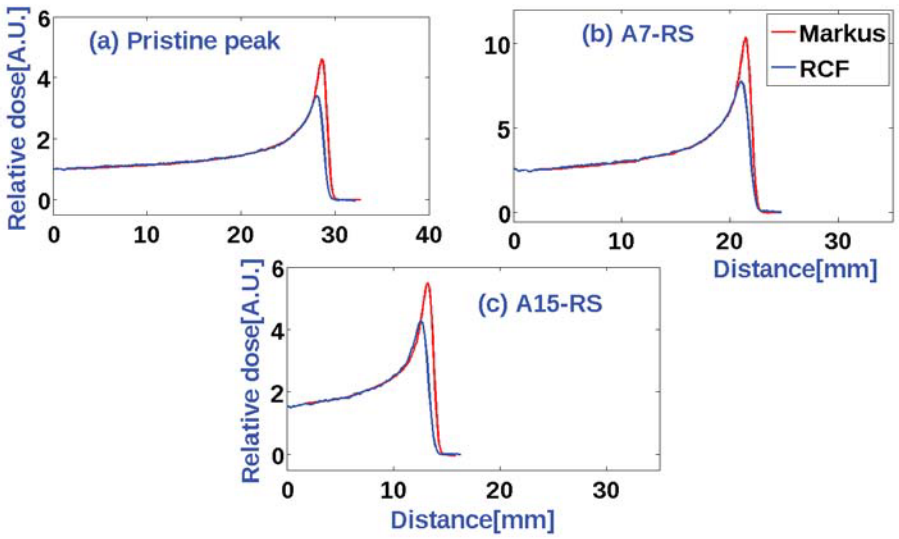

Figure 4.12: Comparison between longitudinal dose distributions (Bragg peaks) obtained with the Markus chamber in the water phantom and the ones obtained with RCF for all the three different ranges: a) pristine peak, b) "*A7*" range shifter, c) "*A15*" range shifter.

well known "quenching" effect of the RCF at higher LET, reported elsewhere [99]. In particular, it has been experimentally demonstrated that for proton energies lower than 10 MeV (correspondent to LET higher than 5 KeV/um), the response of RCFs start being affected by saturation effects which could be corrected once the local energy spectrum at the specific depth in water is known. However, for the purpose of this measurement, the range measurements are not sensibly affected by that, as shown in Figure 4.12.

The range at 90% of dose distal fall-off has been retrieved and compared with the once obtained with the reference dosimeter.

As shown in table 4.3, a maximum discrepancy of 0.6 mm has been found between the two different methods, showing the high level of reliability for longitudinal dose distribution measurements using RCF.

Table 4.3: Discrepancies, in mm, between the range at 90% of dose distal fall-off for the Markus chamber in the water phantom and the one obtained with the RCFs

Pristine peak	range at 90% of dose distal fall-off [mm]
RCF	28.5
MARKUS	28.8
Discrepancy	0.3
A7 range shifter	**range at 90% of dose distal fall-off [mm]**
RCF	21.4
MARKUS	21.6
Discrepancy	0.2
A15 range shifter	**range at 90% of dose distal fall-off [mm]**
RCF	12.9
MARKUS	13.5
Discrepancy	0.6

4.4 Absolute dose measurements with the Faraday cup

As discussed in the chapter 3, the Faraday cup (FC) is a detector aimed to measure the collected charge when charged particle beams are impinging on that.
As said, it is typically equipped with an internal electrode which has the purpose to repel secondary electrons produced in the entrance kapton window (placed to allow vacuum conditions inside the cup) and, on the other side, to collect the secondary electrons produced by the interaction of primary particles with the cup itself, which could go out from the FC. Therefore, basically, the electrodes is aimed to optimize the charge collection, reducing the systematic uncertainties.
The characterization of the FC has been performed at CATANA facility with a 62MeV of protons.
The FC has been placed about 9cm downstream the final collimator along the CATANA beam-line and a 20mm diameter collimator has been used for the measurements (Figure 4.13). The FC operating vacuum was 10^{-5} mbar. In the next

Figure 4.13: Faraday Cup mounted along the CATANA beam-line

sections the results related to the FC characterization will be discussed.

Charge-voltage characteristic

In order to find the operation region of FC, collected charge for different applied voltages has been measured connecting the FC with an electrometer (Keithley 6517A).
The voltage has been varied from -2500 Volt to 2500 Volt, delivering fixed amount of dose (15 Gy), which has been monitored with online transmission ionizations chambers. Each charge measurement has been obtained integrating the current signal, fig. 4.14, for the time interval required to reach the fixed amount of dose. The signal of FC has been acquired using a LABVIEW software.

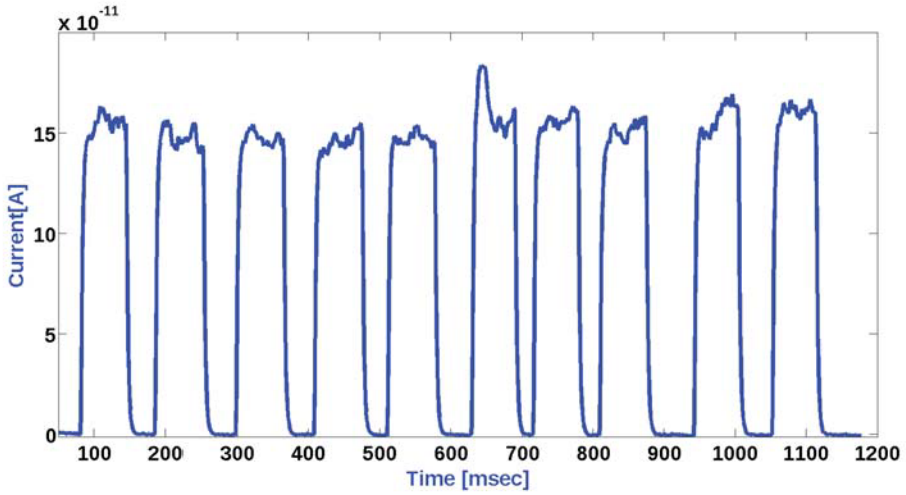

Figure 4.14: Exemple of current signal acquired with the FC

As shown in Figure 4.15, a typical plateau in the negative voltage range between about -2500 V and -400 V can be observed (working region); on the other hand, for positive voltages a collected charge dependence increasing with the voltage applied is evident.
The charge collection response observed in the FC is in agreement with the typical trend of standard FCs used for absolute dosimetry [88].

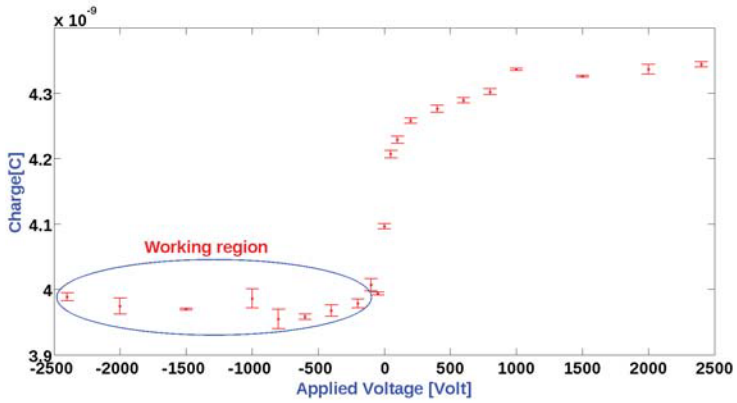

Figure 4.15: Collected charge in the FC as a function of the applied voltage on the electrode. On the left, it is clearly visible the working region (for negative voltages)

Dose-rate dependence

A complete characterization of the FC response in terms of dose-rate has been also carried out. A tantalum foil (SEM) placed in-vacuum along the CATANA beam-line allows to monitor in real time the proton beam current, which can be varied at the injection in the cyclotron and monitored at the beginning of the Catana beam line with the mentioned detector. Once cross-calibrated with a reference detectors at the measurement point, SEM can provide a measurement of the dose-rate, which has been varied from few Gy/min up to about 100. The response of the SEM is independent on beam current for the specific used range and, therefore, it has been used as a reference to study the FC response. The ratio between the FC and SEM response has been determined as a function of the dose rate, fixing the electrode voltage at -1500 V,fig. 4.16.

Each point in the plot has been obtained integrating both SEM and FC detectors signals and calculating, as mentioned, their ratio.

As shown in figure 4.16, for the explored dose-rate interval, FC is, as expected, independent on proton beam dose-rate, considering the experimental uncertainties and the fluctuations. Intrinsic limits due to proton beam acceleration in the cyclotron and the subsequent transport has not allowed to investigate higher dose rates.

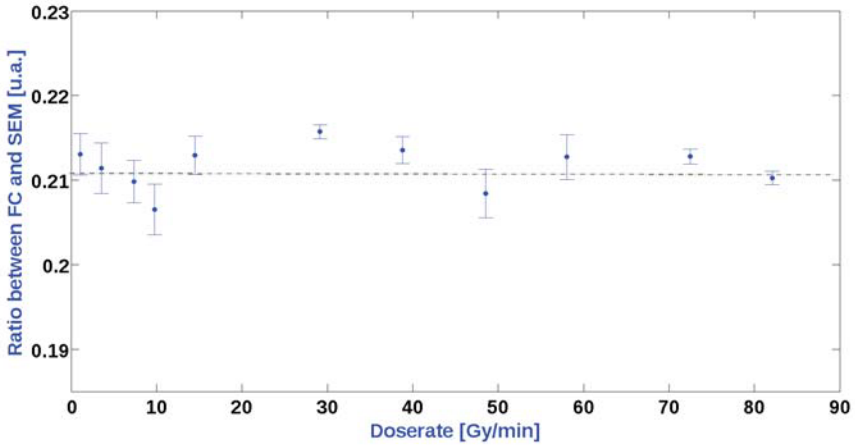

Figure 4.16: Ratio between the FC and SEM response as a function of the dose-rate.

Dose dependence

The linearity of the FC charge as respect the released dose has been verified in a dose interval ranging between about 10 and 100 Gy. The measure has been conducted with an electrode voltage of $-1500V$.

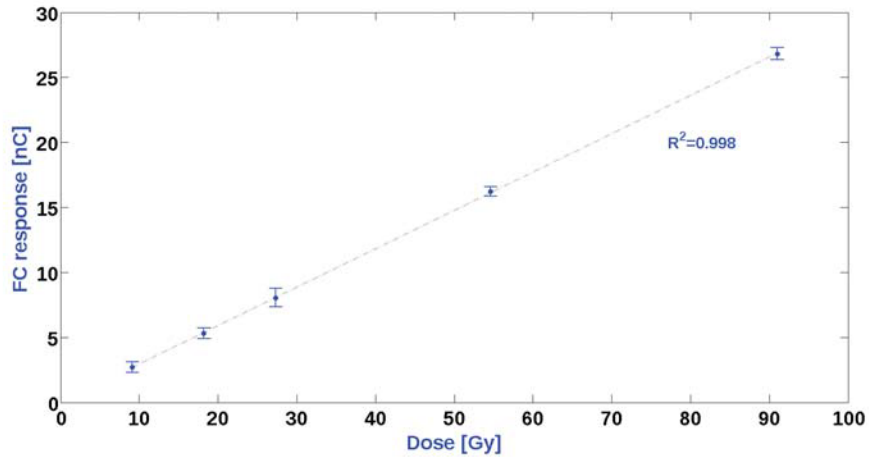

Figure 4.17: The linearity of the FC charge respect the released dose

The result of the dose dependence has been reported in figure 4.17 where, as expected, a linear response of the FC with the absorbed dose has clearly shown.

For each fixed dose value, a charge measurement has been performed. The linearity of FC response respect the released dose represents the repeatability of our charge measure.

4.4.1 Absolute dose measurements with the FC

Ones the FC has been characterized, founding the proper working region, a measure of absolute dose has been performed.
As said in chapter 3, the charge measured by the FC is just one of the physical quantities necessary to determine the absolute dose.
For this specific measurement, the formula 5.6 of chapter 3, results simplified, due to the fact that 62 MeV mono-energetic beams are used. Indeed, in this case, as already explained for the fluence measurements with RFCs, the stopping power in water has been retrieved using ICRU49 tables for the corrected energy of 59 MeV at the irradiation point about 3 m far from the vacuum pipe and 9 cm far from the final collimator (obtained considering the energy losses in the passive elements of the beam line).
In order to calculate the A_{eff}, the RCFs have been scanned with an in transmission scanner and digital images have been acquired.
The data analysis has been carried out through dedicated scripts in MATLAB, obtaining the information on X/Y lateral profiles and applying the formula 3.3 of chapter 3, A_{eff} has been calculated.
The effective area has been measured irradiating the RCFs which have been placed just in front of the FC entrance window, using a 20 mm brass collimator, as shown in Figure 4.18. The same methods described before for RCFs measurements has been applied, obtaining with the mentioned spatial resolution (0.17 mm) the information on X/Y lateral dose profiles, necessary to calculate A_{eff} .
Using the same procedure described above for the fluence measurement with RCFs, the FC has been irradiated at the reference position where the reference Markus chamber has been previously placed, in order to deliver a specific amount of dose with an uncertainty on beam calibration of 2.5%.
Collected charge at -1500 V of applied voltages has been measured as previously

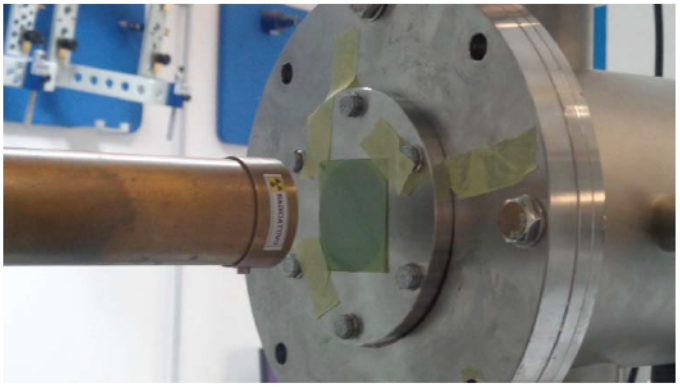

Figure 4.18: RCF placed just in front of the FC for the beam spot measurement, necessary to retrieve the A_{eff} .

described, i.e. connecting an electrometer (Keithley 6517A) to the FC.
Each charge measurement has been obtained integrating the current signal for the time interval required to reach the fixed amount of dose (15 Gy,as typically used in the clinical practice) and the measurements were repeated for all the three different collimators.
In order to calculate the overall uncertainty on the absolute dose measurement with the FC it is necessary to quantify the contribution due to the uncertainty on collected charge, on the stopping power and the one related to the beam effective area.
For the collected charge, the considered uncertainty is basically determined by the standard deviation related to the specific set of repeated measurements at a the fixed dose value.
For the stopping power value, as mentioned it has been retrieved using the ICRU 49 tables for a correspondent energy at the irradiation point of 59 MeV. Tabulated uncertainties have been used on this regard. The uncertainty of A_{eff} is more dominant, because small variation on the beam shape and diameter sensibly influence the effective area, according to the formula 3.3. In order to obtain a good compromise between pixel response fluctuations and resonable spatial resolution, a scanning resolution of 150 dpi has been used, as the same of RCFs, correspondent to 0.17mm. This could be considered as the overall 2D spatial distribution over

the same beam spot. Beyond that, the impact of the dose uncertainty related to the RCF intrinsic inhomogeneity has to be considered, although this has a minor influence on the final effective area determination, due to the fact the a relative dose information is necessary in this concern.
Applying the error propagation and including all the mentioned contributions, an overall uncertainty of 4.5% has been obtained for the absolute dose measurement with the FC. Moreover, similarly to what has been done for the relative dose measurements, the obtained dose values have been compared with ones measured with the reference dosimeter(Markus chamber) in the same irradiation conditions, again delivering a dose value typically used in a clinical session, i.e. 15 Gy.

Table 4.4: Results of absolute dose calculate in different configuration

Collimator diameter [mm]	20	25	20 (antiscattering)
D_W with reference detector [Gy]	15.0 ±0.4	15.0 ±0.4	15.0 ±0.4
D_W with FC [Gy]	14.5 ±0.6	14.7 ±0.7	14.5 ±0.6
Discrepancy	3.3 %	2.0 %	3.3 %

Results are summarized in table 4.4: a maximum discrepancy of 3% between the does measured with the reference detector and the one with the FC has been found. The results discussed above demonstrate that, for conventionally accelerated beams, the detectors used in the ELIMED beamline allow to perform relative and absolute dose measurements characterized by uncertainties which are acceptable for multidisciplinary and medical applications.

Chapter 5

Experimental characterization of the dosimetric detectors with laser-driven ion beams

The dosimetric detectors of ELIMED beam line, FC, SEM and IC, described in chapter 3, have been characterized in an experimental campaign carried out using the SAPHIR laser system at Laboratoire d'Optique Appliquée (LOA, Paris, France) [30].
When high power laser pulses interact with a target, the production of plasma is tipically accompanied by the emission of an intense electromagnetic pulse (EMP), which propagates inside and outside the interaction chamber.
The EMP could influence the response of detectors.
Indeed, the aim of the experiment has been the characterization of the detectors response, in order to reduce the EMP signal and to investigate the frequencies of the signal due to the oscillation modes of the EMP inside and outside the interaction chamber. The setup and the readout system of each detector have been optimized, in order to increase the ratio between the proton signal and the EMP noise, [100][101].
The time evolution signal for each detector has been measured and an estimation of dose delivered by a laser-driven proton beam has been determined with the FC

dosimeter.
In next sections, the experimental setup and the results obtained for each device will be presented.

5.1 Description of the LOA-laser facility

The experimental characterization of the dosimetric devices has been performed at the LOA laser laboratory in Palaiseau (France) using the SAPHIR laser system. The SAPHIR laser system is a femtosecond, double CPA (chirped pulse amplification) laser chain, with the central wavelength of about 800nm. It has been designed to deliver pulses with 3 J of energy on target, time duration of about 25 fs, a peak power of 200 TW at a repetition rate of 5 Hz with a time duration of 25 fs. The ion beams are generated through the laser-matter interaction,

Figure 5.1: Picture of the SAPHIR laser system

in the TNSA regime. The laser beam produced by the amplification system, is transported toward the experimental chamber, with turning boxes which bring the laser beam downstairs in the pit where the experimental chamber is located. A deformable mirror corrects the beam phase front, reducing some of the distortions added during propagation throughout the chain.
During the experimental campaign the laser pulse has been focused at 30° off-axis

by a parabolic mirror with a focal spot size of 10 μm diameter and with a 45° incidence angle onto a 5μm thick titanium foil.
The interaction chamber for particle acceleration experiments is a steel octagonal chamber with a diameter of 1.6 m.
Protons come out from contaminants present on the target surface, placed inside the interaction chamber. The experimental setup used for the characterization of each detector and type of measurements will be described in sections 5.2, 5.3, 5.4 and 5.5.

5.2 Characterization of the detector responses to reduce the EMP signal

5.2.1 FC: EMP characterization

The experimental set-up, to characterize the FC response in order to reduce the EMP, is shown in figure 5.2.
The FC was placed at 45° with respect to the target normal about 70 cm from the target. It has been mounted, directly, attached to the interaction chamber, without the entrance kapton window (see chapter 3 for the technical specifications of FC).
The vacuum cross hosting the detector and the feed-through connectors have been electrically insulated from the target chamber using insulating O-ring and clamps.
In order to characterize the optically accelerated ion beams, a Thomson parabola (TP), placed at 0° with respect to the target normal about 80 cm from the target, has been used providing spectral information on the ion beam.
Combining data of TP and of Radiochromic films (RCFs), the spectrum of the protons and the angular aperture can be calculated, (see [56]).
According to the laser-driven beam angular aperture measured using a RCF stack (see fig.5.3) placed at about 50 mm from the target, no ion beam signal is expected to be measured by the FC placed at 45°. Therefore, it is possible to measure the EMP signal propagating in the interaction chamber only.

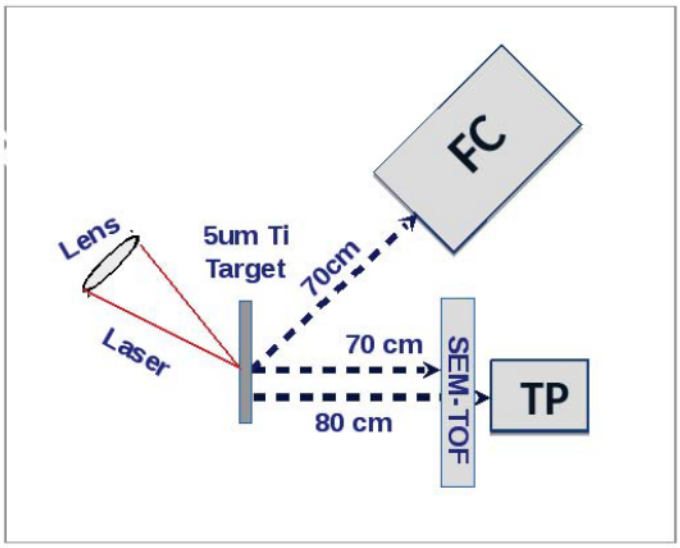

Figure 5.2: Schematic layout of the experimental setup for FC response characterization in order to reduce the EMP

The FC signals have been acquired, with a 2.5 GHz 40Gs/s LeCroy digital oscilloscope terminated with a 50 Ω load impedance.

All the shots have been analyzed in order to compare the characteristics of the

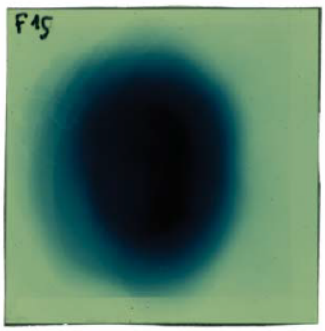

Figure 5.3: Beam spot size measured using RCF film at 48 mm from the target. Beam spot diameter resulted to be 33 mm.

signal in terms of amplitude, time duration and principal frequencies.
As shown in figure 5.4, the high-pulsed laser interaction with the target produces an high electromagnetic noise and the signal recorded is bipolar with maximum amplitude of about 4 V (peak to peak) and time duration of about 500 ns. Particulary, a fast oscillation starts when the plasma is created and it is dampened in about 200 ns. After about 200 ns a lower oscillation starts characterized by maximum amplitude of about 1 Volt (peak to peak), which rapidly falls to zero. Such strong EMP signal may be comparable or even predominant with respect to

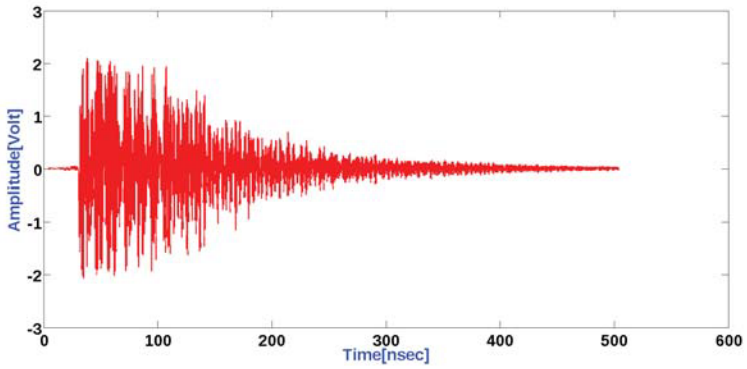

Figure 5.4: The EMP signal registered by the FC placed at 45° with respect to the target normal direction at about 70 cm from the target.

the charged particle signal and can disguise the ion signal.
In order to discriminate the ion signal from EMP noise contribution, an identification and characterization of such noise is crucial.
Therefore, to study the frequency components of the noise signal, the Fourier Transform analysis has been carried out using the software MATLAB, using the Fast Fourier Transform (FFT) algorithm [103]. In general the Fourier Transform is defined for continuous functions, which in physics can describe some physical characteristics. In this case, the signal is a discrete signal and for this reason it is more correct to refer to a sequence of sampled values characterized by a time difference equal to $\Delta t = 0.1ns$ (the time sampling of the scope) and a critical frequency given by:

$$f_c = \frac{1}{2}\Delta t \tag{5.1}$$

If N is the number of the sampled values k and n are respectively the index to distinguish consecutive points in time and frequency domain, the FFT could be approximated, for discrete functions, as:

$$h_k = h(t_k)t_k = k\Delta tk = 0, ...N-1 \tag{5.2}$$

$$H(f_n) \sim \sum_{k=0}^{N-1} h_k e^{2\pi i f_n t_k} \Delta t] = \Delta t \sum_{k=0}^{N-1} h_k e^{2\pi \frac{ikn}{N}} \tag{5.3}$$

$H(f_n)$ is the frequency distribution obtained by the Fourier transform of the input time distribution. However, the calculation expressed in formula 5.3 needs a long computation time due to the great number of processes that have to be processed (of the order of N^2).

On the other hands the discrete Fourier transform can be computed in $N\ log_2\ N$ operations with the algorithm FFT.

Indeed, by using this algorithm the time needed to process N data is drastically decreased. The algorithm is built on the fact that a Fourier Transform of length N can be rewritten as the sum of two discrete Fourier Transforms, each of length $N/2$. The FFT algorithm gives a complex number with a real and an imaginary part. It is possible, therefore, to obtain the distribution of the real part or the imaginary part of the Fourier Transform as function of the frequency. A quantity that can be also defined is the Power Spectral Density that is the modulus-squared of the discrete Fourier Transform normalized with respect to the total number of samples. The power corresponds to the sum of the modulus-squared of the Fourier coefficients.

Figure 5.5 shows FFT of the signal shown in Fiure 5.4.

As one can see from figure 5.5, frequency components ranging from ten's of MHz up to about 1 GHz can be observed.

In order to investigate and attenuate the EMP noise affecting the FC response, low-pass filters from 100 MHz to 900 MHz have been used. Figure 5.6 shows the EMP signals measured by the FC placed at 45° with respect to the target normal

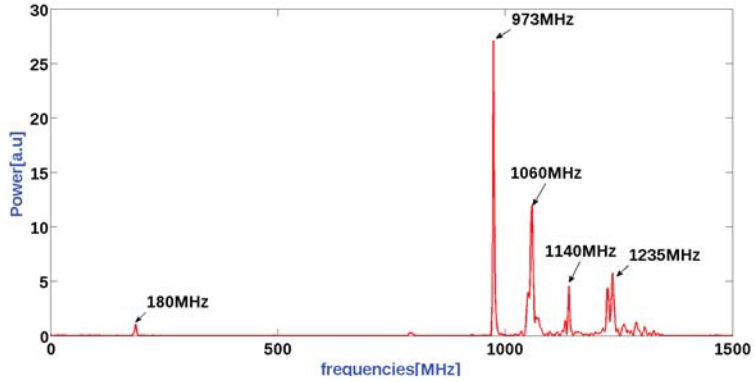

Figure 5.5: FFT of the signal in fig. 5.4

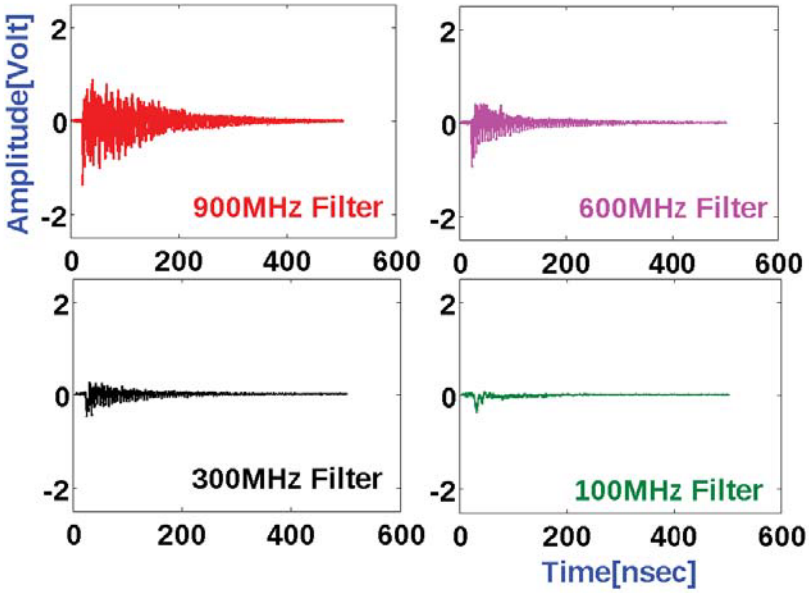

Figure 5.6: EMP signals measured by the FC, placed at 45° with respect to the target normal direction at about 70 cm from the target, using 900 MHz, 600 MHz, 300 MHz and 100 MHz cut-off low-pass filters.

direction at about 70 cm from the target using, respectively, 900 MHz, 600 MHz, 300 MHz and 100 MHz cut-off low-pass filters. As one can clearly see from the comparison shown in figure 5.6, the EMP signal amplitude can be attenuated using proper low-pass filters from ten's of Volt down to hundreds of mV and the signal can be dampened in a short time scale of the order of tens of ns.
In such a way, due to the low-pass filter attenuation, it will be possible to discriminate a signal generated from the fast ion component, particularly proton, accelerated in the laser matter interaction.
Moreover, as one can observe from the FFT of the signal acquired using the 100 MHz low-pass filter, shown in figure 5.7, the contribution of the frequency components above 100 MHz results completely wiped out.

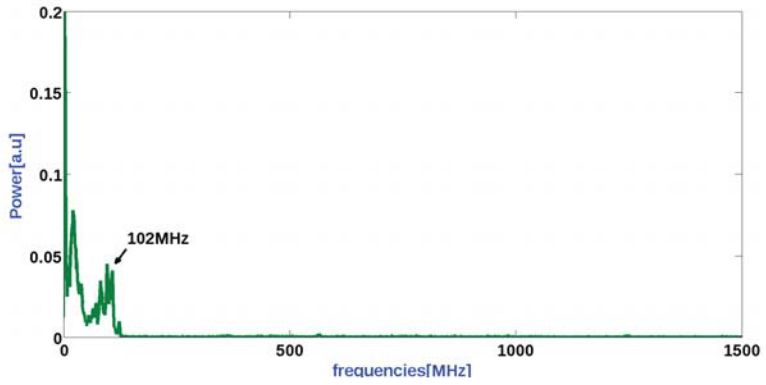

Figure 5.7: FFT of the signal in Fig.5.6 when a LP filter of 100MHz is used.

Furthermore, a characterization of the FC response, placing the FC at 2m from the interaction chamber, in air, has been also performed (the entrance kapton window of the FC has been mounted). In figure 5.8 the signal acquired when the FC is at 2m from the interaction chamber is shown. The bipolar signal shown in figure 5.8, has a maximum amplitude of about 100mV, about two order of magnitude lower compared to the signal shown in figure 5.2. The EMP contribution might still be dominant with respect to the fast proton component signal. Indeed, from the FFT of the EMP signal registered, shown in figure 5.9, frequency components ranging from ten's of MHz up to about 1.2 GHz can be observed. This confirms

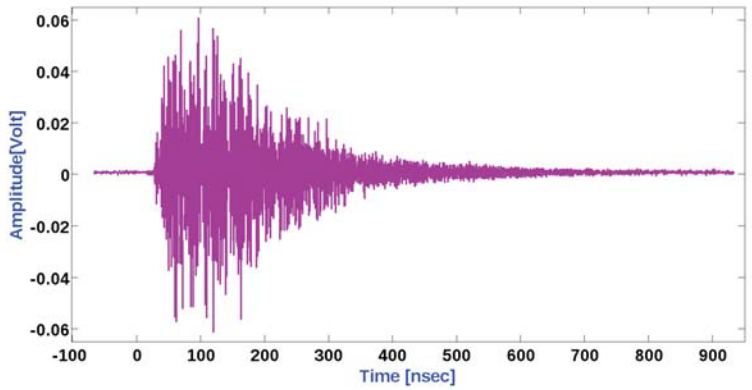

Figure 5.8: FC signal recorded in air at about 2m from the interaction chamber.

how the production of plasma can be accompanied by the emission of EMP within and outside the laser target chamber. So, it is necessary to study the detector responses to optimize setup and readout system to increase the ratio between the proton signal and the EMP noise.

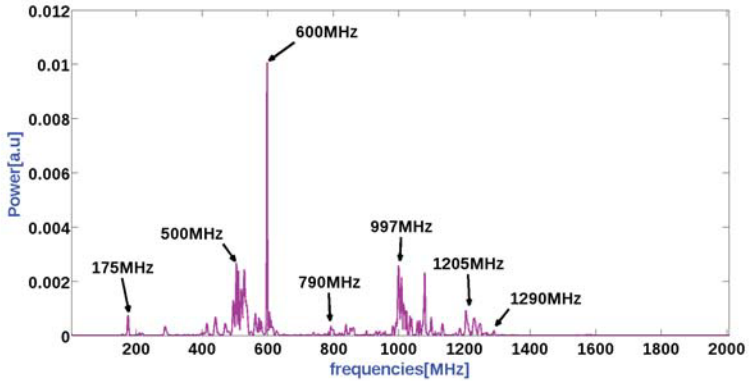

Figure 5.9: FFT of FC signal shown in Fig. 5.8.

5.2.2 SEM: EMP characterization

A characterization of the EMP signal acquired by the SEM has been performed using two different setups.

In a first configuration the SEM detector have been placed at about 70 cm from

the target inside the interaction chamber, both along the target normal direction and at about 10° with respect to the target normal direction (see fig.5.10), in order to measure only the EMP inside the interaction chamber. The experimental set-up

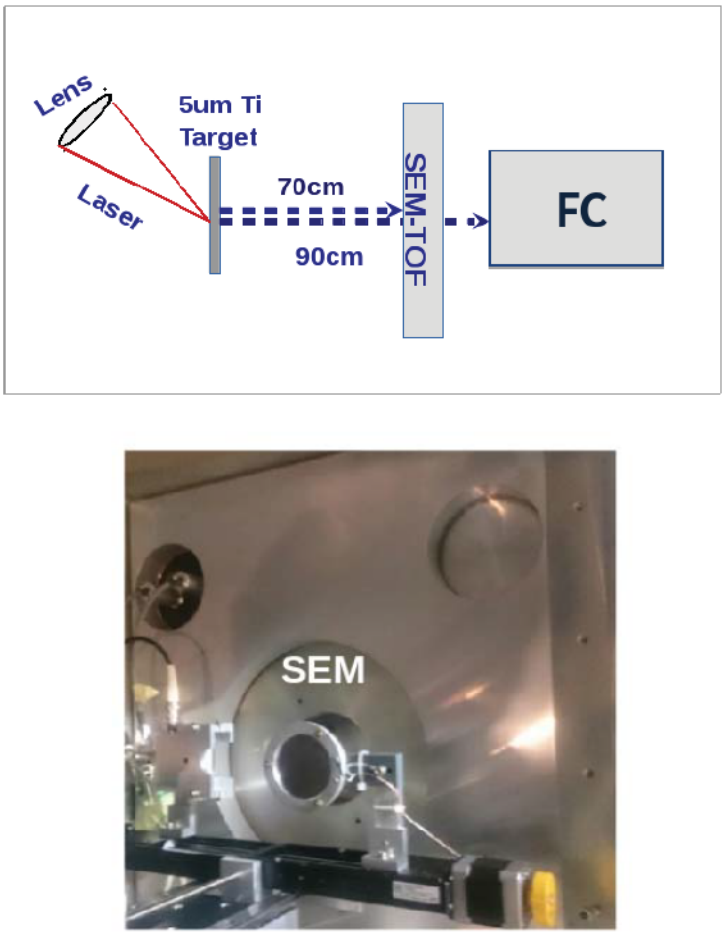

Figure 5.10: SEM placed at about 70 cm from the target and about 10 with respect to the target normal direction, inside the target chamber.

is shown in figure5.10.

The SEM signal has been acquired using a 2.5 GHz 40Gs/s LeCroy digital oscilloscope terminated with a 50 Ω load impedance.

In order to study only the EMP noise affecting the detector, the SEM has been shielded using a set off iron blocks assuring that no ion signal could be detected.

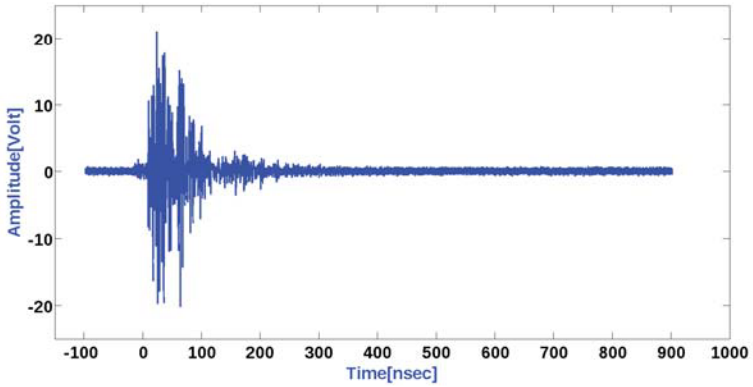

Figure 5.11: Typical EMP signal registered by the SEM placed inside the target chamber at about 70 cm from the target at about 10° from the target normal.

In figure 5.11 is shown a typical EMP signal registred placing the SEM detector inside the interaction chamber at about 70cm and about 10° with respect to the target normal direction.
As shown in figure 5.11, a huge EMP noise of about 40 V maximum amplitude (peak to peak) dominates the signal with time duration of about 200 ns. Such extreme EMP condition hinders the possibility to measure a signal originating from the ion beam accelerated from the target, similarly to the case of the FC described in section 5.2.1.
Figure 5.12 shows the FFT of the signal shown in Fiure 5.11. As one can see from figure 5.12, frequency components ranging from ten's of MHz up to about 500 MHz can be observed.
In order to reduce the EMP noise measured from the SEM, the detector has been moved far away from the target, i.e. the EMP source.
The SEM detector has been placed at 165 cm downstream the target, along the target normal direction, inside a DN100 vacuum cross connected to the interaction chamber using a DN 40 pipe (see figure 5.13), used to increase the distance between the SEM and the laser-target interaction point and to shield the detector itself from the EMP resonating inside the interaction chamber. The vacuums cross hosting the detector and the feed-through connectors have been electrically

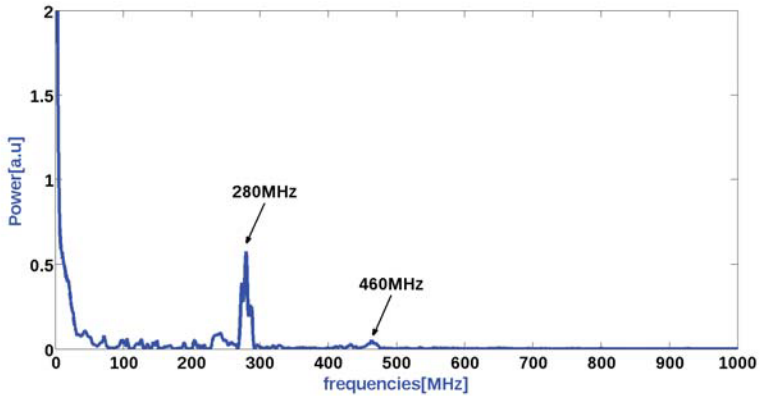

Figure 5.12: FFT of signal in Fig.5.11.

insulated from the target chamber using insulating O-ring and clamps.

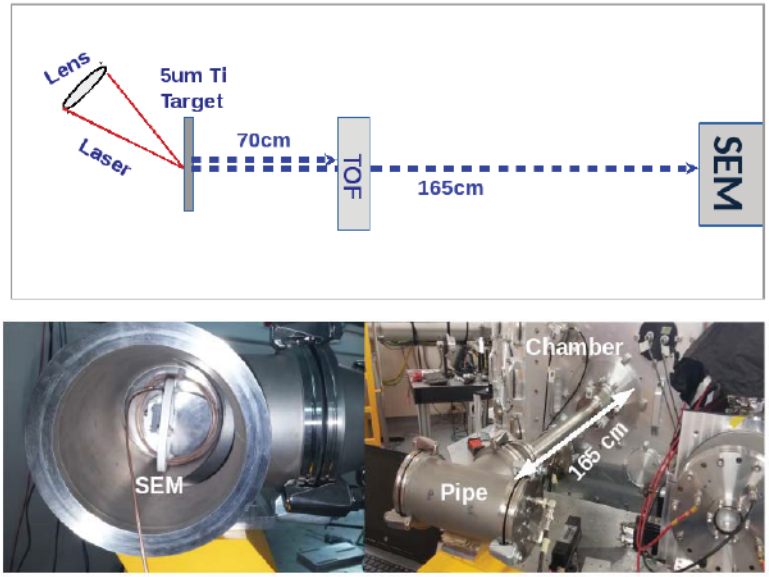

Figure 5.13: SEM detector placed 165 cm downstream the target along the target normal direction (at 0°), inside a small vacuum cross, connected to the interaction chamber through a pipe.

Figure 5.14 shows a signal acquired in this configuration, i.e. the SEM detector placed at 165 cm along the target normal direction. A relevant EMP attenuation, more than two order of magnitude lower compared to the signal shown in figure

5.11 can be observed and a slow ion contribution can be also disentangled at about 200 ns also thanks to the longer flight path (in time-of-flight (TOF) techniques the distance from target to detector is named flight path), nevertheless, the EMP noise is still dominant with respect to the fast proton contribution in the time region up to 150 ns.
The frequency components shown in figure 5.5 of the EMP signal shown in figure 5.16 ranging from ten's of MHz up to about 900 MHz can be observed.

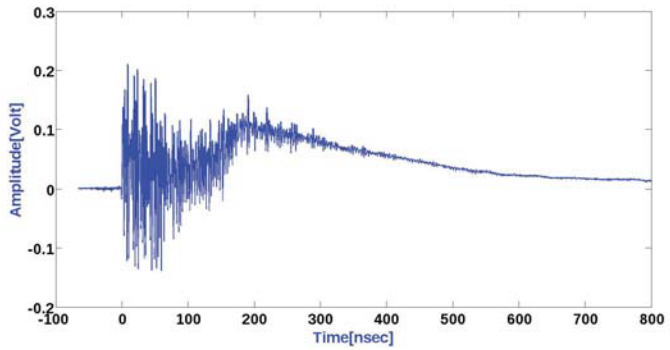

Figure 5.14: Typical EMP signal registered by the SEM at 165 cm along the target normal direction.

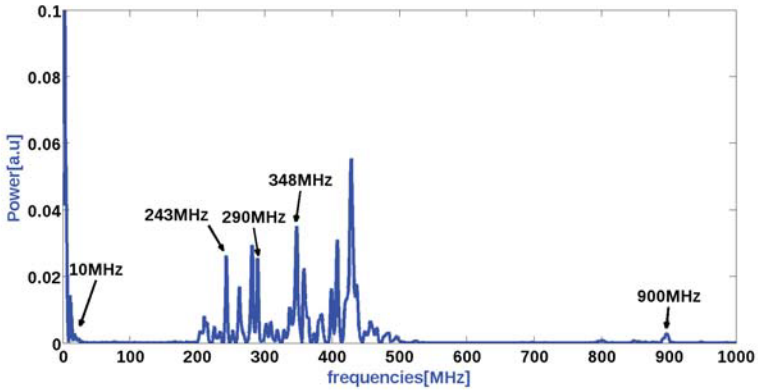

Figure 5.15: The FFT of the signal in Fig.5.14.

In order to further reduce the EMP noise affecting the fast proton signal, low-pass filters with different frequency cut-offs ranging up to 100 MHz have been used.

In agreement with the EMP characterization results obtained with the FC, the EMP becomes almost negligible using a 100 MHz low-pass filter.

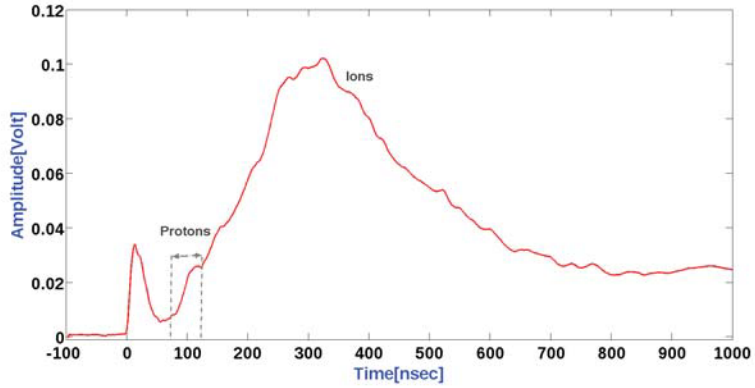

Figure 5.16: Typical ion signal registered by the SEM at 165 cm along the target normal direction.

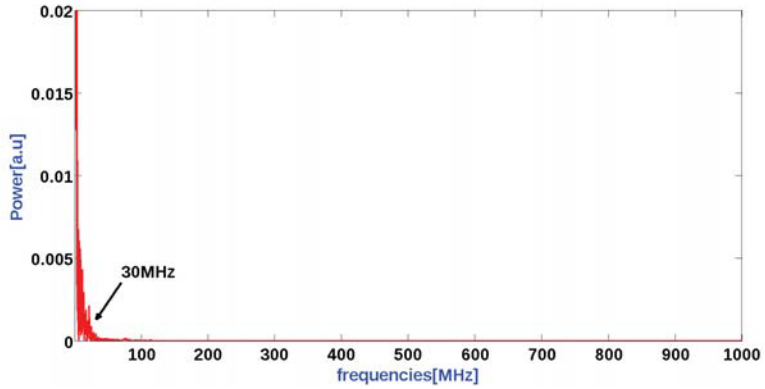

Figure 5.17: FFT of Fig.5.16

Figure 5.16 shows a typical time evolution signal registered with the SEM, placed 165 cm downstream the target, using a 100 MHz low-pass filter.
Using a 100 MHz filter, as shown in figure 5.16, a broad structure due to the slow ion contribution can be clearly observed for time values greater than 200 ns, moreover it is also possible to distinctly discriminate the proton contribution for time values shorter than 150 ns. Figure 5.17 shows the FFT of the signal shown

in Fiure 5.16. Using a 100MHz, (figure 5.17), the contribution of the frequency components above 100 MHz results completely wiped out.

5.2.3 IC: EMP characterization

An accurate characterization of the multi-gap IC response has been performed in order to reduce the EMP, as the others devices. In figure 5.18 is shown the exper-

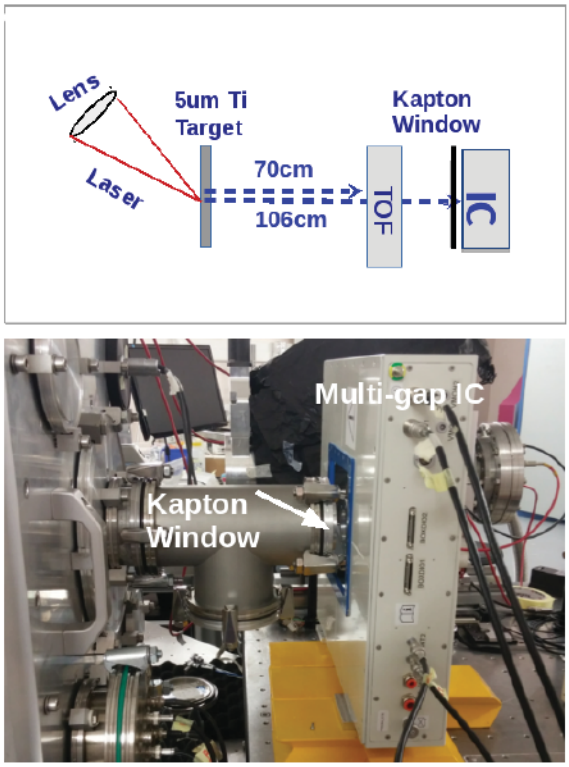

Figure 5.18: Schematic layout of the experimental setup for IC characterization in order to reduce the EMP contribution to the signal.

imental set-up used.

In order to perform the characterization of multi-gap IC to reduce the EMP, the measurement has been carried out, placing the multi-gap IC in air, at 0° with respect to the target normal. The multi-gap IC has been placed in front of the kapton window mounted with a flange at the intercation chamber (figure5.18).

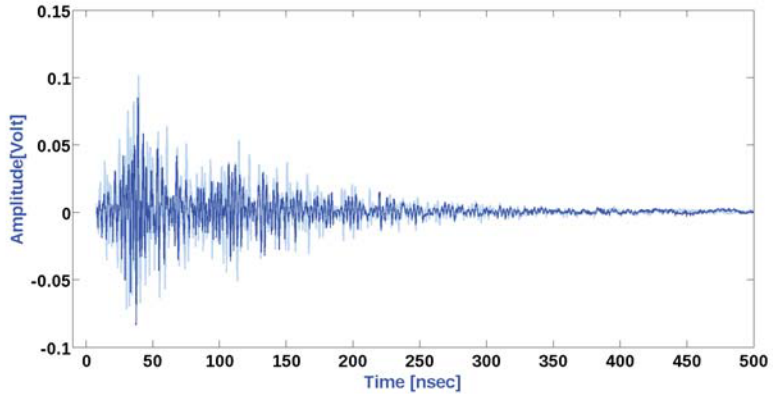

Figure 5.19: EMP signal acquired with multi-gap IC (IC_1 in light blue and $IC2$ in blue) placed at 0° with respect to the target normal about 1m from the target and at 1 cm from the kapton window.

The kapton window allow the exit of the laser-driven ion beam in air.
The ion signals have been acquired at different distances from the kapton window, connecting a 2.5 GHz Le Croy digital oscilloscope directly with the multi-gap IC. In figure 5.19, is reported a signal acquired, placing the multi-gap IC at about 1m from the target and 1cm from the kapton window.

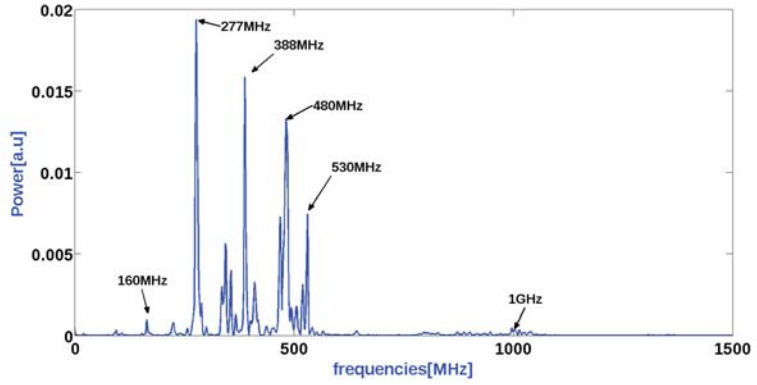

Figure 5.20: FFT of EMP signal of Fig.5.19.

As one can see in figure 5.19, the laser interaction with the target produces an high electromagnetic noise and the signal acquired is bipolar with maximum amplitude of about 100 mV (peak to peak) and time duration of about 500 ns.

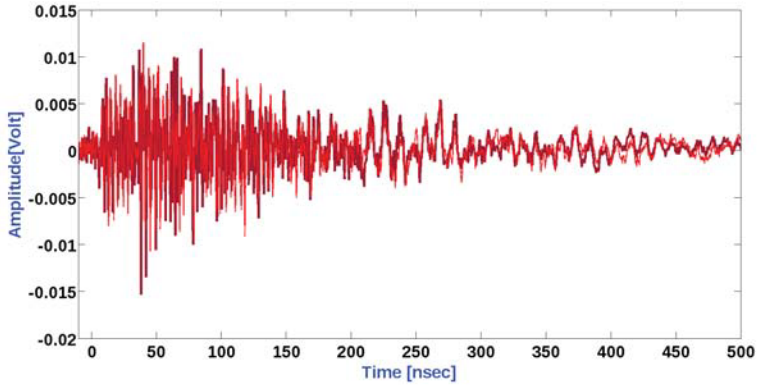

Figure 5.21: EMP signal acquired with multi-gap IC (IC_1 in red and $IC2$ in dark red) placed at 0° with respect to the target normal about 2m from the target and at 1m from the kapton window.

In particular, a fast oscillation starts when the plasma is created and it is dampened in about 200 ns. After about 200 ns the oscillation rapidly falls to zero.

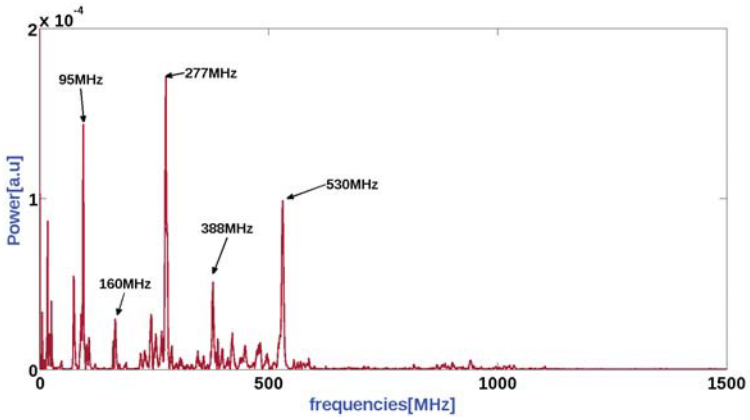

Figure 5.22: FFT of EMP signal in Fig.5.21.

In order to characterize the EMP contribution in terms of frequency components, the FFT of the EMP signal registered by the multi-gap IC has been performed. Figure 5.20 shows the FFT of the signal shown in fiure 5.19. The frequency components shown in fiugre 5.20 ranging from about 10MHz up to about 1GHz.
In figure 5.21 is shown the signal acquired, placing the multi-gap IC at about 1m

from the target and at about 1m from the kapton window .

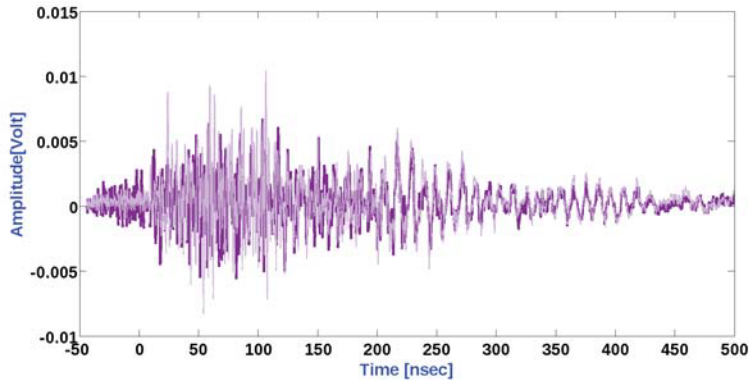

Figure 5.23: EMP signal acquired with multi-gap IC (IC_1 in purple and $IC2$ in light purple) placed at 0° with respect to the target normal about 3.5m from the target and at about 2.5m from the kapton window.

As one can see in fig.5.21, the signal is bipolar with a maximum amplitude of about 10mV (peak to peak) and time duration of about 500 ns. Comparing figure 5.21 with figure 5.19, the EMP is attenuated of an order of magnitude lower compared to the signal shown in figure 5.19.
In figure 5.22 is shown the FFT of EMP signal in Fig.5.21. The frequency components ranging from ten's of MHz up to about 500 MHz.

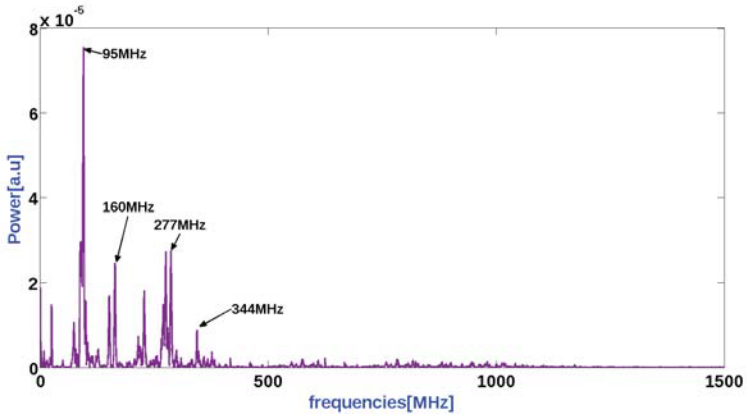

Figure 5.24: FFT of EMP signal in Fig. 5.23

Figure 5.23 shows the signal acquired when the multi-gap IC has been placed at about 1m from the target and about 2.5m from the kapton window.
The bipolar signal shown in figure 5.23 has a maximum amplitude of about 10mV (peak to peak) and time duration of about 500 ns.
The FFT (figure5.24 of the EMP signal in figure in figure 5.23, shows frequency components ranging from ten's of MHz up to about 300 MHz.
The characterization of the multi-gap IC response, at different distance, allowed to study the frequency components of the signal. Moreover, in order to further attenuate the EMP noise affecting the ion signal, low-pass filter with a cut-off of 100 MHz has been used.

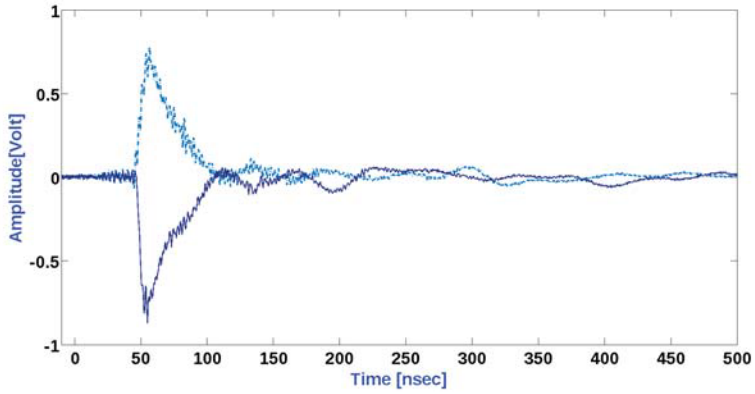

Figure 5.25: The typical ion signal acquired with multi-gap IC (IC_1 in light blue and $IC2$ in blue) placed at 0° with respect to the target normal about 1m from the target and at about 1cm from the kapton window.

The multi-gap IC has been placed at 0° with respect to the target normal direction at about 1m from the target and 1cm from kapton window.
In figure 5.25 is shown the ion signals acquired with multi-gap IC. The signal in figure 5.16, shows a broad structure due to protons.
In agreement with the EMP characterization results obtained with the FC and the SEM detectors, the EMP becomes almost negligible using a 100 MHz low-pass filter.

5.3 Time evolution signal measurements with FC and dose estimation

As discussed in section 5.2.1, using a 100 MHz low-pass filter, the EMP becomes almost negligible and an ion signal is acquired. In figure 5.26 is shown a scheme of the experimental setup of FC. The FC has been placed at 0° at about 90 cm from the target, (i.e. the detector entrance surface is at 90 cm from the target and the detector cup is at about 130 cm from the target). The ion signal has been

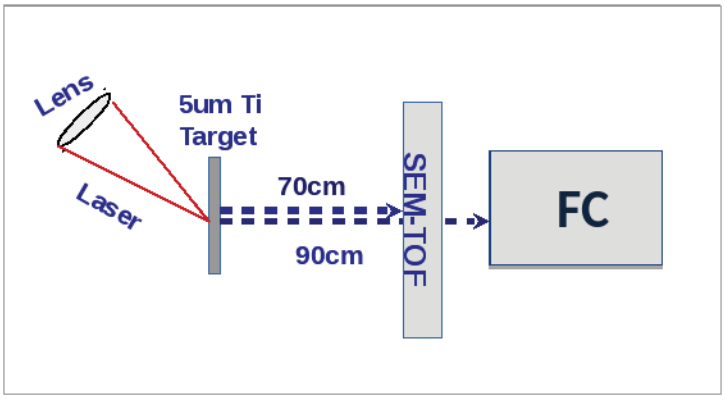

Figure 5.26: Scheme of the experimental setup of FC placed at 0° at 90 cm from the target

acquired using a 100 MHz low-pass filter connected to the FC output.
Figure 5.27 shows a typical time evolution signal measured with the FC, and three peaks can be identified: a negative peak corresponding to the fast electrons (0-35 ns), a narrow peak (50-100 ns) generated by the fastest proton group, and a broader structure (100-500 ns), arising from different ion species and charge state contribution, typically present as target contaminants, follows according to the time evolution of the ion signal together with the slow proton group.
The broad peak in the time of flight range between 100 ns and 400 ns is mainly due to the contribution of carbon ions, accelerated from the target as contaminants. Their charge states and maximum energies have been identified due to measurements performed using a Thomson Parabola spectrometer (Fig. 5.28) placed along

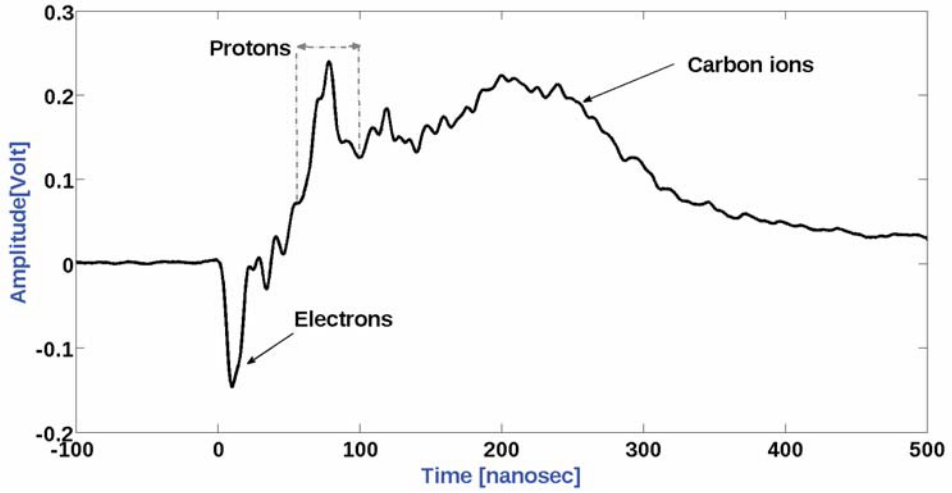

Figure 5.27: Typical time evolution signal measured with the FC

the target normal direction during the preparatory phase of the experimental campaign (Fig. 5.2). Taking into account the information on the ion species extracted from the TP analysis, the time interval due to the fast proton group has been uniquely identified. Once the time evolution intervals of protons (time intervals

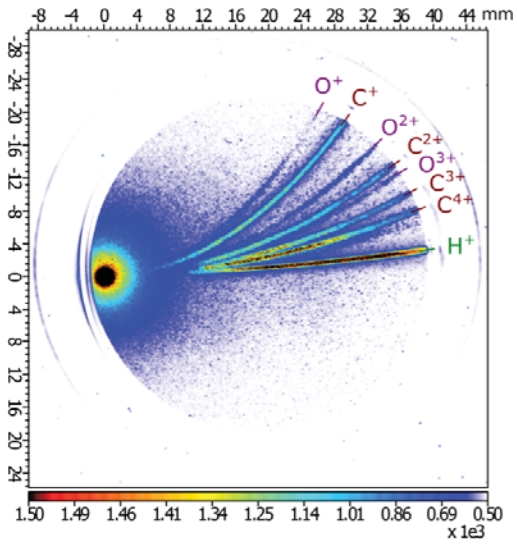

Figure 5.28: Imprint on the TPS of the ion beam accelerated in the forward direction.

between 50ns and 100 ns) has been identified, the signal shown in figure 5.27 has been directly converted in proton energy spectrum, (figure5.29), using the formula [104]:

$$\frac{dN}{dE} = \frac{V}{eR}\frac{t^3}{ml^2}. \tag{5.4}$$

where e is the value of the elementary charge and according to various types of particles arriving to the detector, m is the atomic mass unit, V is the measured voltage, R is the total resistivity of the detector circuits (including termination on the oscilloscope), t corresponds to the time evolution signal registrated and selected, l is the target-detector distance. In figure 5.29 is shown the energy

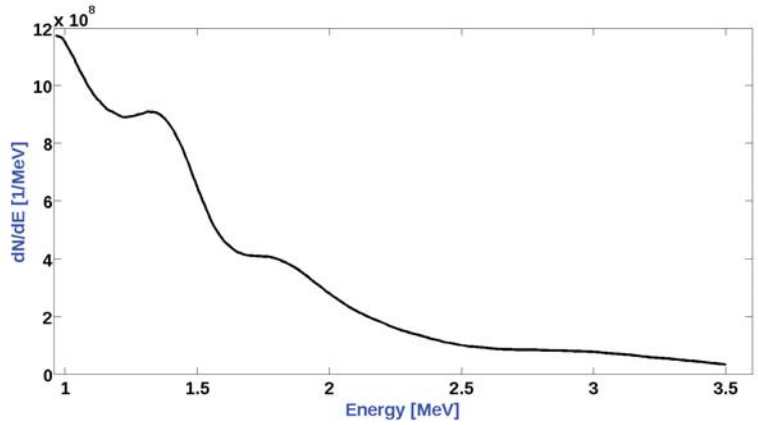

Figure 5.29: Proton energy spectrum reconstructed from the time evolution signal intervals 50ns<time evolution signal<100ns

spectrum reconstructed using the formula 5.4. As one can see, the maximum energy observed for protons is about of 3.5 MeV, in the time of flight range between $50ns$ and $100ns$. In addition, as shown in fig. 5.29, a decreasing exponential energy distribution, typical of the TNSA acceleration regime, can be clearly observed.
In order to normalize the energy spectrum to the solid angle of the beam and to solid angle of the detector, the formula 5.4 have be modified as, [104]:

$$\frac{dN}{dE} = \frac{V}{eR}\frac{t^3}{ml^2}\frac{\Omega_{BEAM}}{\Omega_{DETECTOR}}. \tag{5.5}$$

where Ω_{BEAM} is the solid angle of the beam and $\Omega_{DETECTOR}$ is the solid angle of the detector. Figure 5.30 shows the energy spectrum normalized to the solid angle

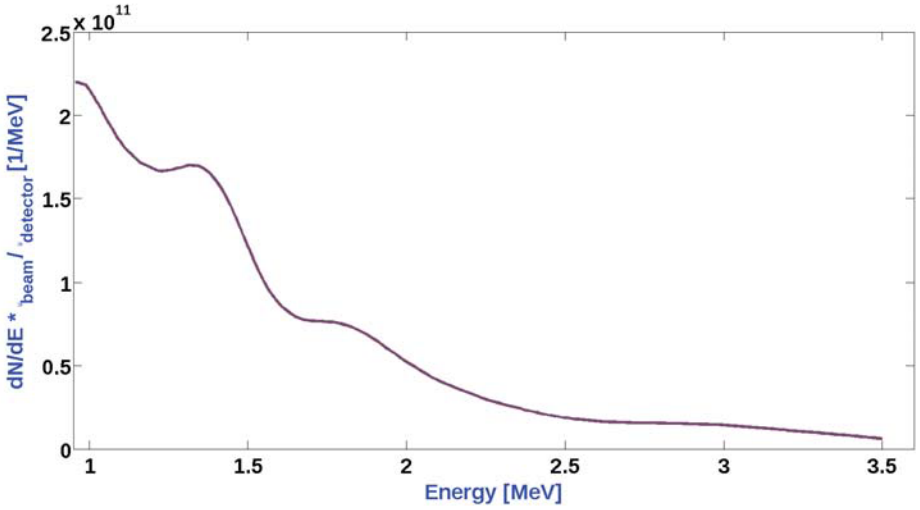

Figure 5.30: Proton energy spectrum reconstructed from the time evolution signal intervals 50ns<time evolution signal<100ns and normalized to solid angle of the beam and solid angle of the detector

of the beam and to solid angle of the detector.
In order to extract the charge collected by the FC and originated by the fast proton group in the time interval between 50 ns and 100 ns, the integral of the energy spectrum (in figure 5.29) has been calculated. A proton charge of 145 pC has been obtained, corresponding to a total number of protons 9.3*10^8.
Assuming an homogeneous spatial distribution of the beam over the area covered by the FC, (diameter cup is of 45 mm), the corresponding fluence is of 5.8*10^7 Protons/cm^2.
In order to estimate a value of dose in water, the formula of absolute dose in water has been approximated as:

$$D_w = \frac{1}{A_{eff}} \frac{\sum_{E_min}^{E_max} S(E)N(E)dE}{\sum_{E_min}^{E_max} N(E)dE} \frac{Q}{e} 1.6020 \times 10^{-10} \quad [Gy] \tag{5.6}$$

where as A_{eff} has been used the area covered by the FC (45 mm). The average stopping power has been determined, extrapolating all stopping power corresponding to the energy range between 750 keV and 3.5 MeV with an exponential fit of second order.
The absolute dose has been calculated directly from the energy spectrum, applying formula 5.6 and a value of about 2 Gy has been found.
In order to evaluate the overall uncertainty on the absolute dose measurement with the FC, the error propagation law, has been applied in formula 5.6, considering the statistical uncertainty on collected charge, on the stopping power and the on the beam effective area. The error on the absolute dose, of the order of about 10% has been estimated.
The analysis procedure on signal acquired with the FC, has been validated by comparing the energy spectrum reconstructed from time evolution signal signals extract with Diamond detectors(Fig. 5.31).
Comparing the energy spectrum in figure 5.29 acquired with the FC with the one shown in figure 5.31 acquired with diamond detectors, the energy range measured with the FC is lower than the one extracted from TOF signal of diamond detectors. The underestimation of energy with the FC could be explained considering that the FC, tipically, is not a detector used to provide particle energy spectrum but it is a detector tipically used to count the charge entering it.
In order to increase the ion signal, a charge amplifier, with a resistence of 5.6KΩ and capacitance of $180pF$, have been used, within the 100MHz LP filter.
Moreover, in front of the entrance window of the FC, a thin Al foil of $12\mu m$ has been placed, in order to stop the Carbon ions contribution. The signal acquired, using the charge amplifier and placing the FC at 0° at about 90 cm from the target, is shown in figure 5.32(blue line).
A charge amplifier, as know from literature, is a charge integrator which provides an output pulse whose amplitude is proportional to the amplitude of the voltage pulse supplied to its input terminals [12].
When the time constant of the input circuit (the parallel combination of the input

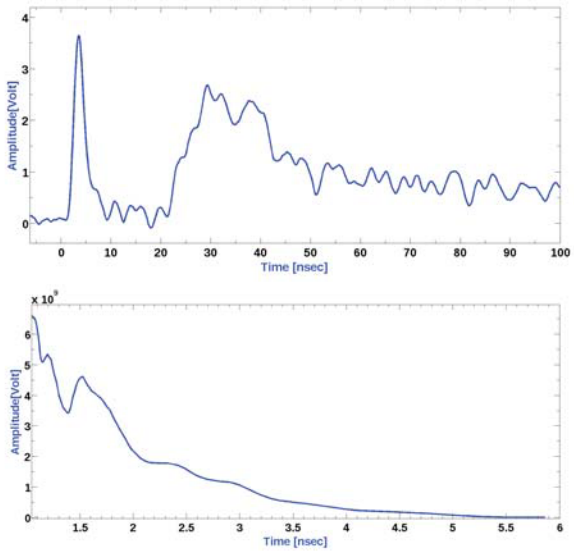

Figure 5.31: TOF signal and Proton energy spectrum reconstructed from the TOF intervals 50ns<TOF<100ns with Diamonds detectors

capacitance and resistance) is large compared with the charge collection time, the input pulse will have an amplitude equal to:

$$V_{max} = Q * C. \tag{5.7}$$

where C is the input capacitance. The capacitance is fixed, so the output pulse produced by a voltage-sensitive amplifier is proportional to the charge Q liberated by the incident radiation.

As shown in the figure 5.32, the initial part of the signal is lost because of the EMP, which is inserted into the amplifier, despite the use of a LP filter, causing a distortion of the signal. This effect causes an underestimation of the max value of the signal.

In order to extract the protons contribution and taking into consideration of the effect due to EMP, a fitting procedure using an exponential fit has been performed. The exponential fit starts from the part of the signal in which the distortion due to the EMP is no longer present, to establish the maximum voltage. The exponential fit is shown in figure 5.32, green line.

As one can see in figure 5.32, the maximum value acquired by the FC with the

amplifier and the 100MHz LP filter is at about 310ns, while the value estimated using the exponential fit is at about 120 ns. From the inverse of the formula 5.7,

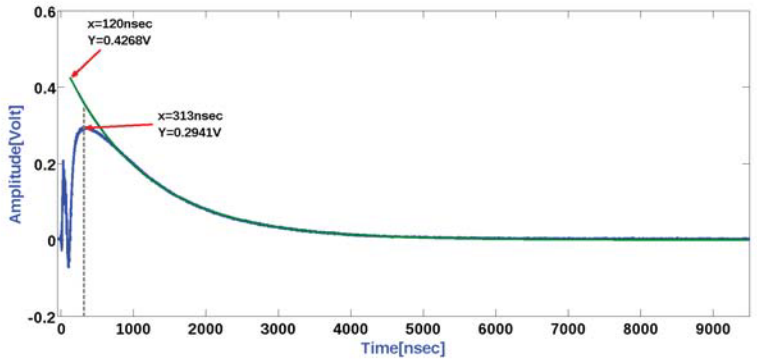

Figure 5.32: Time evolution signal signal acquired with a charge amplifier and an Al foil placed in front of the entrance window of the FC (blue) and exponential fit of the signal (green)

the total charge Q has been determined. A proton charge of 850nC is obtained considering the maximum value estimated using the exponential fit, corresponding to a proton number of 5.3*10^8 and a fluence of 3.3 *10^7 Protons/cm^2, assuming an homogeneous spatial distribution of the beam over the area covered by the FC (45 mm).

As it is well known, with the use of an amplifier the time information is lost, so it is not possible reconstruct the energy spectrum.

In order to extract the dose in water, it is possible to use the energy spectrum of the signal acquired with only the LP 100MHz filter, figure 5.29, because of a certain stability has been verified over time, both from measurements performed with FC and with diamonds detectors. The value of dose in water found is about of 1.5Gy, in accordance with the dose measured in configuration reported before (FC with only LP filter). Although the proton signal measured with the FC is around of hundreds of mV and the proton charge has been extracted from the time evolution signal, this preliminary dose estimation, in the two cases, confirms the possibility to use the FC to measure the dose delivered by a laser-driven proton beam even in harsh electromagnetic environment.

5.4 Characterization of the SEM detector in a laser-driven environment

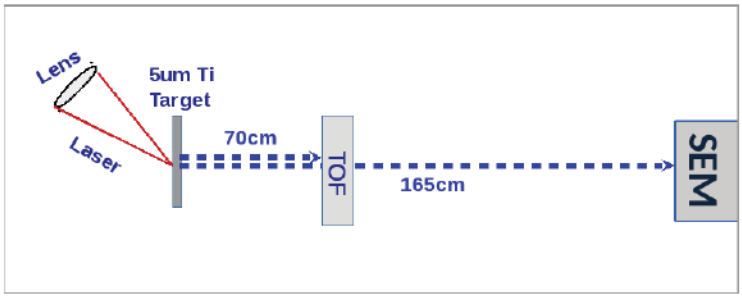

Figure 5.33: Scheme of SEM detector experimental set-up.

As described for the FC in section 5.3, after a study about the influence of EMP on the signal acquired with the SEM detector, the time evolution signal has been acquired, using a a 100 MHz LP filter connected to the SEM output. Figure 5.33 shows a scheme of the experimental setup used.

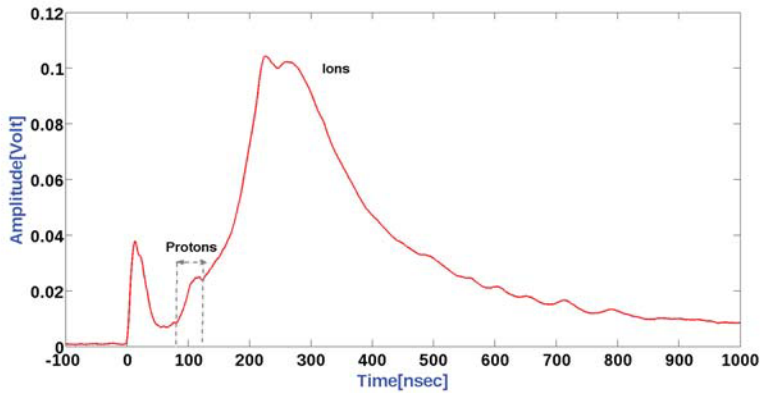

Figure 5.34: Typical ion signal registered by the SEM at 165 cm along the target normal direction.

It has been placed at 0° at 165 cm from the target along the target normal direction, inside a DN100 vacuum cross connected to the interaction chamber using a DN 40 pipe. As reported in section 5.2.2, the pipe has been used to increase the

distance between the SEM and the laser-target interaction point and to shield the detector itself from the EMP resonating inside the interaction chamber.
As one can see from figure 5.34, using the LP filter, a broad structure due to the slow ion contribution could be observed for time values greater than 200 ns. Taking into account the information on the ion species extracted from the TP analysis, the time interval due to the fast proton group has been discriminated for time values between 70 ns and 100 ns.
As one can see from the time evolution signal obtained optimizing the SEM detector setup, as for instance distance from the EMP origin and electrical insulation, and using proper low-pass filter, the detector can be used as a reliable on-line beam monitor. Moreover, calibrating the SEM signal amplitude against a reference detector, such as a diamond detector or a FC, it will be possible to reconstruct the shot-to-shot energy distribution from the in-transmission SEM signal, without perturbing the transportation.

5.5 Characterization of IC in a laser-driven environment

The multi-gap IC has been tested for the first time with low-energy laser-driven proton beams during the experimental campaing carried out at LOA laser facility. The used experimental setup is shown in figure 5.35.
The multi-gap IC has been placed in air in forward direction, at about 1m from the target, at 0° with respect to the target normal and 1 cm from kapton window mounted in a flange connected with the interaction chamber, as shown in figure 5.35.

In front of the entrance window of multi-gap IC Al foils of various thicknesses have been placed, in order to completely stop ion contribution and for protons, achieve different degraded energies, depending on Al thickness used.
In Figure 5.36 is shown the signal produced by ionization in the two different gaps and acquired with the multi-gap IC applying an HV of -800V at the first gap and

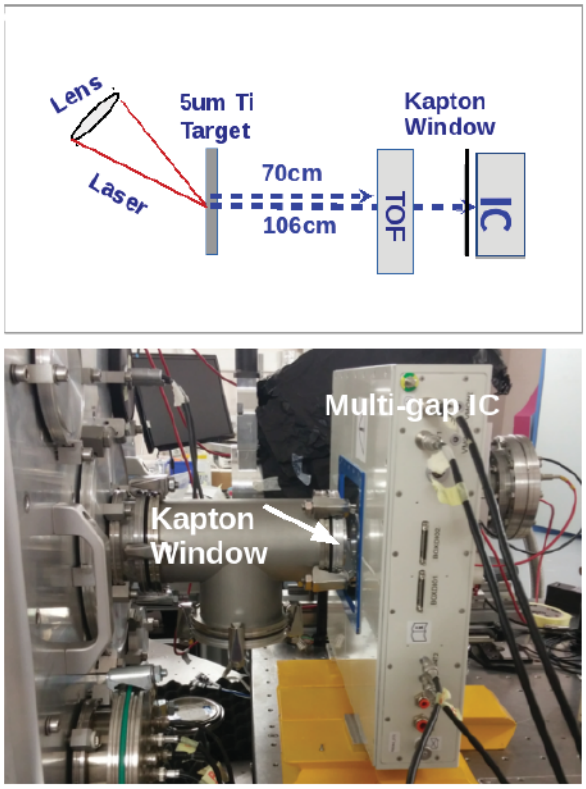

Figure 5.35: A schematic layout of the experimental setup for multi-gap IC characterization.

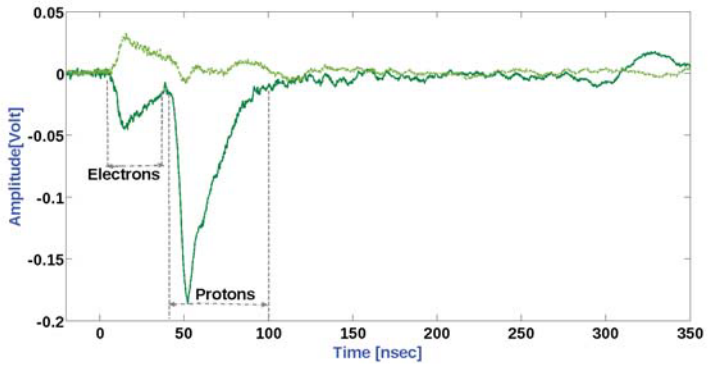

Figure 5.36: Signal acquired with multi-gap IC (IC_1 in green and $IC2$ in light green) applying an HV of -800V at the first gap and 400V at the second gap, placing a 24μm thickness of Al foil in front of the external window of multi-gap IC.

400V at the second gap, with an Al foil of 24μm thickness. As shown in figure, the time signals acquired in both gaps are characterized by two different bumps: in the interval between 2ns and 40 ns the signal is arising from the fast electron contribution while in the interval between 40 ns and 100 ns the bump is produced by protons. Using an Al foil of 24μm thickness, protons up to 1.4MeV are stopped.

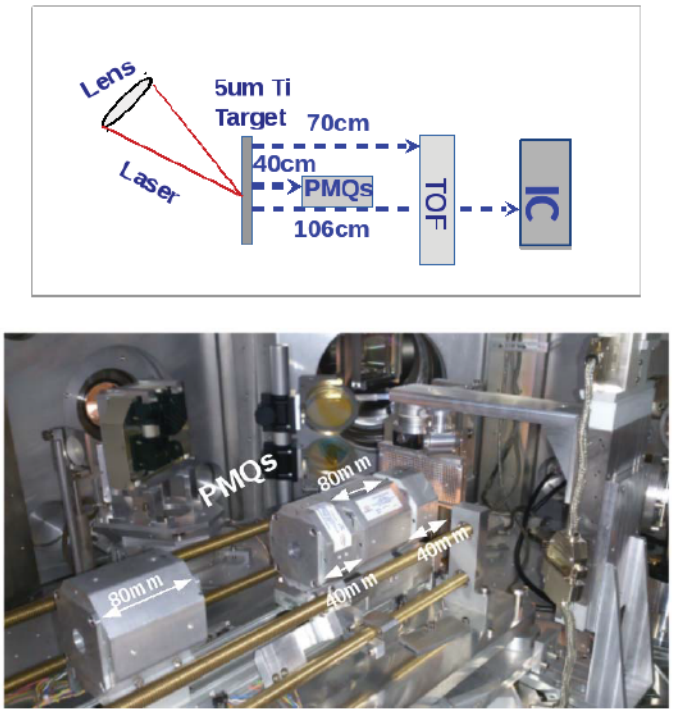

Figure 5.37: On the top the schematic layout of the experimental setup for multi-gap IC characterization in terms of response with a system of PMQs, on the bottom the PMQ system with mechanics set inside the SAPHIR interaction chamber.

In order to improve the transport of protons, a system of focusing PMQs has been used. As shown in figure 5.37, PMQs have been placed along the target normal direction, after about 40mm far from the target.

The PMQ system consists of 80 mm length PMQs and two 40 mm length PMQs with a net bore of 20 mm and a gradient of about 100 T/m (figure 5.37) [56]. PMQs are provided with carriages, guides and step motors remotely controlled,

in order to change the relative distances between magnets and tune the system for the handling of different energies from a few MeV up to 20 MeV, (figure 5.37 on bottom). During the experiment with the multi-gap IC, they have been set to focus 6 MeV protons component according to the calculation reported in [56].
Figure 5.38 shows the signals acquired with IC, placing an Al absorber of $24\mu m$ in front of the external window of multi-gap IC. As one can see in figure5.38, the signal acquired with the multi-gap IC, using a system of PMQs, is characterized by a single big peak (both gaps) arising from accelerated protons.
The contribution due to the fast electrons present in the signals acquired without the PMQs (figure 5.36), has been efficiently removed confirming the focusing effect of the PMQs.

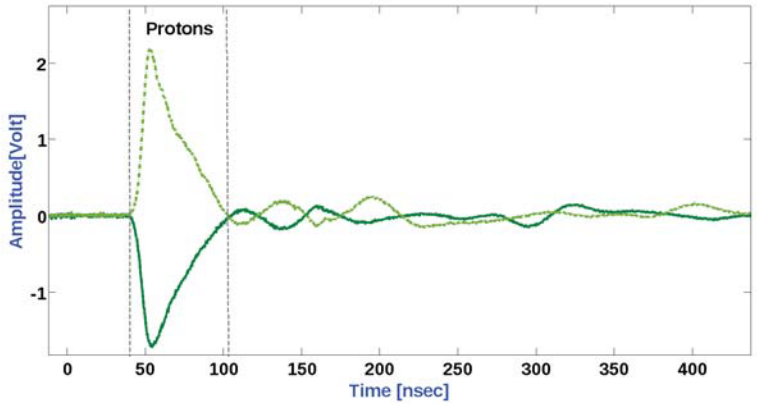

Figure 5.38: Signal acquired with multi- gap IC (IC_1 in green and $IC2$ in light green), applying an HV of -800V at the first gap and 400V at the second gap, when a system of PMQ is mounted in the experimetal set-up. An Al foil of $24\mu m$ thick has been placed in front of the external window of multi-gap IC.

Monte Carlo simulations, with SRIM software (The Stopping and Range of Ions in Matter), have been also performed in order to evaluate the minimum proton energy cutoffs, needed to traverse each layer composing the IC. Moreover, known the energy cut-off for each layer, it is possible to evaluate the maximum protons energy really available with experimental set-up of figure 5.37, comparing the results of SRIM simulation with the signal acquired with multi-gap IC.

The minimum energy cut-offs have been calculated for the materials reported in figure 5.39. It has been considered 25 μm exit kapton window of vacuum chamber, 1cm air i.e. the distance from the kapton window and the materials corresponding to each different layer composing the multi-gap IC.
The SRIM simulation have been performed for each Al foil, placed in front of the multi-gap IC.

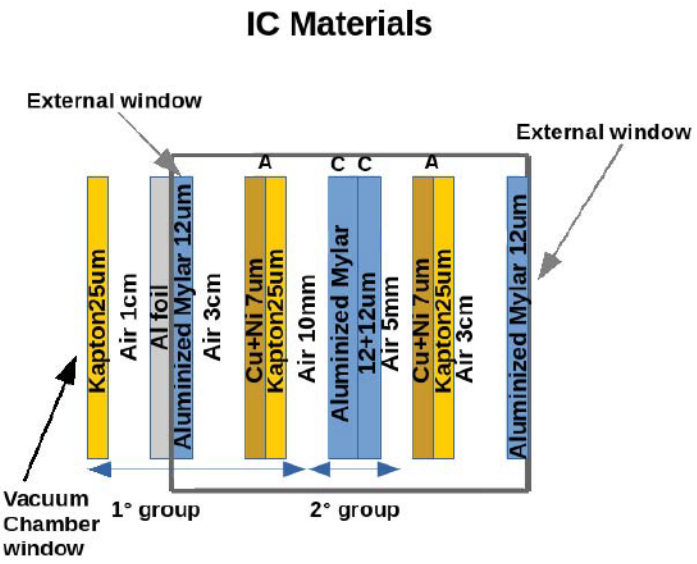

Figure 5.39: Scheme of the Matiarials, used for SRIM simulation: The two chambers are allocated in the center of a box of aluminium, filled of air. The external window is made up of 12 μm of aluminized mylar. The Anode is a thin layer of 5μm of copper and 2 μm of Nichel deposited on a 25 μm layer of kapton, while the cathode is constituted by a 12 μm layer of aluminized mylar. The two gaps of multi-gap IC are filled of air and are respectively of 10mm (IC_1) and 5 mm (IC_2).

As shown in the scheme in figure 5.39, two groups of materials can be identified for the simulations: the ones belonging to the first gap (10 mm thick) and the ones composing the second gap (5 mm thick). In table 5.1 some results of SRIM simulations are reported. As one can see in table5.1, when an Al absorber of 192 μm is placed in front of the IC, the minimum energy to have a signal on both gaps is of 6.5 MeV, while when is used Al absorber of 168 μm, the minimum energy

Table 5.1: Results of Srim simulation of lower energy cutoffs for protons for each component of IC with different thickness Al foil placed in front of the external window.

Al Foil thickness[μm]	**Group of Materials**	$E_{cut-off}$ **[MeV]**
192	Group 1	6.2
	Group 2	6.5
168	Group 1	6
	Group 2	6.3
96	Group 1	5
	Group 2	5.2
48	Group 1	4
	Group 2	4.4
12	Group 1	3.3
	Group 2	4

to have a signal on both gaps is of 6.3 MeV. In figure 5.40 are shown the signals acquired with multi-gap IC, placing in front of the entrance window respectively, an Al foil of 192μm and 168μm thickness. As one can see in figure 5.40, when an Al absorber of 192μm is placed in front of the external window of multi-gap IC, no proton signal is registred by multi-gap IC, so comparing the result with the SRIM simulation the maximum energy available is lower of 6.5 MeV. When an Al absorber of 168μm is placed in front of the external window of multi-gap IC, a signal is registred, in both gap. Therefore, the minimum energy evaluated with SRIM simulation is of about 6.3 MeV.

The result obtained with the multi-gap IC is confirmed by the energy spectrum reconstructed from the TOF signals (Fig. 5.41) acquired with the diamonds detector, placed at about 70cm from the target. Moreover, a preliminary study of the multi-gap IC response varying the applied voltage to both the two independent gaps has been carried out. Starting from a configuration with -800 V and +400 V respectively applied to IC_1 and IC_2, the voltage has been decreased down to -50 V

and +25 respectively for the two different gaps. As shown in figure 5.42, both the two signals related to the gaps are decreasing, due to the fact that, as expected, a lower applied voltage implies higher recombination effects, particularly for these high dose rates and, consequently, a lower charge collection at the electrodes.

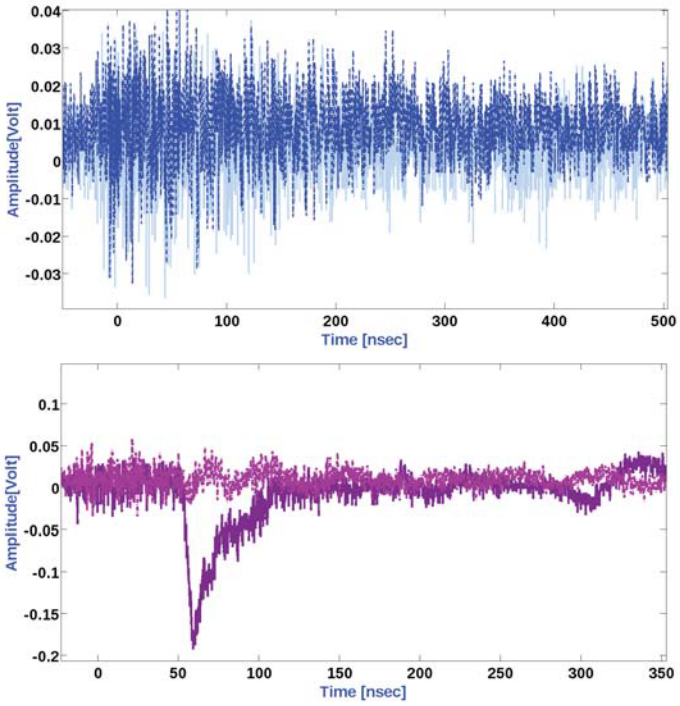

Figure 5.40: On the top: signal acquired with IC, placing a 192μm thick of Al foil in front of the external window(IC_1 in light blue and $IC2$ in blue), On the bottom: signal acquired with multi-gap IC, placing a 168μm thick of Al foil in front of the external windown of multi-gap IC (IC_1 in purple and $IC2$ in light purple).

This preliminary study provides an indication of how large is the effect of ion recombination for these extremely high dose rates per pulse. Of course the trend, in this case, is also influenced by the pulse-to-pulse reproducibility, therefore a higher statistics would be necessary to better study it. Further studies are planned to further characterize the multi-gap IC chamber on this concern.
The results obtained have confirmed the possibility of using the multi-gap IC in a laser driven environment.

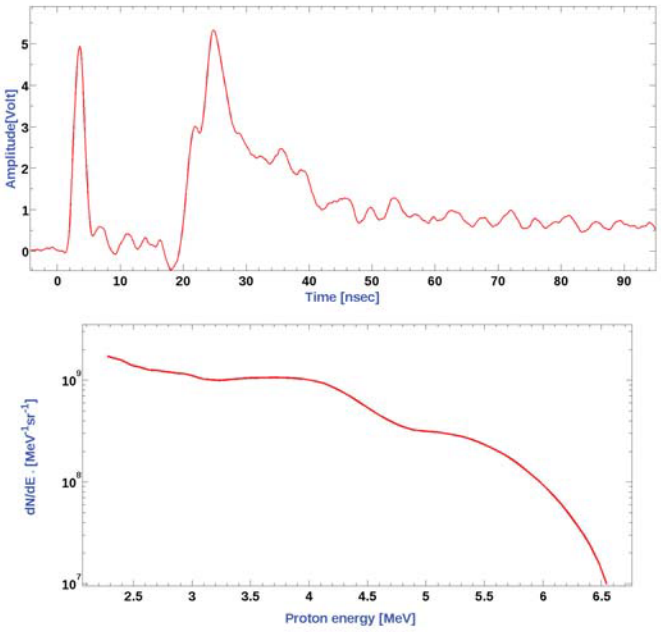

Figure 5.41: TOF signals and energy spectrum acquired with the diamonds detector.

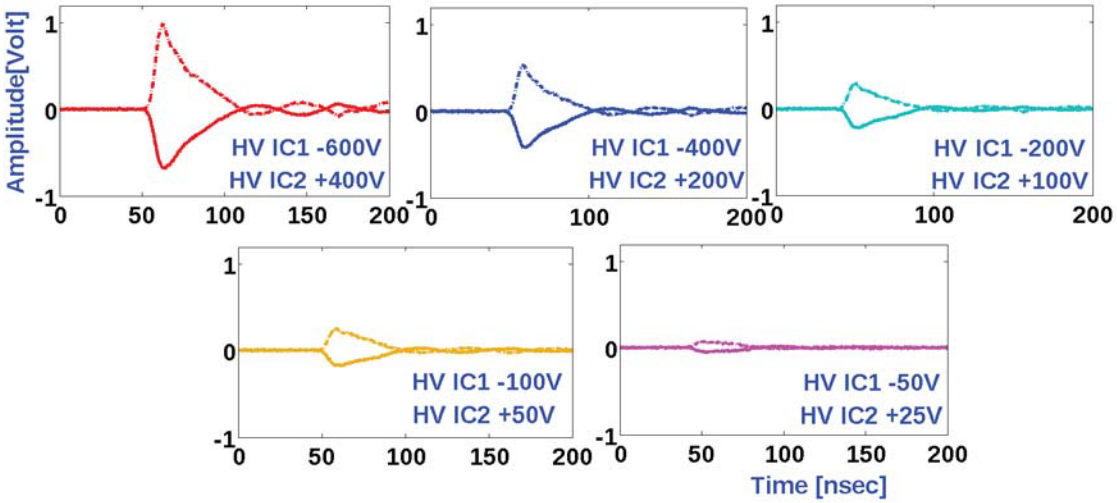

Figure 5.42: Signals acquired with multi-gap IC applying an HV of between -800 V and -50 V to IC_1 and between +400V and +25 V to IC_2.

Furthermore, calibrating the multi-gap IC with the FC absolute dosimeter, it will be possible to use the in-transmission multi-gap IC to on-line measure the delivered dose per pulse.

Conclusions

The work presented in this thesis has been carried out in the framework of the design and realization of the ELIMED (ELI- Beamlines MEDical and multidisciplinary applications) beam line. The ELIMED beam line represents the final section of the ELIMAIA (Multidisciplinary Applications of laser-Ion Acceleration) user-oriented beam line addressed to the transport, handling and dosimetry of the laser-driven ion beams. It will allow to transport stable, controlled and reproducible beams which will be available for all the users interested in multidisciplinary and medical applications of high energy laser-accelerated beams.

This work has been mainly focused on the realization and characterization of dosimetric detectors for the absolute and relative dosimetry of ELIMED beam line. The details of the ELIMED beam line have been discussed in chapter 2, in particular a description of the dosimetric detectors of the beam line has been reported in chapter 3.

The transported laser-accelerated ion beams at ELIMAIA beam line, will be characterized by very high intensities per pulse, i.e. up to 10^7-10^{10} particles per bunch, and very short temporal structure (ns), compared to 10^8-10^9 particles/s accelerated by conventional clinical machines. This results in an extremely high dose rates, i.e. 10^6-10^9 Gy/min (vs 10-50 Gy/min of conventional proton therapy), which implies the development of dose-rate independent systems for absolute and relative dosimetry for the ELIMED beamline.

The dosimetric system, as reported in chapter 3, is composed by dose-rate independent detectors which have been specifically designed and realized to work in a typical laser-driven environment, characterized also by a strong electromagnetic

pulse.
In particular, a Faraday Cup (FC) for absolute dosimetry has been designed and realized, in order to overcome ion recombination effects that may occur using conventional dosimeters, as ionization chambers, at high dose-rate per pulse. The FC, together with radiochromic films (RCF), allows to determine the absorbed dose to water. RCF are, indeed, used in order to measure the effective beam area and the energy spectrum (when used in stack configuration), which have to be coupled with the collected charge in order to finally retrieve the dose.
In order to measure in real-time the dose delivered per pulse, without affecting the beam transport downstream at the irradiation point, a multi-gap Ionization Chamber (IC), has been designed and realized. The presence of a second gap close to the first one allows correcting for ion recombination effects caused by the very high dose-rate per pulse.
Moreover, in order to monitor the particle flux in real-time, a Secondary Electron Monitor (SEM), will be used, as described in Chapter 3.
In chapter 4 the characterization of RCFs and FC with conventionally accelerated proton beams at 62 MeV, performed at the CATANA proton therapy facility at LNS has been reported.
RCFs have been used to estimate the 2D dose distributions, X/Y profiles and the fluence and the obtained results have been compared with reference measurements. In particular, it has been shown that they can be used to measure the transversal and longitudinal dose profiles with high spatial resolution (0.17 mm). Therefore, considering that they are not dependent on dose rate, RCFs represent a valuable tool for relative dosimetry of laser-driven beams and they will be used to characterize the beam shape and the spatial dose distributions at the irradiation point.
The FC has been characterized studying its response as a function of the voltage applied to the electrode, which aims to repel secondary electrons created in the entrance window and to collect the ones produced in the cup itself. A specific working region, in terms of voltage, has been experimentally retrieved (between -2500 and -400 V), where the charge collection is optimized. Moreover, dependence on dose and dose-rate has been investigated, for the possible beam intensities provided by

the cyclotron. Ones the FC has been characterized and a proper working region has been retrieved, it has been used to determine the absolute dose, comparing the results with reference detectors used in the clinical practice.
The absolute dose has been measured with an overall estimated uncertainty of 4.5%, with a maximum discrepancy respect to the reference detector of about 3%.
In chapter 5, the characterization of the dosimetric detectors of the ELIMED beam line, FC, SEM and multi-gap IC, in an experimental campaign carried out at Laboratoire d′Optique Appliquée (LOA, Paris, France), has been discussed.
The aim of the experiment has been the characterization of the detector response, in order to reduce the electromagnetic pulse (EMP) signal and to investigate the frequencies of the signal due to the oscillation modes of the EMP inside and outside the interaction chamber.
The setup and the readout system of each detector have been optimized, in order to increase the ratio between the proton signal and the EMP noise.
The results obtained have confirmed that using a proper low-pass filters of 100MHz, the EMP signal amplitude can be attenuated and a signal generated from the fast ions component, particularly protons, accelerated inthe laser matter interaction, can been discriminated, for each dosimetric detector. Moreover, a preliminary measure of the dose has been carried out analysing the time evolution signal of the FC for specific shots and integrating the correspondent energy spectrum.
The results discussed in this thesis demonstrate that the detectors designed and realized for the ELIMED beamline will allow to perform measurements for multidisciplinary applications with the level of accuracy required for these kind of irradiations. Once installed at ELIMAIA, they will contribute to provide the Users with controllable and properly calibrated proton beams to be used for demonstrating the potentialities of laser-driven beams for future medical applications. Moreover, the investigated approaches have shown that these devices can be properly used even in this extreme environment characterized by the intense EMP accompanying the production of plasma.

...Grazie alla mia famiglia che mi ha sostenuto e supportato,
aiutandomi a portare a termine questo percorso...

Bibliography

[1] Robert R. Wilson, Radiology 47-vol.5 487-491,(1946), doi:10.1148/47.5.487.

[2] F. Wagner, et al., Physics of Plasmas 22 (2015) 063110.

[3] T. Kluge, et al., New Journal of Physics 14 (2012) 023038.

[4] S.P. Hatchett, et al., Physics of Plasmas 7 (2000) 2076.

[5] J. Badziak, Opto-Electronics Review 15 (2007).

[6] T. Esirkepov, M. Borghesi, S.V. Bulanov, G. Mourou, and T.Tajima, (2004), Phys. Rev. Lett. 92, 175003.

[7] A. Macchi, S. Veghini, F. Pegoraro, Physical Review Letters (2009) 103, doi:103.085003.

[8] L. Yin, B.J. Albright, K.J. Bowers, D. Jung, J.C. Fernandez, B.M. Hegelich, Physical Review Letters (2011) 107, doi:107.045003.

[9] Dieter Schardt, Thilo Elsässer, Daniela Schulz-Ertner, Rev. Mod. Phys.82-vol.383, (2008).

[10] M. Hollmark, J. Uhrdin, D. Belkic, et al., Phys. Med. Biol., 49:3247–3265, (2004).

[11] B. Gottschalk, CRC Press20–57, (2012).

[12] Glenn F. Knoll, John Wiley Sons Inc,(1999), doi:0-471-07338-5.

[13] Radiation Oncology Physics: A Handbook for Teachers and StudentsE.B. Podgorsak Technical Editor, (2005).

[14] IAEA TRS-398.

[15] G. Jaffé, Phys. Rev.vol.30-n.968, (1998).

[16] Gerald J. Hine,Gordon L. Brownell, "Radiation Dosimetry", New York Academic Press (1967).

[17] D.E. Lea, Cambridge University press, (2008), doi:10.1017/S030500410001242.

[18] J.J. Thomson and E. Rutherford, Philos. Mag vol.42-n.258 392–407, (1896).

[19] J.J. Thomson, Philos. Mag vol.47-n.253, (1899).

[20] J.W. Boag., Radiation Dosimetry, vol. 2. Academic Press, (1966).

[21] M. Borghesi, et al., Fusion Sci. Technol. 49, 412, (2006).

[22] K. A. Flippo et al., Phys. Plasmas, 15:056709, (2008).

[23] A. Macchi, M. Borghesi, M. Passoni, Physics plasm-ph, (2013).

[24] "A Superintense Laser–Plasma Interaction Theory" Primer (2013).

[25] L. Bertagna M. Passoni and A. Zani, New J. Phys., 12:045012, (2010).

[26] http://www.qub.ac.uk/sites/LIBRA/Resources/.

[27] http://www.oncoray.de/?id=22.

[28] http://www.munich-photonics.de/.

[29] W.Leemans, W.Chou, M.Uesaka, ICF A Beam Dynamics Newsletters 56(2011)51.

[30] Ken W. D. Ledingham , Paul R. Bolton , et al., Applied Sciences vol.4 402-443,doi:10.3390/app4030402, (2014).

[31] Colin Danson et al.,High Power Laser Science and Engineering vol. 3 3-14, doi:10.1017/hpl.2014.52, (2015).

[32] Leemans, W., Chou, W., Uesaka, M., ICFA-Beam Dynamics Newsletter vol.56 51–60, (2011).

[33] Bin, J. et all, Appl. Phys. Lett vol.101,(2012).

[34] C.N. Danson et al., Nucl. Fusion 44 (2004) S239.

[35] L. Pommarel, Plasma Physics- Université Paris-Saclay, Master thesis, (2017).

[36] L. Pommarel, et all, APS-123-PRAB .

[37] Glinec, Y.et all, Med. Phys.vol.33 155–162, (2006).

[38] Mothersill, C. et all, Genet, (2012).

[39] https://www.bnl.gov/atf/.

[40] https://www.bnl.gov/atf/experiments/Pages/Ions.php].

[41] D. Kraft, et al., New Journal of Physics, 12, 085003 (2010), doi:1088/1367-2630/12/8/085003.

[42] J. Schreiber, P. R. Bolton, and K. Parodi, Rev. Sci. Instrum. 87, 071101 (2016).

[43] https://www.munich-photonics.de/publications/all-years/.

[44] A. Mittone, A. Bravin and P. Coan, Measurement Science and Technology (2017).

[45] https://www.cala-laser.de/en/research.html.

[46] D. Margarone, G.A.P. Cirrone, G. Cuttone and G. Korn, Preface: 2nd ELIMED Workshop and Panel, AIP Conf. Proc. 1546 (2013).

[47] G.A.P. Cirrone et al., Proc. SPIE 8779, Laser Acceleration of Electrons, Protons, and Ions II; and Medical Applications of Laser-Generated Beams of Particles II; and Harnessing Relativistic Plasma Waves vol.III, doi:10.1117/12.2026530, (2013).

[48] G.A.P. Cirrone, et al., Nuclear Instruments and Methods in Physics Research, doi:10.1016/j.nima.2015.02.019,(2016).

[49] F. Romano et al., Nucl. Instrum. Meth. A 829 (2016) 153.

[50] F. Schillaci, et al., JINST vol.10, doi:10.1088/1748-0221/10/05/T05001, (2015).

[51] F. Schillaci et al.,(2015) JINST 10 T12001, doi:10.1088/1748-0221/10/12/T12001

[52] F. Schillaci et al., (2016) JINST 11 P08022, doi:10.1088/1748-0221/11/08/P08022

[53] F. Schillaci et al., MT24, Seoul, Korea, (2015).

[54] K. Halbach, Nucl. Instrum. Methods vol.187 109–117, (1981).

[55] K. Halbach, Nuclear Instruments and Methods 169 (1980) 1.

[56] F. Schillaci et al. Journal of Instrumentation 10 (2015) T05001.

[57] P. Castro, DESY TECHNICAL NOTE2003-01 (2003.)

[58] J. Tanabe, World Scientific Publishing Co. Pte. Ltd., 2005. ISBN: 981-256-381-4.

[59] M. Reiser, WILEY-VCH Verlag GmbH Co. KGaA.

[60] V. Scuderi et al., Jinst, March (2017), doi:10.1088/1748-0221/12/03/C03086.

[61] G. Milluzzo et al., Jinst, February (2017), doi:10.1088/1748-0221/12/02/C02025.

[62] G. Milluzzo et al., Jinst, March (2017), doi:10.1088/1748-0221/12/03/C03044.

[63] G.A.P. Cirrone, et al., Applied Sciences 5, doi:10.3390/app50x000x,(2016).

[64] P. Mulser and D. Bauer. vol. 238. Springer Science Business Media, (2010).

[65] A Superintense Laser–Plasma Interaction Theory Primer.(2013).

[66] R.A. Snavely, et al., Physical Review Letters, 85(14):2945, (2000).

[67] Paul M. Bellan, Fundamentals of plasma physics (2008).

[68] S.C. Wilks et al., Phys. Plasmas 8, 542 (2001).

[69] Hatchett, S. P., et al., Phys. Plasmas 7, 2076, (2000).

[70] E. L. Clark et al. Phys. Rev. Lett., 84:670, (2000).

[71] Maksimchuk, A., et al., Phys. Rev. Lett. 84, 4108, (2000).

[72] Hegelich, M., et al., Phys. Rev. Lett. 89, 085002 (2002).

[73] M. Passoni, et.al., New J. Phys.vol.12, (2010).

[74] Borghesi, M.,et al. Fusion Sci. Technol, (2006)

[75] Fuchs, J., et al., Nat. Phys. 2, 48, (2006b).

[76] Zeil K., S. D. Kraft, et al., New J. Phys. 12, 045015, (2010).

[77] T. Burris-Mog et al. Physical Review special topics accelerators and beams 14:121301, (2011).

[78] G.A. Mourou, G. Korn, W. Sandner, J. L. Collier, The ELI Whitebook, THOSS Media GmbH, (2011)

[79] Jackson, J. D., Classical Electrodynamics (Wiley, New York),Chap. 7.3, 3rd ed., (1998).

[80] Y. Sentoku, et al., 2003, Phys. Plasmas 10, (2009).

[81] Palmer C.A.J., et al., Phys. Rev. Lett. (2012).

[82] Badziak, J., et al., Appl. Phys. Lett. 85, 3041, (2004).

[83] Henig, A., et al., Phys. Rev. Lett. 102, 095002, (2009a).

[84] R. L Forward, J. Spacecr. Rockets 21, 187 (1984).

[85] Simmons, J. F. L., and C. R. McInnes, Am. J. Phys. 61, 205, (1993).

[86] E. Grasell et al., Phys. Med. Biol. 40 1831, (1995).

[87] G. Cuttone et al., Phys. Med.vol.XV n.3, (1999).

[88] R. Cambria et al., Phys. Med. Biol.vol.42 1185–1196, (1997).

[89] J.D. Thomas et al., Nuclear instrument and Methods in PhysicsResearch A vol.536-n.11-21, (2005).

[90] comsol," A Simulation Toolkit",[http://www.comsol.it/].

[91] Geant4, " A Simulation Toolkit",[http://geant4.web.cern.ch/].

[92] R. Leanza, et al., Jinst February (2017), doi:10.1088/1748-0221/12/03/C03046.

[93] J W. Boag and T. Wilson, British Journal of Applied Physics vol.3-n.7-222, (1952).

[94] D. Kramer, B. Dehning, E.B. Holzer, G. Ferioli,M .Stockner

[95] D. Kramer "Design and implementation of a Detector for High Flux Mixed Radiation Fields", Thesis.

[96] G. Cuttone. et al., European Physical Journal Plus,(2011), doi:10.1140/epjp/i2011-11065-1.

[97] G.A.P. Cirrone et al.,IEEE TRANSACTIONS ON NUCLEAR SCIENCE, (2004).

[98] http://www.gafchromic.com/documents/EBT3Specifications:pdf.

[99] F. Fiorini et al., Phys. Med. 454-61 (2014).

[100] S. H. Park et al.,Journal of the Korean Physical Society, Vol. 49, No. 1, July (2006).

[101] J. Prokupek at al., REVIEW OF SCIENTIFIC INSTRUMENTS 85, 013302, (2014).

[102] T. Dzelzainis et al.,Laser Part. Beams 28 451, (2010) .

[103] W. Press, et al., Numerical recip in C++.

[104] J. Prokupek, Master's thesis (2012).